DIEGO NEI VENTURI

FROM DILUTE TO DENSE GAS-SOLID FLOWS SIMULATION: THE CFB RISER CASE STUDY

FEDERAL UNIVERSITY OF UBERLÂNDIA

SCHOOL OF MECHANICAL ENGINEERING

2020

DIEGO NEI VENTURI

FROM DILUTE TO DENSE GAS-SOLID FLOWS SIMULATION: THE CFB RISER CASE STUDY

Thesis submitted to the Graduate Program in Mechanical Engineering at the Federal University of Uberlândia, in partial fulfillment of the requirements to obtain the degree of **Doctor in Mechanical Engineering**.

Concentration area: Heat Transfer and Fluid Mechanics

Supervisor: Prof. Dr. Francisco José de Souza

Uberlândia, MG – Brazil
February 21, 2020

Ficha Catalográfica Online do Sistema de Bibliotecas da UFU
com dados informados pelo(a) próprio(a) autor(a).

V469
2020

Venturi, Diego Nei, 1990-
From dilute to dense gas-solid flows simulation [recurso eletrônico] : the CFB riser case study / Diego Nei Venturi. - 2020.

Orientador: Francisco José de Souza.
Tese (Doutorado) - Universidade Federal de Uberlândia, Pós-graduação em Engenharia Mecânica.
Modo de acesso: Internet.
Disponível em: http://doi.org/10.14393/ufu.te.2020.112
Inclui bibliografia.
Inclui ilustrações.

1. Engenharia mecânica. I. Souza, Francisco José de,1973-, (Orient.). II. Universidade Federal de Uberlândia. Pós-graduação em Engenharia Mecânica. III. Título.

CDU: 621

Bibliotecários responsáveis pela estrutura de acordo com o AACR2:
Gizele Cristine Nunes do Couto - CRB6/2091
Nelson Marcos Ferreira - CRB6/3074

UNIVERSIDADE FEDERAL DE UBERLÂNDIA
Coordenação do Programa de Pós-Graduação em Engenharia Mecânica
Av. João Naves de Ávila, nº 2121, Bloco 1M, Sala 212 - Bairro Santa Mônica, Uberlândia-MG, CEP 38400-902
Telefone: (34) 3239-4282 - www.posgrad.mecanica.ufu.br - secposmec@mecanica.ufu.br

ATA DE DEFESA - PÓS-GRADUAÇÃO

Programa de Pós-Graduação em:	Engenharia Mecânica				
Defesa de:	Tese de Doutorado, nº 293, COPEM				
Data:	vinte e um de fevereiro de dois mil e vinte	Hora de início:	08:00	Hora de encerramento:	12:00
Matrícula do Discente:	11613EMC005				
Nome do Discente:	Diego Nei Venturi				
Título do Trabalho:	From dilute to dense gas-solid flows simulation: the CFB riser case study				
Área de concentração:	Transferência de Calor e Mecânica dos Fluidos				
Linha de pesquisa:	Dinâmica dos Fluidos e Transferência de Calor				
Projeto de Pesquisa de vinculação:					

Reuniu-se no Auditório do MFlab - Bloco 5P, Campus Santa Mônica, da Universidade Federal de Uberlândia, a Banca Examinadora, designada pelo Colegiado do Programa de Pós-graduação em Engenharia Mecânica, assim composta: Professores Doutores: Dirceu Noriler - UNICAMP; Rigoberto Eleazar Melgarejo Morales - UTFPR; Carlos Henrique Ataíde - FEQUI/UFU; João Marcelo Vedovoto - FEMEC/UFU e Francisco José de Souza - FEMEC/UFU, orientador(a) do(a) candidato(a).

Iniciando os trabalhos o(a) presidente da mesa, Dr(a). Francisco José de Souza, apresentou a Comissão Examinadora e o candidato(a), agradeceu a presença do público, e concedeu ao Discente a palavra para a exposição do seu trabalho. A duração da apresentação do Discente e o tempo de arguição e resposta foram conforme as normas do Programa.

A seguir o senhor(a) presidente concedeu a palavra, pela ordem sucessivamente, aos(às) examinadores(as), que passaram a arguir o(a) candidato(a). Ultimada a arguição, que se desenvolveu dentro dos termos regimentais, a Banca, em sessão secreta, atribuiu o resultado final, considerando o(a) candidato(a):

Aprovado.

Esta defesa faz parte dos requisitos necessários à obtenção do título de Doutor.

O competente diploma será expedido após cumprimento dos demais requisitos, conforme as normas do Programa, a legislação pertinente e a regulamentação interna da UFU.

Nada mais havendo a tratar foram encerrados os trabalhos. Foi lavrada a presente ata que após lida e achada conforme foi assinada pela Banca Examinadora.

Documento assinado eletronicamente por **Francisco José de Souza**, **Professor(a) do Magistério**

Superior, em 21/02/2020, às 16:41, conforme horário oficial de Brasília, com fundamento no art. 6º, § 1º, do Decreto nº 8.539, de 8 de outubro de 2015.

Documento assinado eletronicamente por **RIGOBERTO ELEAZAR MELGAREJO MORALES**, **Usuário Externo**, em 21/02/2020, às 16:44, conforme horário oficial de Brasília, com fundamento no art. 6º, § 1º, do Decreto nº 8.539, de 8 de outubro de 2015.

Documento assinado eletronicamente por **João Marcelo Vedovoto**, **Professor(a) do Magistério Superior**, em 21/02/2020, às 16:45, conforme horário oficial de Brasília, com fundamento no art. 6º, § 1º, do Decreto nº 8.539, de 8 de outubro de 2015.

Documento assinado eletronicamente por **Carlos Henrique Ataide**, **Professor(a) do Magistério Superior**, em 21/02/2020, às 16:46, conforme horário oficial de Brasília, com fundamento no art. 6º, § 1º, do Decreto nº 8.539, de 8 de outubro de 2015.

Documento assinado eletronicamente por **Dirceu Noriler**, **Usuário Externo**, em 21/02/2020, às 16:47, conforme horário oficial de Brasília, com fundamento no art. 6º, § 1º, do Decreto nº 8.539, de 8 de outubro de 2015.

A autenticidade deste documento pode ser conferida no site https://www.sei.ufu.br/sei/controlador_externo.php?acao=documento_conferir&id_orgao_acesso_externo=0, informando o código verificador **1889572** e o código CRC **7CF76BB7**.

For my tireless and ever loving wife, Angela.

Acknowledgements

I must start this acknowledgements page by first thanking all the loving support from my family. Giving up on many family gatherings and personal proximity during four years to pursue this graduation, did not come easy for both sides. I thank specially my wife, who gave up on many things just to accompany me. They were all paramount in keeping me on the track. Love you all.

On the other end, here in Uberlândia, are all the friends made at the MFLab. Some of them helped me by sitting with me and discussing ideas and equations, other by teaching me how to use a software, and others just by getting my mind off the study and taking a cup of coffee or a glass of beer with me. It is fulfilling to be able to make such good friends away from home. Also here, I found two teachers who increased my desire for knowledge and taught me to be a better student and researcher, Profs. Francisco and Aristeu.

Other friends from afar were also present during this time. Those with whom I have forged such a strong bond in Blumenau at the LFC, but are now in the most different places. They surely helped me multiples times by taking the time to have very fruitful discussions over the web, or by having this and other discussions in person in the rare encounters.

I am also grateful to all fellow researchers around the world who corresponded to me when I asked for directions: to Prof. Jesse Capecelatro who helped me into better understanding the volume-averaged model and discussed some numerical implementations with me by e-mail, without even knowing me; to Prof. Berend van Wachem, Martin Sommerfeld, and Paulo Laranjeira da Cunha Laje for the help offered at the 2019 ERCOFTAC Guidance Seminar held just before the ICMF Rio, where we discussed ideas for the improvement of some numerical issues about the volume-averaged formulation; and to Prof. Karl D. Hammond for sending me the LAMMPS[1] Fortran wrapper code for DEM modeling, even though we ended up discontinuing this idea.

Moreover, I feel that at least some form of acknowledgement should also be directed to those who are silent helpers. Those who end up helping us with a blog post directed to graduate students or those who take their free and unpaid time just to create better tools for everyone. I thank these people by naming two who were very present in my days, Prof. Marco Mello from the *Sobrevivendo na Ciência* blog[2] ("Surviving in Science", in free translation) and Lauro César Araujo from the abnTeX2 project[3].

---

[1] <https://lammps.sandia.gov/>

[2] <https://marcoarmello.wordpress.com/>

[3] <https://www.abntex.net.br/>

On the financial side, I cannot forget to mention the support from the Brazilian National Council for Scientific and Technological Development (CNPq) for the full scholarship during this four years of research, and also to *Coordenação de Aperfeiçoamento de Pessoal de Nível Superior* (CAPES) and Petrobras. A researcher can only dream that his work may affect society in some way that more people start to see research budget as investment. And at last, I surely also have a lot to thank to all the staff at the Federal University of Uberlândia, at the Mechanical Engineering Graduate Program, and at the MFLab.

"Bear in mind that the wonderful things you learn in your schools are the work of many generations, produced by enthusiastic effort and infinite labor in every country of the world. All this is put into your hands as your inheritance in order that you may receive it, honor it, add to it, and one day faithfully hand it on to your children. Thus do we mortals achieve immortality in the permanent things which we create in common."
(Albert Einstein, The World As I See It)

"Inventions are, above all, the result of stubborn work,
in which there must be no room for discouragement."
(Alberto Santos Dummont)

Abstract

The importance of gas-solid flows in industry is never overestimated, they are present in many different production sectors and equipment. When in the vertical ascending configuration, such flows may appear in many different patterns, but the subjects of study in the present work will lie mainly on the fast fluidization or pneumatic conveying ones. In the present thesis, the main subject of investigation is on the modeling and simulation of gas-solid flows in CFB risers utilizing CFD. This equipment is commonly utilized for the recovery of heavy petroleum fractions into more usable products such as gasoline and diesel, and has a lot of interest from the oil companies. For this analysis, the UNSCYFL3D code is utilized, which is an already established computational code for the simulation of dilute gas-solid flows. The objective of this thesis is to consolidate a new formulation in the UNSCYFL3D that is suitable also for dense flows, but keeping a reasonably cheap computational cost. To do this, first it was noted from the literature that the gas phase formulation has to be changed into accounting the volume fraction, rather than using the standard single-phase equations. Another important aspect are the particle-particle collisions. It is common that in such cases deterministic collision approaches are used, but the increase in the computational cost may prohibit analysis in large equipment. For this reason, in the present thesis a stochastic model that has not been tested before for dense flows is utilized. Two formulations are summarized and presented in the thesis, one for dilute flows and one for dense flows. Both of them are within the Euler-Lagrange framework, with the point-particle approach. A thorough study is carried out beforehand for dilute flows to assess some late implementations, and to evaluate up to which point the dilute formulation is valid for dense flows. Following that, CFB riser simulations are carried out utilizing both formulations to show the importance of the correct modeling, and the accuracy of the stochastic particle-particle collision model in this condition. In the present thesis, we have shown that the dilute formulation is valid for a solids mass loading of up to $1\,\mathrm{kg_{part.}/kg_{air}}$ in horizontal flows, but up to $8\,\mathrm{kg_{part.}/kg_{air}}$ in well-distributed vertical ascending flows. However, as in CFB risers the configuration of the geometry encourages the agglomeration of the solids into clusters, even lower solids mass loadings ($4\,\mathrm{kg_{part.}/kg_{air}}$) are shown to need the dense formulation. Also, a comparison with experiments and other simulations utilizing deterministic collision approaches, show that the the present formulation is able to correctly predict the dense gas-solid flows in CFD risers up to $22\,\mathrm{kg_{part.}/kg_{air}}$.

Keywords: CFB riser, CFD, gas-solid flow, UNSCYFL3D.

Resumo

A importância dos escoamentos gás-sólido na indústria nunca é superestimada, eles estão presentes em muitos setores produtivos e equipamentos diversos. Na configuração vertical ascendente, estes escoamentos aparecem em diversos regimes, mas os de interesse da presente tese se classificam principalmente como fluidização rápida e transporte pneumático. Na presente tese, o principal objeto de investigação é a modelagem e simulação de *risers* de Leito Fluidizado Circulante (LFC) utilizando CFD. Este equipamento é comumente utilizado para a recuperação de frações pesadas do petróleo em produtos mais usáveis como a gasolina e o diesel, o que desperta muito interesse por parte das companhias de petróleo. Para esta análise, o código UNSCYFL3D é utilizado, o qual é um código computacional já bem estabelecido para simulações de escoamentos gás-solido diluídos. O objetivo desta tese, é consolidar uma nova formulação no UNSCYFL3D que seja também adequada para escoamentos densos, mas enquanto mantendo um custo computacional razoavelmente baixo. Para isto, nota-se da literatura que a formulação matemática da fase gasosa necessita de modificações para levar em conta a fração volumétrica, em vez de utilizar as equações padrões para escoamento monofásico. Outro aspecto importante são as colisões partícula-partícula. É comum que nestes casos abordagens de colisão determinística sejam utilizados, mas o aumento no custo computacional pode tornar esta análise proibitiva para equipamentos maiores. Por esta razão, na presente tese um modelo estocástico que ainda não foi testado em escoamentos densos será utilizado. Duas formulações são sumarizadas e apresentadas na tese, uma para escoamentos diluídos e outra para densos. Ambos estão dentro da estrutura da abordagem Euler-Lagrange, com a consideração de partícula pontual. Um estudo completo em escoamentos diluídos é apresentado antecipadamente para que se avalie algumas implementações recentes, e para se estimar até que ponto a formulação de escoamentos diluídos é válida também para os densos. Seguindo isto, simulações em risers de LFC são conduzidas utilizando-se ambas as formulações para que se mostre a importância da modelagem correta, e a acurácia do modelo de colisão partícula-partícula estocástico nesta condição. Na presente tese, mostrou-se que a formulação para escoamentos gás-sólido diluídos é válida para uma carga mássica de sólidos de até $1\,\mathrm{kg_{part.}/kg_{air}}$ em escoamentos horizontais, mas até $8\,\mathrm{kg_{part.}/kg_{air}}$ em escoamentos ascendentes verticais bem distribuídos. No entanto, como risers de LFC apresentam uma configuração geométrica que promove a aglomeração dos sólidos em *clusters*, mesmo em cargas mássicas mais baixas ($4\,\mathrm{kg_{part.}/kg_{air}}$) a formulação para escoamentos densos é necessária. Também, uma comparação com dados experimentais e de outras simulações que utilizaram abordagens de colisão determinística, mostrou que a formulação apresentada aqui é capaz de prever corretamente o escoamento gás-sólido denso em risers de LFC até $22\,\mathrm{kg_{part.}/kg_{air}}$.

Palavras-chave: riser de LFC, CFD, escoamento gás-sólido, UNSCYFL3D.

List of Figures

List of abbreviations and acronyms

AMG	Algebraic Multi-Grid
BiCG	Bi-Conjugate Gradient
CDS	Central Differencing Scheme
CFB	Circulating Fluidized Bed
CFD	Computational Fluid Dynamics
DC	Deferred Correction
DDPM	Dense Discrete Phase Model
DEM	Discrete Element Model
DNS	Direct Numerical Simulation
EE	Euler-Euler
EL	Euler-Lagrange
FCC	Fluid Catalytic Cracking
FVM	Finite Volume Method
KTGF	Kinetic Theory of Granular Flows
LES	Large Eddy Simulation
MP-PIC	MultiPhase Particle-In-Cell (also MPPIC)
ODE	Ordinary Differential Equation
PCM	Particle Centroid Method
PDE	Partial Differential Equation
RANS	Reynolds-Averaged Navier-Stokes (equations)
RMS	Root Mean Square
RSM	Reynolds Stress Model
SIMPLE	Semi-IMplicit Pressure Linked Equations

SOR	Successive Over-Relaxation
SOU	Second Order Upwind
SOUE	Second Order Upwind Euler
TFM	Two Fluid Model
U	Upwind
URANS	Unsteady Reynolds-Averaged Navier-Stokes (equations)

List of symbols

LATIN LETTERS

A	Area
$\mathbf{a}$	Generic fluid property of any tensorial order; Coefficient matrix of a linear system
A_μ, A_ε	Length scales in the two-layer k-ε model
C	Coefficient for a force modeling; Constant
C_μ	Constant in the k-ε model
C_l	Constant in the two-layer k-ε model
d_p	Particle diameter
$\mathbf{F}$	Force; Source term
f	Tangential friction factor; Generic variable
f_{coll}	Frequency of collision
$\mathbf{F}_{\mathrm{gp}}$	Gas-particle interaction term
$\mathbf{F}_{\mathrm{KTGF}}$	Collision force derived from the KTGF (in the DDPM model)
$\mathbf{F}_{\mathrm{MP\text{-}PIC}}$	Collision force in the MP-PIC model
$\mathbf{G}$	Relative velocity (relative to two different particles)
$\mathbf{g}$	Gravity vector
g	Statistical kernel; Filtering kernel
$\mathbf{G_{ct}}$	Tangential component of $\mathbf{G}$
$\mathbf{I}$	Identity matrix
I_p	Particle moment of inertia
$\mathbf{J}$	Impulsive force
k	Spring constant; Turbulence kinetic energy
l_μ, l_ε	Length scales in the two-layer k-ε model

$\dot{m}$	Mass flux
m_p	Particle mass
$\mathbf{n}$	Normal vector (depends on the context)
N_p	Total number of particles
P	Modified pressure
p	Pressure
P_{coll}	Probability of collision
P_k	Production term of k
P_s	Constant in the MP-PIC model
$\mathbf{R}$	Correlation function
$\mathbf{r}$	Distance
Re_p	Particle Reynolds number
Re_S	Shear Reynolds number
Re_y	Turbulence Reynolds number
S	Source term; Cell face area
St	Stokes number
$\mathbf{T}$	Torque
$\mathbf{t}$	Tangential vector (depends on the context)
t	Time
T_E	Eulerian integral time scale
T_L	Lagrangian integral time scale
$\mathbf{U}$	Filtered (or mean) velocity vector
$\mathbf{u}$	Instantaneous velocity vector
$\mathbf{u}'$	Fluctuation (or RSM) velocity vector
V	Volume
$\mathbf{x}$	Position vector

y^+	Normalized distance from the wall

GREEK LETTERS

α	Volume fraction
β	Constant in the MP-PIC model
Γ	Diffusion coefficient
Δ	Difference
ϵ	Small number (to avoid numerical issues with division by zero)
ε	Dissipation rate of k
η	Damping coefficient; Particle mass loading in $\mathrm{kg_{part.}/kg_{air}}$
θ	Angle
θ_p	Granular temperature
κ	Dilatational viscosity; von Kármán constant
λ	Bulk viscosity
μ	Viscosity; Dynamic or molecular viscosity (when no subscript)
μ_α	Volume fraction dependent viscosity
μ_{eff}	Effective viscosity
μ_t	Turbulent (or eddy) viscosity
ξ	Normally distributed random number; Uniformly distributed random number
ρ	Density
$\boldsymbol{\sigma}$	Shear stress tensor
σ_ε	Constant in the k-ε model
σ_g	Gas mean fluctuation velocity
σ_k	Constant in the k-ε model
$\boldsymbol{\tau}$	Stress tensor (normal + shear)

τ_p	Particle relaxation time
ϕ	Angle; Generic variable
ψ	Angle
$\boldsymbol{\Omega}_g$	Relative particle-fluid rotation
$\boldsymbol{\omega}_g$	Fluid vorticity
$\boldsymbol{\omega}_p$	Particle angular velocity

SUBSCRIPTS

$2l$	Relates to the two-layer k-ε model
B	Relates to the Buoyancy force
C	Relates to the cell C
cp	Relates to the close packing of particles
D	Relates to the Drag force
F	Relates to the cell F, neighbor of C
f	Relates to the fluid phase; Relates to the face of a cell
fict.	Relates to the fictitious particle
g	Relates to the gas phase (fluid phase)
LR	Relates to the Rotation-induced Lift force
LS	Relates to the Shear-induced Lift force
n	Relates to the normal direction
p	Relates to the particle phase (solid phase)
rel	Relates to *relative*, to two particles or between the gas and the particle
s	Relates to the solid phase (particle phase)
t	Relates to the tangential direction
W	Relates to the Weight force

SUPERSCRIPTS

0	Relates to before the collision (pre-collisional)
old	Relates to the previous time-step

Contents

Chapter 1

Introduction

Throughout all of its existence, mankind has copied nature. We have seen it many times. Look at da Vinci's flying machine using bat-like wings, or de Mestral's invention of the Velcro® hook and loop for some classical examples. There are also countless examples of particle-laden flows in the environment that an engineer can seek inspiration to. Look at snow powder avalanches that change the shape of a landscape, the pyroclastic flow from a volcano that changes the ecosystem around it, or the Sahara dust plume that influences the climate in a large portion of the planet. Even Computational Fluid Dynamics (CFD), one of the most advanced engineering tools, is not astray from nature. The simulation of fluid flows, or particle dynamics, is the simulation of nature itself.

All the time, when the engineer does not know what to do or think, he turns to nature and look for ideas. We have looked at the birds to design our planes, at the fish to design our boats, at the living beings bone articulations to design our robots. This is the engineering design process, which is only an extension to the scientific method. The engineer, relying on the scientific method, looks up on his problem by first researching what already exists. This research can be looking up to the nature, searching well-established methods on books, or accessing the state-of-the-art studies on research journals. Based on this first lookup, the engineer either uses what is already available or creates an alternative solution using those as basis. Testing is fundamental. And after testing, a redesign may be necessary, looking at all that research again.

In the present thesis, it may seem that we do not look up to much to nature directly. But we do not need to look at nature for inspiration on an invention only. One may look at it to devise a mathematical model, or a numerical approach, for example. Those on who this thesis is based upon have done it, and those before that. Let us take a very clear example. In this thesis, a statistical model is utilized to account for the particle-particle collisions. The basis of the model were proposed by Oesterlé and Petitjean (1993) and Sommerfeld (2001), who utilized an analogy with the collisions of the molecules in a gas. A true mimic of the nature to model another event of the nature.

The equipment and processes this thesis is concerned about are already established. Not that there is not room for improvement, on the very contrary. We are looking for improvement. But first, we are looking for a way to better, and faster, model such equipment and processes. In the present thesis, the scientific method, the engineering design process, is in the mathematical model and in the numerical approach, not in the equipment or in the chemical process.

1.1 Background on gas-solid flows

Besides being an influential part of the nature phenomena, gas-solid flows are also very important in the industry. They can be found in virtually all sectors of a production plant, such as: (1) heating, in biomass heating systems where the solid fuel may be fluidized and the ashes from the burn are transported outside; (2) transport, that can occur as consequence of other processes or it can be used as alternative to other regular transports of solid, see for instance the transport of grains to silos; (3) reaction, many reactions are conducted under gas-solid flow, where the solid can be either a reagent, a product, or a catalyst of the reaction; and (4) in separation, some examples of gas-solid separation equipment are the cyclone, gravitational chamber, electrostatic precipitators, and others.

Gas-solid flows also appear in a wide range of solid mass loadings, from very dilute to very dense. And the flow will behave very differently depending on this condition. A good visual representation of the many flow patterns developed in gas-solid flows is presented in Figure 1. At the first end, the fixed bed regime is at a condition where the particles are refrained form moving due to a very low fluid velocity such that the drag is not high enough. As the fluid velocity is increased, the carrier fluid starts to lift some particles, and the bed expands. This expansion leaves space for the agglomeration of the fluid in bubbles, as shows the second diagram. With further advance in those conditions, the bubbles grow bigger, and can reach the slugging regime, where the bubbles of fluid are so big that they produce small bursts of solids. A little increase in velocity and the expansion of the bed is so advanced that it almost does not maintain itself in a state of particles aggregation all the time.

At the other end of the schematics lie the two patterns concerned in the present thesis, the fast fluidization and the pneumatic conveying. The former is found in risers of Circulating Fluidized Beds (CFB's), discussed in the next section, and the latter at dilute pipe particle-laden flows. At the fast fluidization, smaller cohesive particle structures

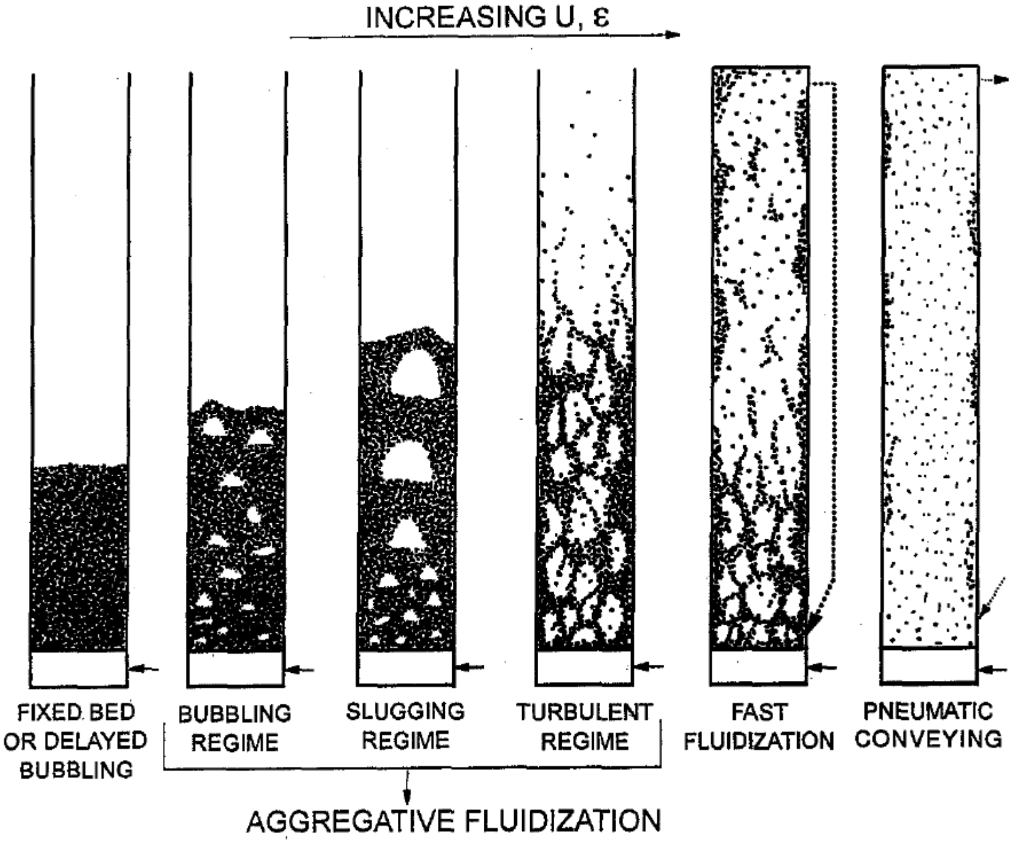

Figure 1 – Schematic diagram of the gas-solid flows patterns as function of the fluid velocity and void fraction. From Lim *et al.* (1995).

called clusters, are formed at certain locations in an intermittent manner. Particles are mostly carried upwards, but there can still be some backflow. On the very end of the fluid velocity and porosity scale, is the pneumatic conveying regime. At this stage the particles are fully carried out upwards, with almost no agglomeration of solids. Also, in this last regime, the particles are very distant from each other, configuring a very dilute flow, in opposition to the other dense flows.

It is important to note that the approach utilized to model each one of the discussed regimes is different, and also fundamental for its correct prediction. In the fixed bed regime, for instance, the particle contact is the dominant phenomena, and needs to be modelled by a very physically sound model such as the Discrete Element Model (DEM). On the other hand, the fluid turbulence is almost negligible and can be often disregarded by using the simplest turbulence closure model available or none at all. As one moves to the right in the direction of higher fluid velocities up to the turbulent regime, the particle-particle collisions importance is still maintained, but the influence of the fluid closure model also grows in importance.

While in the regime at the left end of Figure 1, the particle collisions dominate the flow and the fluid modeling is almost unimportant, on the right end the picture is the exact opposite: the modeling of the fluid-phase turbulence in the pneumatic conveying is the most influential aspect in the results. However, bear in mind that one does not necessarily need to use Direct Numerical Simulations (DNS) for it, even the Reynolds-Averaged Navier-Stokes (RANS) equations approach can suffice depending on the quality of the response that is needed. Also, in this regime particle-particle collisions are almost non-existent, such that many studies are carried out neglecting them at all, using the so-called one- or two-way coupling. Of course that in some specific cases the collisions are still important, but in a very lower level in comparison to the other regimes, in such way that simpler models are usually employed.

In the middle of this spectrum lies the fast fluidization regime. In this one, there is a mix of importance between turbulence closure and particle-particle collision modeling. As will be shown in chapter 2, there are many approaches suitable to model this flow, from very deterministic ones such as the Large Eddy Simulation (LES) for the fluid and DEM for particle contact, down to RANS/URANS with stochastic collision approaches.

1.2 Problem statement

In the present thesis, the main subject of investigation is the modeling of particle-laden flows in risers from Circulating Fluidized Bed (CFB) facilities. CFBs are equipment characterized by a multi-phase condition where solid particles are dispersed in a gas carrier phase. They are commonly employed when the particles that flow through the riser need to be recovered and fed in again into the riser, such as in reactions where the particles are the catalysts.

The literature shows that studies in CFB risers have intensified about three decades ago. Experimental investigations are usually carried out in reduced scales and the main evaluated characteristics are the particle phase dynamics (velocity, velocity fluctuations, concentration, clustering) and geometrical characteristics, employing techniques such as pressure taps, optical fiber probes, Doppler effect anemometry, particle image velocimetry, γ-ray tomography, and electrical capacitance. Together with the experimental studies, simulations also have been carried out. In computational studies the approach to model the phases has been the main object of study in the scientific community. The present thesis only focus on simulations to carry out the proposed study.

Numerical simulations of such gas-solid flows are carried utilizing two main approaches currently, the Euler-Lagrange and the Euler-Euler. In the present work, the former one is utilized for the simulation of a CFB riser. However, in this approach there are two main ways to model the gas phase flow equations, which will be considered in this work. The first one is to model it as if it was a clean flow. Despite the hypothesis being valid only in the limit of vanishing particle volume fraction, it serves as a good approximation for dilute flows. The second one is achieved by carrying out a volume-averaging operator in each cell to account for the presence of the particles in terms of volume occupied. This last one is suitable for dilute and dense flows.

Another point to consider, is that the most realistic gas-solid flows simulations utilize very computationally heavy models, such as LES or DNS for the fluid-phase, and the DEM for the particle collisions. However, such combination of models can be a barrier to the simulation of large industrial equipment. In the present thesis, a more computationally cheap modeling approach is sought, that requires significantly less computational power for its simulations. The Unsteady Reynolds-Averaged Navier-Stokes (URANS) methodology is employed for the fluid and a statistical collision model for the particles. This computationally cheaper framework benefits users requiring fast responses, such as in industrial optimization.

1.3 UNSCYFL3D: previous works and present thesis contribution

In the present thesis all simulations are carried out in the in-house code UNSCYFL3D. This code was developed in the Fluid Mechanics Laboratory (MFLab) of the School of Mechanical Engineering at the Federal University of Uberlândia under the supervision of Prof. de Souza. It is written in FORTRAN language, and it is prepared for serial processing utilizing unstructured meshes with element types such as hexahedra, tetrahedra, prisms, pyramids and wedges. The meshes are generated with the ICEMCFD software from ANSYS, and are converted to the UNSCYFL3D readable format with a small C language application. Post-processing of the results can be performed in either the VisIt or Paraview visualization softwares.

The UNSCYFL3D has a reasonable history with simulations of gas-solid flows. Some examples of validation studies are: Souza *et al.* (2012), Martins *et al.* (2014) and Souza *et al.* (2015) that carried out simulations in cyclones; Souza *et al.* (2014) who performed simulations of gas-solid flow in a diffuser validating the methodology of wall roughness; a number of gas-solid validations were also presented in congress papers for pipe and channel flows; and Pereira *et al.* (2014), Duarte *et al.* (2015), Duarte *et al.* (2017) evaluated the use of the code in erosion predictions in pipe bends. After these numerous validations, some work has also been done in order to promote geometry optimization and assess the influence of different configurations on erosion prediction (SANTOS *et al.*, 2016; DUARTE *et al.*, 2016; DUARTE; SOUZA, 2017; DUARTE *et al.*, 2019).

However, the UNSCYFL3D code was always utilized for dilute loadings of particles, using the standard equations of the Euler-Lagrange approach, where the fluid phase is solved using the single-phase fluid equations. The study that pushed the limits of applicability was also the first work of the group on CFB risers, carried out by Utzig (2016) performing comparisons with experiments in a pilot scale CFB riser built for his thesis at the Verification and Validation Laboratory (LVV) of the Chemical Engineering Department at the Blumenau University[1]. Although good results were achieved then, it was noted that the simulation of flows at higher particle mass loadings began to show more disparity, and some enhancement on the model could be necessary.

After some review of the literature, it was noted that the first step towards a modeling more suitable for dense flows should be the change of the fluid-flow equations, in order to account for the particles volume. This is the objective of the present thesis, the implementation of such model. There are also other improvements that can be made, such as the particles collision modeling, for instance. However, this will remain for future works, as also presently we still seek an approach that maintain the low computational cost of simulations.

1.4 Motivation

One of the main motivations of this study is the strong interest of the Brazilian national petroleum company - Petrobras - in the topic. One of the main applications of CFBs is in the Fluid Catalytic Cracking (FCC) process, which is largely employed in Brazilian refineries. In the FCC process heavy petroleum fractions, around C15 to C30, are vaporized into the riser together with solid catalysts to enhance the cracking reaction into lighter components, with higher aggregated value. A photography of a full CFB facility in the FCC unit of the REVAP Petrobras refinery is presented in Figure 2. The smaller vertical white pipe on the right side is the riser reactor, followed by the gas-solid separation section utilizing series of cyclones on the top, which sends the solid catalysts to the regenerator at the bottom for coal removal. The products, still in gas phase, are recovered in the equipment shown in the left side of the photography.

The FCC process has been used commercially since 1915 (SPEIGHT, 2006 apud WIKIPEDIA, 2019), and ever since experimental investigations have been carried out in order to improve it. Also, CFD simulations have been utilized since its early years to try to improve this chemical process. Nevertheless, there is still room for development, and investing in new or better ways to correctly predict such flows is still needed. Despite the recent increase in offer, demand, and research on renewable sources, petroleum will still remain extremely important in the foreseeable future. Let us look at some statistics in crude oil production in the U.S., for instance. After the production hit its peak value at 10 million barrels per day in 1970, the production fell down until the 2010's, and only recovered its mark again in 2017 (U.S. DOE, 2018). However, since then, petroleum production has only increased, successively pushing its all-time high value and hitting 13 million bbl/d in November/2019 (U.S. DOE, 2019a)[2]. Even though the production has

---

[1] FURB - University of Blumenau, located in Blumenau, state of Santa Catarina, Brazil.

[2] Statistics from U.S. were used as that is the easiest data available on the internet and they are a good

Figure 2 – A Fluid Catalytic Cracking facility from the REVAP Petrobras refinery, located in the São Paulo state in Brazil. Photography taken by Prof. Henry F. Meier, originally presented in Utzig (2016).

never been higher, the cost of oil products such as gasoline and diesel has not decreased in the last years (U.S. DOE, 2019b). In such scenario, the improvement of efficiency in oil refinement related processes is essential, and has two main benefits: cost and pollution reduction.

Benefits of the present research can also achieve other areas that not only the FCC process of the oil refinement industry. While the main application is the one just mentioned, it is not difficult to find other applications where CFB risers can be applied also playing a role of the main reactor, such as in ozone decomposition, polymerization in gaseous phase, combustors, and others (ROSSBACH *et al.*, 2019). Also, once the mathematical, numerical and computational approach is deemed suitable in the validation cases tested in the present thesis, it can be used for other dense gas-solid simulations, especially in vertical ascending flows.

---

representation of what's going on around the world. However, it is known that the production has also increased in Brazil over the last years, mainly with new wells from the pre-salt.

1.5 Objectives

Given the topics recently discussed, the main objective of the present thesis is *to consolidate a mathematical/numerical/computational model suitable for the simulation of both dilute and dense particle-laden flows, with a special look for the CFB riser of the FCC process, that is faster than the current ones.* Nevertheless, it is important to also define specific objectives that will help us and lead us to the main one, from which the present thesis is a result:

a) to validate the previously established dilute gas-solid flow formulation with all its recent modifications, and evaluate if it is or not suitable for dense flows;

b) to investigate the dynamics of the dilute particle-laden flows in horizontal and vertical pipes, assessing the influences of many parameters such as wall roughness, forces, and particle mass loading;

c) to implement a suitable mathematical model for the modeling of dense gas-solid flows under the Euler-Lagrange approach in the UNSCYFL3D code;

d) to validate the newly implemented dense formulation on the already known dilute cases, and on dense flow cases, specially in CFB risers;

e) to evaluate the limits of each formulation within its framework of modeling.

Chapter 2

Literature review

A brief literature review about three main subjects to the execution of the present thesis is presented in this chapter. The selected important topics are: (1) the suitable mathematical formulation for the modeling of dense two-phase gas-solid flows; (2) non-deterministic particle-particle collision models that provide cheaper computational cost than the deterministic ones; and (3) a discussion about the distribution of the particle volume in the containing mesh cells in order to reach a numerically stable and more accurate formulation.

In the present thesis, an evaluation of the suitability of two different formulations is carried out for dilute and dense gas-solid flows, as already introduced in the first chapter of this document. Nonetheless, as will be shown in chapter 5 after a number of simulations utilizing the dilute formulation, the dilute formulation comes as not appropriate for the modeling of CFB riser flows. To understand the main aspects necessary in order to expand the current standard Euler-Lagrange formulation in the UNSCYFL3D to a suitable formulation for dense flows in CFB risers, a brief literature review is presented in this chapter.

Two main subjects were identified as reasonable modifications to the formulation: the fluid flow equations and the particle-particle collision model. Firstly, in the fluid flow equations review it is shown that the there is not just a single suitable formulation, but many. We use the state-of-the-art literature to evaluate which seems more appropriate in order to implement it. Further discussions about the model, its derivation, and aspects of implementation are presented in the following chapters of the present thesis.

Furthermore, the particle-particle collision model is also identified as an important topic to the correct prediction of the aforementioned flows. As one of the objectives of the present thesis is to present a computational cheap model, non-deterministic models are reviewed. Although some already tested models are found in the literature, we decided to test the stochastic model from Sommerfeld (2001) that is already implemented in the UNSCYFL3D code, but which had been thoroughly employed only for dilute flows. This decision was taken both because it would be time-challenging to make two such great changes in the code in the available amount of time, for which we judged that the change in the fluid flow equations were more important, and secondly because it is also a good contribution to show the limits of application of this collision model.

A third topic is also reviewed that was found out to be necessary due to numerical difficulties encountered during the implementation of the new dense flow formulation. That is the distribution of the particle volume in all the cells that contain a part of it. It is shown by the literature that accounting the particles only by its centroid may lead to numerical issues and poor agreement. Furthermore, reviews of models in general are presented in each appropriate section of Chapters 3 and 4.

2.1 Dense formulation

The Navier-Stokes equations, which describe the flow of Newtonian fluids, are very well-know and established within the fluid dynamics literature. However, if one looks for the appropriate expressions for the case of two-phase gas solid flows with the consideration of the volume fraction of the particles, many different momentum balance equations will be found. Although just a few main works are cited as reference for such balance, the availability of models is larger. Let us take, for instance, some examples of the momentum balance for a fluid at the non-vanishing presence of solid particles that are found in works in the literature[1]:

$$\frac{\partial}{\partial t}(\rho_g \alpha_g \mathbf{u}_g) + \boldsymbol{\nabla} \cdot (\rho_g \alpha_g \mathbf{u}_g \mathbf{u}_g) = -\boldsymbol{\nabla} p + \boldsymbol{\nabla} \cdot \boldsymbol{\sigma} + \rho_g \alpha_g \mathbf{g} + \mathbf{F}_{\mathrm{gp}}\,; \tag{2.1}$$

$$\frac{\partial}{\partial t}(\rho_g \alpha_g \mathbf{u}_g) + \boldsymbol{\nabla} \cdot (\rho_g \alpha_g \mathbf{u}_g \mathbf{u}_g) = -\alpha_g \boldsymbol{\nabla} p + \alpha_g \boldsymbol{\nabla} \cdot \boldsymbol{\sigma} + \rho_g \alpha_g \mathbf{g} + \mathbf{F}_{\mathrm{gp}}\,; \tag{2.2}$$

$$\frac{\partial}{\partial t}(\rho_g \alpha_g \mathbf{u}_g) + \boldsymbol{\nabla} \cdot (\rho_g \alpha_g \mathbf{u}_g \mathbf{u}_g) = -\boldsymbol{\nabla} p + \boldsymbol{\nabla} \cdot (\alpha_g \boldsymbol{\sigma}) + \rho_g \alpha_g \mathbf{g} + \mathbf{F}_{\mathrm{gp}}\,; \tag{2.3}$$

$$\frac{\partial}{\partial t}(\rho_g \alpha_g \mathbf{u}_g) + \boldsymbol{\nabla} \cdot (\rho_g \alpha_g \mathbf{u}_g \mathbf{u}_g) = -\alpha_g \boldsymbol{\nabla} p + \boldsymbol{\nabla} \cdot (\alpha_g \boldsymbol{\sigma}) + \rho_g \alpha_g \mathbf{g} + \mathbf{F}_{\mathrm{gp}}\,; \tag{2.4}$$

where the main difference lies on the relation of the fluid volume fraction α_g with the pressure p and shear stress tensor $\boldsymbol{\sigma}$ as seen on the two first terms on the RHS of the equations above.

---

[1] The momentum balance is presented here only to better show the differences seen in literature. The more appropriate discussion about this equation is presented later in this thesis in chapter 3.

There is some degree of freedom in these equations because the way that the fluid-particle interaction term $\mathbf{F}_{\mathrm{gp}}$ is accounted for may change, but only within the limits of a mathematic algebraic equivalence. For instance, 2.1 and 2.2, that are usually utilized in the Euler-Lagrange approach and credited to Anderson and Jackson (1967), are shown to be mathematically equivalent by the authors themselves and others (CROWE *et al.*, 2011; CAPECELATRO; DESJARDINS, 2013) if $\mathbf{F}_{\mathrm{gp}}$ is properly modeled, such that it would assume different formulations in each model. Also, Zhou *et al.* (2010) has shown its equivalence by carrying out numerical simulations utilizing these two formulations for the modeling of a bubbling fluidized bed, a horizontal pneumatic conveying pipe, and in a hydrocyclone.

However, even such apparent well-posedness of Anderson and Jackson (1967) formulation does generate confusion in the literature. It is not difficult to find studies in the recent literature that cite their work as reference for the formulation utilized, but in fact present equations such as 2.3 or 2.4. One could argue that 2.3 or 2.4 could be also equivalent to the two others if $\mathbf{F}_{\mathrm{gp}}$ were to be changed as before, but that is not true, as shown by means of comparing simulations of bubbling fluidized beds in Kafui *et al.* (2002). See also Feng and Yu (2004b) and Kafui *et al.* (2004), that are related to this paper. Furthermore, it would seem odd, under the perspective of an Euler-Lagrange derivation, that α_g could be multiplying p and $\boldsymbol{\sigma}$ differently since they can be treated together under the perspective a full stress tensor $\boldsymbol{\tau}$ that aggregates the normal and tangential stresses, if not for some simplification during the derivation or posteriorly.

However, in works that utilize the Euler-Euler approach such difference in modeling is more reasonable, because there are some considerations made during the derivation concerning the pressure of the solid phase, which is treated as a hypothetic fluid. This difference, more often than not, leads to such papers citing the works of Gidaspow (1994) and Enwald *et al.* (1996) as references, and presenting either formulation 2.3 or 2.4. Nonetheless, Feng and Yu (2004a) has shown that 2.3 or 2.4 are differently by assessing each one in the simulation of a bubbling fluidized bed.

So, in order to remove any possibility of a premature choice of formulation leading to an erroneous simulation, and given the recent analysis, in the present thesis the formulation of Anderson and Jackson (1967) was chosen because it seems that its derivation has more proximity to the Euler-Lagrange approach. Also, the work Capecelatro and Desjardins (2013) has performed a good review of their derivation arriving at the same equations and discussing its terms, which gives more confidence in utilizing the right equations. In an independent work of formulating the two-phase flow equations for an Euler-Lagrange approach, Crowe *et al.* (2011) also arrive at the same equations by a different method. Finally, Chu and Prosperetti (2016) utilizing yet another derivation procedure, arrived at its own equations that confirm the relationship of α_g, p, and $\boldsymbol{\sigma}$ in the same way that it is shown by Anderson and Jackson (1967). More discussion is presented in section 3.2.

2.2 Particle-particle collision models

When it comes to the modeling of the particle-particle collisions in dense flows such as in CFB risers, there is a natural preference to deterministic approaches. Those two most utilized nowadays are the hard-sphere and the soft-sphere approaches (also called the Discrete Element Method - DEM). These two methods are based on modeling the actual collision by either checking the crossing of all particle trajectories or by resolving most of the collision process itself. Although they are the most accurate collision models, the computational cost of such calculations are very high, what often makes their use prohibitive for simulations of large equipment.

Also, some computational cost reduction techniques such as the so-called coarse-graining, representation of multiple particles by one computational parcel, are generally not suitable due to these models nature. In fact, some coarse-graining is allowed in the DEM, but it is carried out by artificially increasing the particle diameter (PATANKAR; JOSEPH, 2001; CHU *et al.*, 2009; SAKAI *et al.*, 2010; LU *et al.*, 2014; PENG *et al.*, 2015; LU *et al.*, 2018), which does not reduce cost very much and also does not help on relaxing the time-step limitation.

As an alternative to provide computationally cheap tools for the simulation of such cases, some non-deterministic models have arisen. Two of the most utilized are the Dense Discrete Phase Model (DDPM) and the MultiPhase Particle-In-Cell (MP-PIC, or MPPIC). In these models, particle variables calculated inside the Eulerian framework are utilized to determine a force of collision on a cell basis, instead of checking each particles trajectory or proximity to other particles. Also, the parcel approach is naturally applicable and larger time-steps than in the DEM approach can be utilized, which help reducing drastically the computational cost.

Another collision model that has been extensively employed in the UNSCYFL3D code for dilute flows, and is suggested in the present thesis for dense flows as well, is the stochastic collision model from Sommerfeld (2001). In this model, the actual collision dynamics that govern the post-collisional velocities of the particles is solved by the classical hard-sphere model. However, the computational heavy part that is the collision checking by crossing all particle trajectories is removed, by deciding the collisions based on statistics. Let us get a better review of the aforementioned models in order to understand each ones weaknesses and strengths.

2.2.1 Deterministic models

In the hard-sphere approach[2], the post-collisional particle velocities are related to the pre-collisional ones by a classical mechanics impulsive force balance around the moment of the collision:

$$\begin{aligned} m_{p,1}\Big(\mathbf{u}_{p,1}-\mathbf{u}^0_{p,1}\Big) &= \mathbf{J}\,, \\ m_{p,2}\Big(\mathbf{u}_{p,2}-\mathbf{u}^0_{p,2}\Big) &= -\mathbf{J}\,, \\ I_{p,1}\Big(\boldsymbol{\omega}_{p,1}-\boldsymbol{\omega}^0_{p,1}\Big) &= \frac{d_{p,1}}{2}\mathbf{n}\times\mathbf{J}\,, \\ I_{p,2}\Big(\boldsymbol{\omega}_{p,2}-\boldsymbol{\omega}^0_{p,2}\Big) &= \frac{d_{p,2}}{2}\mathbf{n}\times\mathbf{J}\,, \end{aligned} \tag{2.5}$$

where m_p is the particle mass, I_p is the particle moment of inertia, $\mathbf{u}_p$ is the particle linear velocity, $\boldsymbol{\omega}_p$ is the particle angular velocity, $\mathbf{J}$ is the impulsive force at the contact, and $\mathbf{n}$ is the normal vector connecting particles 1 and 2 at the contact.

As one can note, the impulsive force balance is made around two colliding particles, so that it imposes a limitation on this method already, for multiple collisions. For this reason this approach is used less in very dense flows like bubbling fluidization, and more in fast fluidization (HE *et al.*, 2009) or even dilute flows (MALLOUPPAS; WACHEM, 2013; ALLETTO; BREUER, 2013). To apply the balance above, the collision have to be checked by crossing the trajectories of pairs of particles, which make the computational cost very high.

The more complete, and more utilized, deterministic approach is the DEM (CUNDALL; STRACK, 1979; TSUJI *et al.*, 1993), where all the contact between the particles is modeled. This method is applied by checking the proximity of the particles, if the distance is less than the radii sum then they are touching each other and the model starts to be accounted. This allows for multiple collisions to be handled at the same time. Note that the deformation of the particles is not fully resolved, but it is modeled utilizing a spring-dashpot system to account for the collision force in the normal $\mathbf{F}_n$ and tangential direction $\mathbf{F}_t$:

$$\mathbf{F}_n = \Big(-k_n\delta_n^{3/2} - \eta_n\mathbf{G}\cdot\mathbf{n}\Big)\mathbf{n}\,; \tag{2.6}$$

$$\mathbf{F}_t = \begin{cases} -k_t\delta_t - \eta_t\mathbf{G}_{ct}, & \text{if } \|\mathbf{F}_t\| < f\|\mathbf{F}_n\|\,, \\ f\|\mathbf{F}_n\|\mathbf{t}, & \text{otherwise}\,; \end{cases} \tag{2.7}$$

where k is the spring constant, η is the damping coefficient, f is the tangential friction factor, δ is the overlapping distance of the particles, $\mathbf{G}$ and $\mathbf{G}_{ct}$ are the relative velocities, and $\mathbf{n}$ and $\mathbf{t}$ are the collision unit vectors in the normal and tangential direction. For the tangential force, the simpler form $\mathbf{F}_t = f\|\mathbf{F}_n\|\mathbf{t}$ is usually preferred, as the calculation of the first condition of equation Equation 2.7 is computationally complex and generally does not make much difference (CAPECELATRO; DESJARDINS, 2013).

---

[2] Extended discussion in subsection 3.3.2

As the relation between force and displacement is not linear, and there is the possibility of multiple contacts, all the collision process has to be modeled, from the approach to the overlapping, up to the detachment of the particles. As a consequence, in order to account for the whole process in an accurate manner, very small time-steps are required since the deformation of solid particles is very limited. Not rarely, studies utilize artificially smaller coefficients in order to allow for bigger time-steps and speed up the simulations. For the reasons above, the DEM has seen more use in small bubbling fluidized beds analysis (CHIESA *et al.*, 2005; RENZO; MAIO, 2007; MÜLLER *et al.*, 2009; PEPIOT; DESJARDINS, 2012; ALOBAID; EPPLE, 2013; LU *et al.*, 2017; LU *et al.*, 2018) and simplified CFB risers (ZHAO *et al.*, 2010; CAPECELATRO *et al.*, 2014; LU *et al.*, 2014; CARLOS VARAS *et al.*, 2017a).

One advantage from the deterministic models in comparison to the non-deterministic ones is that usually the constants and coefficients of the model come from the materials themselves. In the hard-sphere approach, for instance, the calculation of the impulsive force depends on the restitution and friction coefficient, that can be determined experimentally from the controlled collision of particles. On the other hand, in the DEM the coefficients presented above can be calculated from the Young's modulus and Poisson ration of the material that constitutes the particles.

2.2.2 DDPM

The DDPM (POPOFF; BRAUN, 2007) can be thought of as a midway formulation between the Euler-Euler Two-Fluid Model (TFM) and the Euler-Lagrange approaches, such that some authors name it as an Euler-Euler-Lagrange method (CLOETE *et al.*, 2012). To clarify, the DDPM is in fact (in the present author's view) an Euler-Lagrange based approach, where the fluid phase is solved under the Eulerian framework, and the particles (or parcels) are solved as single entities under the Lagrangian point of view utilizing the classical Newton equations. However, the information from the particle-particle collisions is carried out in a modeled manner, in accordance to the Kinetic Theory of Granular Flows (KTGF) method (HOEF *et al.*, 2006), which was essentially devised for TFM simulations.

Some straight benefits of this change in modeling perspective, from using the KTGF in the Euler-Euler TFM to using it in a EL-based framework, are (CLOETE *et al.*, 2012):

a) no numerical diffusion in the particle volume fraction field;

b) easier inclusion of more particle sizes;

c) better modeling of particle-wall interaction.

In the EL approach the volume fraction is not updated by a transport equation as in the EE, which would be subject to numerical diffusion because of the discretization, but rather is directly inferred from the particle positions in relation to the mesh cells. Also, another important critical to the EE-TFM approach is the large increase in computational cost for accounting multiple particle sizes. For each particle diameter, another set of transport equations has to be added, and the interaction between this diameters modeled. Lastly, as in the EE the particle phase is modeled as a hypothetic fluid, there is no way to account for the particle-wall collisions in a deterministic way, and one more model has to be taken.

The DDPM has been utilized with success for CFB riser simulations (ADAMCZYK *et al.*, 2014; KLIMANEK *et al.*, 2015; ADNAN *et al.*, 2018) and also other general gas-solid flows (CLOETE *et al.*, 2012; CHEN; WANG, 2014). However, this model is most exclusively available in the ANSYS FLUENT solver. This imposes some restrictions in order to implement the model in other codes. The KTGF is a computational heavy model, in the sense that it has many equations with closure models, that if not properly selected and carefully implemented may present many convergence problems. In addition to the KTGF itself, there is the accounting of the KTGF force into the Lagrangian modeling, that also needs to be properly manipulated.

Let us review some equations to understand the statement above. In the DDPM collision modeling approach, one assumes a proportionality between the collision force and the gradient of the solid phase stress tensor. The stress tensor is calculated based on the KTGF theory that states that this tensor comes from the particle collisions and translations. The force is translated into the Lagrangian framework as

$$\mathbf{F}_{\mathrm{KTGF}} = -\frac{1}{\rho_p}\boldsymbol{\nabla}\boldsymbol{\tau}_s\,, \tag{2.8}$$

using the solids stress tensor $\boldsymbol{\tau}_s$ analogy to the fluid stress tensor that comes from the KTGF theory:

$$\boldsymbol{\tau}_s = -p_p\mathbf{I} + \alpha_p\mu_p\Big[\boldsymbol{\nabla}\mathbf{u}_p + (\boldsymbol{\nabla}\mathbf{u}_p)^{\mathrm{T}}\Big] + \alpha_p\Big(\lambda_p - \frac{2}{3}\mu_p\Big)(\boldsymbol{\nabla}\cdot\mathbf{u}_p)\mathbf{I}\,. \tag{2.9}$$

where α_p is the particle volume fraction and $\mathbf{I}$ is the identity matrix. The solids pressure p_p, the solids viscosity μ_p, and the bulk viscosity λ_p are all dependent on closure models that are function of the granular temperature θ_p.

The KTGF granular temperature is a measurement of the particles fluctuation velocity, which resembles the fluid turbulence kinetic energy k. In fact, the transport equation of θ_p is similar to the transport equations for fluid turbulence transported variables, such as k and ε. So, despite DDPM being an advance in the reduction of computational cost in relation to the classical TFM-KTFG, it stills has an overhead of computation with the addition of one more transport equation.

2.2.3 MP-PIC

The MP-PIC (ANDREWS; O'ROURKE, 1996; SNIDER, 2001) is very similar, in conception, to the DDPM. The Euler-Lagrange is utilized in its standard way, and the particle-particle collisions are modeled by a force proportional to the gradient of the solids stresses:

$$\mathbf{F}_{\text{MP-PIC}} = -\frac{1}{\rho_p \alpha_p} \boldsymbol{\nabla} \tau_s \,. \tag{2.10}$$

The modeling of this stress, however, is different, and follows the equation:

$$\tau_s = \frac{P_s \alpha_p^\beta}{\max\left[\alpha_{p,\text{cp}} - \alpha_p, \epsilon(1-\alpha_p)\right]} \,, \tag{2.11}$$

where P_s is a constant with units of pressure that are usually between 1 and 100 Pa, β is also another constant with recommended values ranging from 2 to 5, $\alpha_{p,\text{cp}}$ is the particle volume fraction at the close packing limit (approximately 0.64), and ϵ is a very small number $\mathcal{O}(10^{-7})$ in order to avoid singularities in the division when near the close packing limit.

The majority of the studies carrying out MP-PIC simulations are performed in only two softwares, Barracuda[3] and MFIX[4]. The Barracuda was co-founded and is co-owned by one of the original authors of the method, Dr. Dale Snider (SNIDER, 2001; O'ROURKE; SNIDER, 2012), and is often called in the literature as Computational Particle Fluid Dynamics (CPFD). The MFIX is based on the previously cited references, but in its documentation (GARG; DIETIKER, 2013) show that many modifications had to be made in order to get a stable solver.

Although the implementation of this model seems easy because the sole addition of the aforementioned force in the on the particle linear velocity equation, it is not. This force cannot be simply numerically integrated alongside with the other forces such as drag. Snider (2001) and Garg and Dietiker (2013) show specific methods to do this calculation. There are also many special conditions to be taken into account such as the sign of τ_s in Snider (2001) implementation, or the sign of the relative velocity and τ_s in Garg and Dietiker (2013) implementation. There are also many numerical aspects in Snider (2001) original implementation that make this model difficult to implement solely on its paper description. Some are addressed in Garg and Dietiker (2013), but it is still complex. For instance, they write that the form of the stress tensor does not matter, and a simple coloring function could be used instead to achieve the same results.

Despite this computational complication, there are many successful studies in those two softwares in the simulation of general fluidizations (ABBASI *et al.*, 2011; WEBER *et al.*, 2013; LIANG *et al.*, 2014; SOLNORDAL *et al.*, 2015a; SONG *et al.*, 2018), CFB risers (LI *et al.*, 2012; CHEN *et al.*, 2013; SHI *et al.*, 2015a; SHI *et al.*, 2015b; WANG *et al.*, 2015; ZHANG; YOU, 2016; BERROUK *et al.*, 2017; XIE *et al.*, 2018) and even full CFB loops (JIANG *et al.*, 2014; WANG *et al.*, 2014b; WANG *et al.*, 2014a).

---

[3] Available at <https://cpfd-software.com/>.

[4] Available at <https://mfix.netl.doe.gov/>.

2.2.4 Sommerfeld's stochastic collision

Another alternative that is also a suitable model for parcel formulation and presents low computational cost such as the DDPM and the MP-PIC, is the stochastic collision model from Sommerfeld (2001). This model is already implemented in the UNSCYFL3D, and has been consistently utilized for handling particle-particle collisions in dilute flows by the present research group (see works previously cited in section 1.3) and Prof. Dr. Sommerfeld's as well (LAÍN; SOMMERFELD, 2008; LAÍN; SOMMERFELD, 2012; LAÍN; SOMMERFELD, 2013). However, to the best of the authors knowledge, there is no study with it in dense flows or in CFB risers. For this reason, this model is suggested in the present thesis to be tested in such flows as a computational cheap substitute.

This model is based on the deterministic hard-sphere collision model to calculate the particles post-collisional velocities, but the realization of the collisions is carried out in a stochastic way, instead of crossing all particle trajectories. A chance of collision is calculated based on the particle concentration field by an analogy to the kinetic theory of the gases. If the collision occurs, a fictitious partner has to be generated utilizing statistical distributions. As this model is already part of UNSCYFL3D, and will be utilized for the present thesis, a more complete discussion is presented in subsubsection 3.3.2.1.

2.3 Particle volume distribution

An important assumption in the Euler-Lagrange approach is that the particles are much smaller than the cells of the mesh, such that the concepts of point-force and the filters for the volume-averaged equations may hold true. However, such condition can not be always guaranteed. In the present thesis, for instance, it is very common that the near-wall cells are smaller than the particles, due to a required refinement that is followed due to the turbulence closure modeling. Another problem to this condition, comes from the representation of multiple real particles by computational parcels. It is common that the volume represented by one parcel can also exceed the volume of the smaller cells.

The most simple and utilized practice is to account each particle in the cell which hosts its centroid, namely the Particle Centroid Method (PCM). This is utilized to define which cell will receive the particle volume for the accounting of the cell volume fraction, and also to account the gas-particle interaction term. However, it has been shown that utilizing the PCM method in cases where the particles are larger or the same order of the cell size can cause erroneous results (PENG *et al.*, 2014; SUN; XIAO, 2015a) and numerical instability (PENG *et al.*, 2014).

Peng *et al.* (2014) has carried out simulations of a bubbling fluidized bed with the DEM collision modeling in multiple cell sizes, and compared the PCM with an analytical distribution approach. In the analytical approach, the cell volume and interaction force contributions are divided in real proportion to each cell that contain a piece of the particle, making it the most accurate method when applicable. The authors found out that up to a cell-to-particle size ratio of 3.8 the PCM would provide unrealistic local values of pressure and mass flow, while the analytical approach would not. In a similar case, Sun and Xiao (2015a) also showed the inconsistency of the PCM for relatively small cells in comparison to a diffusion-based method. This diffusion-base method will be discussed shortly along other commonly applied methods.

2.3.1 Analytical approach

The analytical approach is the theoretically most accurate way to account for the distribution of the particle volume. In this method, the true division of the particle is carried out, assigning each piece to the appropriate hosting cell. Although the analytical approach should be the sought methodology for all simulations, its implementation is very complex, and sometimes impossible for unstructured meshes. Most works that apply this method, are carried out in a 2D domain or 3D but with a totally cartesian mesh (PENG *et al.*, 2014).

Wu *et al.* (2009), to the best of the authors knowledge, were the only ones to propose an analytical decomposition to tetrahedral cells[5]. However, to account for the many possible cell shapes available, more work is needed. Also, the implementation of such method does not fall short from complex, which stills make this method mostly not preferable.

2.3.2 Statistical kernel

Another method of particle distribution comes from the employment of statistical kernel functions. The particle volume fraction or the gas-particle interaction term are given by a weighted sum such as

$$\alpha_p(\mathbf{x}) = \sum_{i=1}^{N_p} V_{p,i} g_i \,, \tag{2.12}$$

where N_p is the total number of particles and $g_i = g(\|\mathbf{x} - \mathbf{x}_i\|)$ is a statistical kernel such as the top-hat or the Gaussian-like distribution functions. This will distribute the volume and force of the particle in all cells around the host cell according weight given by the selected kernel as a function to the cell-to-cell distance.

This method is significantly easier to implement than the analytical one, while still retaining a very good distribution. Some examples of this are available in Xiao and Sun (2011), Evrard *et al.* (2019). However, the treatment of the boundaries is difficult (SUN; XIAO, 2015b).

---

[5] Also confirmed by Sun and Xiao (2015b). No others works in this field were found by us since then.

2.3.3 Diffusion based

The diffusion based method (CAPECELATRO; DESJARDINS, 2013; SUN; XIAO, 2015b) is an approximation to the statistical kernel approach. In this method, the particle volume fraction and the gas-particle interaction force are first calculated as in the PCM method. After that, a diffusion equation is solved for this variable, so the quantity is smoothed over all the neighboring cells. Of course this diffusion has to be controlled so that the influence is not spread over all the domain. Both Capecelatro and Desjardins (2013) and Sun and Xiao (2015b) provide expressions for the calculation of a suitable total time of diffusion, such that the same stencil as in the statistic kernel is reached.

This method provides the same distribution as the statistical kernel method for small and medium cells, and a little more spread in large ones. However, it is also much easier to implement than the other ones, given that the discretization of a transient diffusion equation is not complex in the FVM, and all the basis for this are already laid in the computational code. Also, it overcomes the problem at the boundary conditions. For such reasons, this method is implemented in the UNSCYFL3D for the present thesis, and a more thorough discussion is presented in subsection 4.2.4.

Chapter 3

Mathematical modeling

The full set of equations with their appropriate closure models, needed to solve both dilute and dense flows are presented here. The differences between the two models are emphasized for a better understanding of their characteristics.

There are many notable differences between the dilute and dense formulation for gas solid-flows in both the gas phase and in the particle phase equations, mainly concerning the inclusion of the particle volume fraction. However both of them are solved in the same Euler-Lagrange framework. The Eulerian approach is applied to the gas phase using continuum transport equations to describe the flow, whereas the particle phase is described in a Lagrangian approach where each particle is represented as a single entity with its own set of position and velocities vector.

3.1 Dilute flows

Strictly speaking, the use of the equations that are introduced in the present section for gas-solid flows would require particle surface-resolving approaches. However, such approaches are still restricted to a very reduced number of particles. See, for instance, the simulations of Yeo and Maxey (2010) using a few more than 4000 particles and Vreman (2016) with no more than 128 particles. Given this restriction, it is a common and acceptable practice throughout the literature to use the point-wise equations of motion in dilute flows without much harm to accuracy. There is no hard limit for the validity of this simplification, Crowe *et al.* (2011) show that it may vary for particle volume fraction values from 10^{-3} up to 10^{-1}, and Vreman *et al.* (2004) concluded that the inclusion of the spatial variation of the particle volume fraction in the fluid equations for particle-laden channel flow computations, had no significant effects for values up to 0.013.

3.1.1 Gas phase formulation

The gas phase formulation is presented here in two parts. Firstly, the point-wise equations that describe the fluid flows are introduced. After that, the mathematical procedure to allow the proper solution of turbulence in large geometries and high Reynolds flows is presented, together with the turbulence closure model utilized in the present thesis.

3.1.1.1 Point-wise equations

The differential equations that represent a generic fluid flow are known since the middle of the 19th century, after the closure of Cauchy's momentum equation by Navier and Stokes. The equations are considered common knowledge in this field and can be recalled from any fluid dynamics or transport phenomena textbook, for instance Bird *et al.* (2002) and White (2006). In the present thesis, the gas phase is modeled by this set of mass and momentum balances, also called point-wise equations to differentiate from the volume-averaged ones presented later. Let them be, respectively:

$$\frac{\partial \rho_g}{\partial t} + \boldsymbol{\nabla} \cdot (\rho_g \mathbf{u}_g) = 0 \tag{3.1}$$

and

$$\frac{\partial}{\partial t}(\rho_g \mathbf{u}_g) + \boldsymbol{\nabla} \cdot (\rho_g \mathbf{u}_g \mathbf{u}_g) = \boldsymbol{\nabla} \cdot \boldsymbol{\tau}_g + \rho_g \mathbf{g} + \mathbf{F}\,, \tag{3.2}$$

where ρ_g is the gas density, $\mathbf{u}_g$ is the gas velocity, the full stress tensor $\boldsymbol{\tau}_g$ is

$$\boldsymbol{\tau}_g = -p\mathbf{I} + \mu\left[\boldsymbol{\nabla}\mathbf{u}_g + (\boldsymbol{\nabla}\mathbf{u}_g)^{\mathrm{T}}\right] - \left(\frac{2}{3}\mu - \kappa\right)(\boldsymbol{\nabla} \cdot \mathbf{u}_g)\mathbf{I}\,, \tag{3.3}$$

$\mathbf{g}$ is the gravity vector, $\mathbf{F}$ is any source term due to non-resolved phenomena, p is the pressure, $\mathbf{I}$ is the identity matrix, μ is the gas molecular viscosity and κ is the dilatational viscosity.

Equations 3.1, 3.2 and 3.3, can be further simplified by assuming ρ_g and μ as constants, and taking $\mathbf{F}$ to be only the gas-particle interaction force ($\mathbf{F}_{\mathrm{gp}}$). After these assumptions, the mass and momentum balances become

$$\boldsymbol{\nabla} \cdot \mathbf{u}_g = 0 \tag{3.4}$$

and

$$\rho_g\left[\frac{\partial \mathbf{u}_g}{\partial t} + \boldsymbol{\nabla} \cdot (\mathbf{u}_g \mathbf{u}_g)\right] = -\boldsymbol{\nabla} p + \mu \boldsymbol{\nabla} \cdot \left[\boldsymbol{\nabla}\mathbf{u}_g + (\boldsymbol{\nabla}\mathbf{u}_g)^{\mathrm{T}}\right] + \rho_g \mathbf{g} + \mathbf{F}_{\mathrm{gp}}\,, \tag{3.5}$$

Where Equation 3.4 has also been used as a restriction to simplify Equation 3.3. Another simplification is usually carried out identifying the following mathematical equivalence that appears in Equation 3.5:

$$\boldsymbol{\nabla} \cdot \left[(\boldsymbol{\nabla}\mathbf{u}_g)^{\mathrm{T}}\right] = \boldsymbol{\nabla}(\boldsymbol{\nabla} \cdot \mathbf{u}_{\mathbf{b}})\,, \tag{3.6}$$

which, in turn, is equal to zero after Equation 3.4. However, retaining this term is needed due to the treatment of the turbulence closure as will be presented in the next subsubsection, because such approach will introduce a viscosity that is not constant.

3.1.1.2 Turbulence closure

Although Equations 3.4 and 3.5 are suitable for solving any fluid flow, their use is conditioned to time and spatial scales sufficiently small as the Kolmogorov structures, configuring the so called Direct Numerical Simulation (DNS). Given the expensive computational requirement of this approach for large geometries and high Reynolds number flows, in the present thesis the Unsteady Reynolds-Averaged Navier-Stokes (URANS) approach is followed. In the URANS approach, equations are written in terms of filtered/averaged quantities instead of instantaneous ones, which can, in turn, be solved in a more realistic framework of time and spatial scales. This methodology is well-known and widely accepted in the turbulence modeling literature (WILCOX, 1993; POPE, 2000; LESIEUR, 2008; DAVIDSON, 2019), but a brief summary is given here for the sake of completeness.

First of all, the Reynolds decomposition is applied in Equations 3.4 and 3.5 by replacing all variables into a sum of its filtered value plus a fluctuation value, generically $f = \overline{f} + f'$. Note that this development is usually called the Reynolds averaging procedure, as it was first introduced for steady state equations. However, as in this case it is used for transient equations, the more correct mathematical procedure is the filtering (which reduces to a simple average in a steady-state case). After applying the decomposition, a filter of any kind (temporal, spatial, ensemble) is applied that meets the following properties:

$$\begin{aligned} \overline{\overline{f} + f'} &= \overline{\overline{f}} + \overline{f'}\,, \\ \overline{\overline{f} f'} &= \overline{\overline{f}}\; \overline{f'}\,, \\ \overline{\overline{f}} &= \overline{f}\,, \\ \overline{f'} &\approx 0\,, \end{aligned} \tag{3.7}$$

and is also commutative to differential operators. As in the present thesis the physical properties of the fluid phase were taken as constants, the decomposition only needs to be applied on the gas velocity and pressure, resulting in:

$$\boldsymbol{\nabla}\cdot\left(\overline{\overline{\mathbf{u}_g} + \mathbf{u}_g'}\right) = 0\,, \tag{3.8}$$

and

$$\begin{aligned} \rho_g\left[\frac{\partial}{\partial t}\left(\overline{\overline{\mathbf{u}_g} + \mathbf{u}_g'}\right) + \boldsymbol{\nabla}\cdot\left(\overline{\mathbf{u}_g\mathbf{u}_g}\right)\right] &= -\boldsymbol{\nabla}\left(\overline{\overline{p} + p'}\right) \\ &\quad + \mu\boldsymbol{\nabla}\cdot\left[\boldsymbol{\nabla}\left(\overline{\overline{\mathbf{u}_g} + \mathbf{u}_g'}\right) + \left(\boldsymbol{\nabla}\left(\overline{\overline{\mathbf{u}_g} + \mathbf{u}_g'}\right)\right)^{\mathrm{T}}\right] + \rho_g\mathbf{g} + \mathbf{F}_{\mathrm{gp}}\,, \end{aligned} \tag{3.9}$$

which will be further simplified using conditions given in Equation 3.7.

The filter applied to the dyadic product in the advective term of Equation 3.9

results in the following non-vanishing terms after simplification:

$$\begin{aligned}\overline{\mathbf{u}_g\mathbf{u}_g} &= \overline{(\overline{\mathbf{u}_g} + \mathbf{u}_g')(\overline{\mathbf{u}_g} + \mathbf{u}_g')} \\ &= \overline{\overline{\mathbf{u}_g}\ \overline{\mathbf{u}_g}} + 2\overline{\overline{\mathbf{u}_g}\mathbf{u}_g'} + \overline{\mathbf{u}_g'\mathbf{u}_g'} \\ &= \overline{\mathbf{u}_g}\ \overline{\mathbf{u}_g} + \overline{\mathbf{u}_g'\mathbf{u}_g'}\,,\end{aligned} \tag{3.10}$$

where the last term in the previous equation is the so called Reynolds tensor and cannot be solved directly. The Boussinesq assumption is used as closure model for this term:

$$\overline{\mathbf{u}_g'\mathbf{u}_g'} = -\frac{\mu_t}{\rho_g}\Big[\boldsymbol{\nabla}\overline{\mathbf{u}_g} + (\boldsymbol{\nabla}\overline{\mathbf{u}_g})^{\mathrm{T}}\Big] + \frac{2}{3}k\mathbf{I}\,, \tag{3.11}$$

where μ_t is the turbulent or eddy viscosity and $k = \frac{1}{2}\overline{\left\|\mathbf{u}_g'\right\|^2}$ is the turbulence kinetic energy. Note that the eddy viscosity is not a physical property of the fluid, but rather a function of the flow, and must also be modeled by the so called turbulence closure models. The turbulence closure model will also have to be written as function of k, so that the unknown variables do not appear in the equation. See subsubsubsection 3.1.1.2.1.

Finally, the mass and momentum balances become

$$\boldsymbol{\nabla}\cdot\overline{\mathbf{u}_g} = 0\,, \tag{3.12}$$

and

$$\rho_g\left[\frac{\partial\overline{\mathbf{u}_g}}{\partial t} + \boldsymbol{\nabla}\cdot(\overline{\mathbf{u}_g}\ \overline{\mathbf{u}_g})\right] = -\boldsymbol{\nabla}\Big(\overline{p} + \frac{2}{3}\rho_g k\Big) + \boldsymbol{\nabla}\cdot\Big[\mu_{\text{eff}}\Big(\boldsymbol{\nabla}\overline{\mathbf{u}_g} + (\boldsymbol{\nabla}\overline{\mathbf{u}_g})^{\mathrm{T}}\Big)\Big] + \rho_g\mathbf{g} + \mathbf{F}_{\text{gp}}\,, \tag{3.13}$$

where $\mu_{\text{eff}} = \mu + \mu_t$ is the effective viscosity and it is left inside the divergence operator because μ_t is a function of space, even though μ is constant. Another common practice is to take the sum inside the first gradient term on the RHS as $P = \overline{p} + \frac{2}{3}\rho_g k$, and solve it together as a single variable. Also, for simplicity after all mathematical manipulations, the overline in the filtered velocity $\overline{\mathbf{u}_g}$ is dropped and it is written as $\mathbf{U}_g$, resulting in:

$$\boldsymbol{\nabla}\cdot\mathbf{U}_g = 0\,, \tag{3.14}$$

and

$$\rho_g\left[\frac{\partial\mathbf{U}_g}{\partial t} + \boldsymbol{\nabla}\cdot(\mathbf{U}_g\mathbf{U}_g)\right] = -\boldsymbol{\nabla}P + \boldsymbol{\nabla}\cdot\Big[\mu_{\text{eff}}\Big(\boldsymbol{\nabla}\mathbf{U}_g + (\boldsymbol{\nabla}\mathbf{U}_g)^{\mathrm{T}}\Big)\Big] + \rho_g\mathbf{g} + \mathbf{F}_{\text{gp}}\,. \tag{3.15}$$

3.1.1.2.1 Standard k-ε model

In the k-ε family of turbulence closure models, the eddy viscosity μ_t is calculated from the algebraic relation

$$\mu_t = C_\mu\rho_g\frac{k^2}{\varepsilon} \tag{3.16}$$

between the turbulence kinetic energy k and its dissipation rate

$$\varepsilon = \frac{\mu}{\rho_g} \overline{\left\| \boldsymbol{\nabla} \mathbf{u}_g' : \boldsymbol{\nabla} \mathbf{u}_g' \right\|} \,,$$

where $C_\mu = 0.09$. These quantities are, in turn, determined from the solution of the following transport equations:

$$\rho_g \left[\frac{\partial k}{\partial t} + \boldsymbol{\nabla} \cdot (\mathbf{U}_g k) \right] = \boldsymbol{\nabla} \cdot \left[\left(\mu + \frac{\mu_t}{\sigma_k} \right) \boldsymbol{\nabla} k \right] + P_k - \rho_g \varepsilon + S_k \tag{3.17}$$

and

$$\rho_g \left[\frac{\partial \varepsilon}{\partial t} + \boldsymbol{\nabla} \cdot (\mathbf{U}_g \varepsilon) \right] = \boldsymbol{\nabla} \cdot \left[\left(\mu + \frac{\mu_t}{\sigma_\varepsilon} \right) \boldsymbol{\nabla} \varepsilon \right] + C_{\varepsilon,1} \frac{\varepsilon}{k} P_k - C_{\varepsilon,2} \rho_g \frac{\varepsilon^2}{k} + S_\varepsilon \,, \tag{3.18}$$

where

$$P_k = \mu_{\text{eff}} \left[\left(\boldsymbol{\nabla} \mathbf{U}_g + (\boldsymbol{\nabla} \mathbf{U}_g)^{\mathrm{T}} \right) : \boldsymbol{\nabla} \mathbf{U}_g \right] \tag{3.19}$$

is the so called production term of k, the constants are $\sigma_k = 1.0$, $\sigma_\varepsilon = 1.3$, $C_{\varepsilon,1} = 1.44$ and $C_{\varepsilon,2} = 1.92$, and the terms S_k and S_ε would be responsible to account for any other sources to the equations, as turbulence due to the wake of the particles for instance, although they are not utilized in the present thesis.

The k-ε model is attributed to Jones and Launder (1972), but the standard version of the model most utilized nowadays is written using the constants from Launder and Sharma (1974). Also the original correction for low Re numbers is rarely applied. More insightful discussions about the meaning of each of the terms and the reasonability behind the constants, as well as the derivation of the model itself, are presented in the references cited at the beginning of subsubsection 3.1.1.2.

A well-know characteristic of most turbulence closure models is that they yield unsatisfactory results in the near-wall region. Thus, the use of wall functions is necessary to match the *law-of-the-wall*. The most utilized wall function for the standard k-ε model is the so called standard wall function. In this model, algebraic expressions are utilized to calculate $\mathbf{U}_g$, k, ε, P_k, and μ_t, on the wall-adjacent cell to match the expected value for a turbulent boundary layer in the range $30 < y^+ < 200$.

Using the above methodology, the standard version of the k-ε model provides enough accuracy in a wide variety of engineering flows. However, it is known that it may come to wrong predictions for flows with complex phenomena in the near-wall region, such as: separation, recirculation, or in the advent of strong adverse pressure gradients in the boundary layer. This is mainly because the standard wall law is only valid for the $30 < y^+ < 200$ range, whereas the aforementioned phenomena can occur in the range of $y^+ < 5$. A more appropriate model is presented in the next subsubsubsection, which is utilized throughout the present thesis.

3.1.1.2.2 Two-layer k-ε model

As an alternative to overcome some deficiencies imposed by the use of the standard wall function, the *two-layer* version of the k-ε model, devised by Chen and Patel (1988), can be used. In this model, the flow is divided into two regions: a core flow region, and a near-wall region. In the core region the standard k-ε model is solved without modifications, but in the near-wall region k is solved by the same transport equation whereas ε and μ_t are solved by algebraic length scale models.

The two-layer k-ε model has also been shown to be better for particle velocity predictions in the near-wall region, as shown by Tian and Ahmadi (2007). These authors presented results of particle deposition velocity in the near-wall region and concluded that the two-layer k-ε model provides a better prediction than the standard k-ε model. It also provided a better prediction than the anisotropic Reynolds Stress Model (LAUNDER *et al.*, 1975) with the standard wall function.

Let the subscript *std* define the variables calculated by the standard model and $2l$ the ones calculated by the two-layer model. Then, the two-layer eddy viscosity is calculated as

$$\mu_{t,2l} = C_\mu \rho \sqrt{k} l_\mu \, , \tag{3.20}$$

and ε_{2l} as

$$\varepsilon_{2l} = \frac{k^{3/2}}{l_\varepsilon} \, . \tag{3.21}$$

The length scales l_μ and l_ε contain the necessary damping effects for the near-wall region and are calculated as

$$l_\mu = C_l y \left(1 - e^{-Re_y/A_\mu}\right) \tag{3.22}$$

and

$$l_\varepsilon = C_l y \left(1 - e^{-Re_y/A_\varepsilon}\right) \, , \tag{3.23}$$

where $C_l = \kappa C_\mu^{-3/4}$, $\kappa = 0.4187$ is the von Kármán constant, $A_\mu = 70$, and $A_\varepsilon = 2C_l$.

The two regions are characterized comparing the local Re_y, the turbulence Reynolds number based on the minimum distance to the wall y_w, with a critical reference value, namely $\mathrm{Re}_y^* = 200$. If $\mathrm{Re}_y \geqslant \mathrm{Re}_y^*$ the flow belongs to the core region, otherwise it belongs to the near-wall region. Re_y is defined as:

$$\mathrm{Re}_y = \frac{\rho_g y_w \sqrt{k}}{\mu} \, . \tag{3.24}$$

A good way to transition between the two regions is using a blending function λ, defined as

$$\lambda = \frac{1}{2}\left[1 + \tanh\left(\frac{Re_y - Re_y^*}{A_{2l}}\right)\right] \, , \tag{3.25}$$

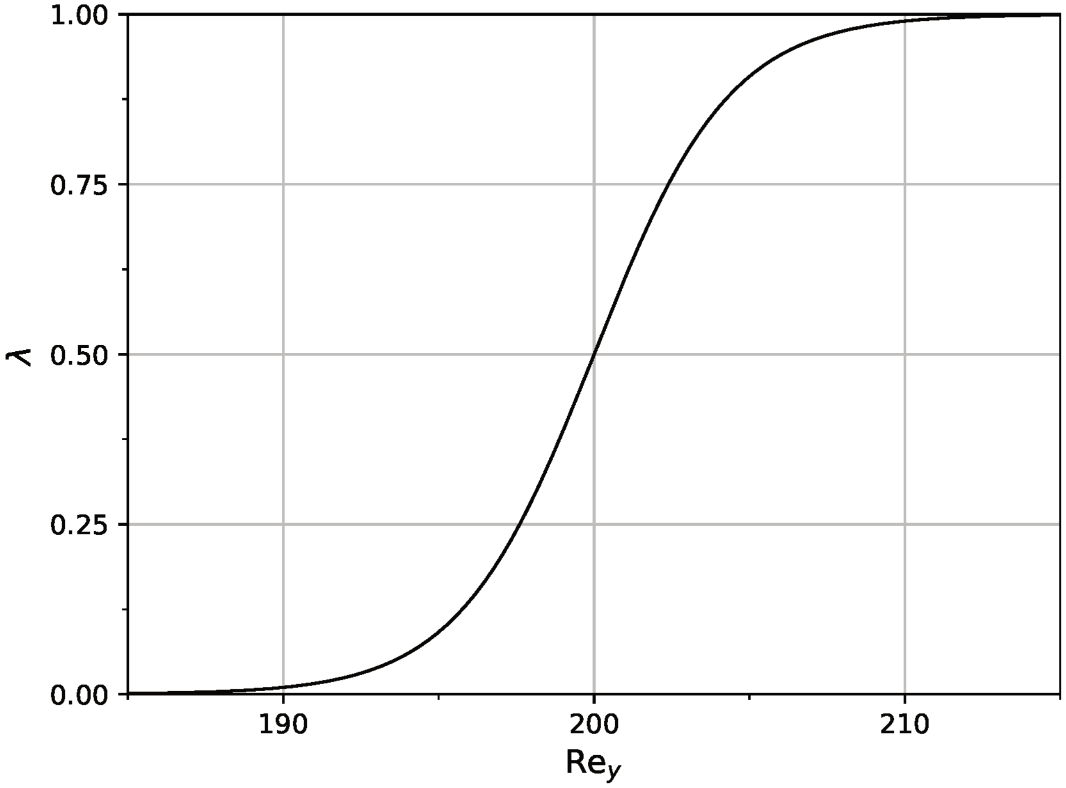

Figure 3 – Blending function λ to smooth the two-layer k-ε model transition.

where

$$A_{2l} = \frac{\mathrm{Re}_y^*}{10 \ln\left(\frac{1+0.98}{1-0.98}\right)} \approx 4.35\,. \tag{3.26}$$

Figure 3 shows the blending function λ. One can note that the transition is confined to a narrow region from $Re_y \approx 190$ to $Re_y \approx 210$ and that it presents a compact support. Before and after these respective values, the function reaches 0 and 1 and remains as it.

Finally,

$$\varepsilon = \lambda\varepsilon_{std} + (1 - \lambda)\varepsilon_{2l}\,, \tag{3.27}$$

and

$$\mu_t = \lambda\mu_{t,std} + (1 - \lambda)\mu_{t,2l}\,. \tag{3.28}$$

3.1.2 Particle phase formulation

For the particle phase formulation, a Lagrangian point-source approach is used. That is, the particles are solved as individual entities, where the forces acting on them are superimposed to each other. The important quantities to fully describe the state of a particle are its position $\mathbf{x}_p$, linear velocity $\mathbf{u}_p$, and angular velocity $\boldsymbol{\omega}_p$, which can be solved by the following ordinary differential equations (ODE):

$$\frac{\mathrm{d}\mathbf{x}_p}{\mathrm{d}t} = \mathbf{u}_p\,, \tag{3.29}$$

$$m_p \frac{\mathrm{d}\mathbf{u}_p}{\mathrm{d}t} = \sum \mathbf{F_p}\,, \tag{3.30}$$

and

$$I_p \frac{\mathrm{d}\boldsymbol{\omega}_p}{\mathrm{d}t} = \sum \mathbf{T_p}\,. \tag{3.31}$$

In Equation 3.30, m_p is the particle mass, and $\mathbf{F_p}$ are any forces acting on the particle. In Equation 3.31, I_p is the particle moment of inertia, and $\mathbf{T_p}$ is the torque applied on a particle. The moment of inertia to be considered is that of a solid sphere:

$$I_p = \frac{m_p}{10} d_p^2\,. \tag{3.32}$$

In the present thesis, the dilute flows are modeled using drag ($\mathbf{F_D}$), shear-induced lift ($\mathbf{F_{LS}}$), rotation-induced lift ($\mathbf{F_{LR}}$), weight

$$\mathbf{F_W} = \rho_p V_p \mathbf{g}\,, \tag{3.33}$$

and buoyancy

$$\mathbf{F_B} = -\rho_g V_p \mathbf{g} \tag{3.34}$$

as forces for the linear velocity equation, where V_p is the particle volume. In the angular velocity equation, the only source of torque is the fluid exerted torque $\mathbf{T_f}$. Note that particle-wall and particle-particle collisions could also be sources of change in both the linear and angular velocity equations for the particles, however this change will be taken into account directly into the respective collision models. After adopting these sources, Equations 3.30 and 3.29 may be rewritten as:

$$m_p \frac{\mathrm{d}\mathbf{u}_p}{\mathrm{d}t} = \mathbf{F_D} + \mathbf{F_{LS}} + \mathbf{F_{LR}} + m_p \mathbf{g} \left(1 - \frac{\rho_g}{\rho_p}\right), \tag{3.35}$$

and

$$I_p \frac{\mathrm{d}\boldsymbol{\omega}_p}{\mathrm{d}t} = \mathbf{T_f}\,. \tag{3.36}$$

The linear forces and the fluid exerted torque are briefly discussed in the next subsubsections. More details about the forces derivation, some historical perspective, and reasoning are available in reference multiphase flow texts, such as Sommerfeld (2000), Loth (2010), Crowe *et al.* (2011), Alletto (2014), Loth (2016) and Sommerfeld and Laín (2016).

3.1.2.1 Drag force

In turbulent particle-laden flows the drag force is always the most important surface force in the main flow direction, as it adds both the pressure field and viscous stresses contributions (form and friction drag). Usually, it outvalues virtual mass and Basset forces by several orders of magnitude. The general expression for the drag force is:

$$\mathbf{F_D} = \frac{1}{2} \rho_g A_p C_D \|\mathbf{U}_g - \mathbf{u}_p\| (\mathbf{U}_g - \mathbf{u}_p)\,, \tag{3.37}$$

where A_p is the projected cross sectional area of the particle in the relative velocity direction and C_D is the drag coefficient. A commonly used expression for C_D is that of Schiller and Naumann (1935), which appends a correction to the Stokes drag law:

$$C_D = \begin{cases} \dfrac{24}{\mathrm{Re}_p}\left(1 + 0.15\mathrm{Re}_p^{0.687}\right), & \text{if } \mathrm{Re}_p < 1000; \\ 0.44, & \text{otherwise}; \end{cases} \tag{3.38}$$

where the expression for the particle Reynolds number is

$$\mathrm{Re}_p = \frac{\rho_g \|\mathbf{U}_g - \mathbf{u}_p\| d_p}{\mu}\,. \tag{3.39}$$

There are many correlations other than the aforementioned, such as Morsi and Alexander (1972), Haider and Levenspiel (1989) and Coelho and Massarani (1996). However, all of them are very similar for the range of particle Reynolds numbers achieved in the present thesis simulations. In Figure 4, these drag correlations are compared for a range of common particle Reynolds numbers. For instance, consider the limiting case where large particles with a diameter of 500 µm initially at rest are accelerated by air at 30 m/s. In this case, the maximum particle Reynolds number is around 1000, which would only occur in acceleration regions. Now let the typical case be that with a relative velocity of around 2 m/s with the a particle diameter of 100 µm, than the typical particle Reynolds number is around 15. At this range of Re_p, Figure 4 confirms that all correlations give similar results.

Equation 3.37 is often rewritten for spherical particles incorporating the particle mass and using the appropriate geometric expression for the projected area ($A_p = \pi d_p^2/4$):

$$\mathbf{F_D} = \frac{3}{4}\frac{\rho_g m_p}{\rho_p d_p} C_D \|\mathbf{U}_g - \mathbf{u}_p\| (\mathbf{U}_g - \mathbf{u}_p)\,. \tag{3.40}$$

3.1.2.2 Shear lift force

The shear-induced lift force arises when there is a velocity gradient over a particle that is acting on a transversal direction in relation to the flow. As the higher transversal velocity gradients are, usually, transversal to the main flow direction (for instance in the near-wall region), this force can become very important even though its magnitude is only a fraction of the drag. This force is also called *Saffman force*, named after Saffman (1965, 1968), who devised its analytical expression for a flow around a sphere at a very low particle Reynolds number and shear Reynolds number, namely

$$\mathrm{Re}_S = \frac{\rho_g \|\boldsymbol{\omega}_g\| d_p^2}{\mu}\,, \tag{3.41}$$

and under the restriction $\mathrm{Re}_S << \sqrt{\mathrm{Re}_p}$. Decades later, McLaughlin (1991) relaxed the latter restriction by introducing a correction that can be calculated by analytical expressions or taken from tabulated values, depending on the range of Re_p and Re_S. However, this

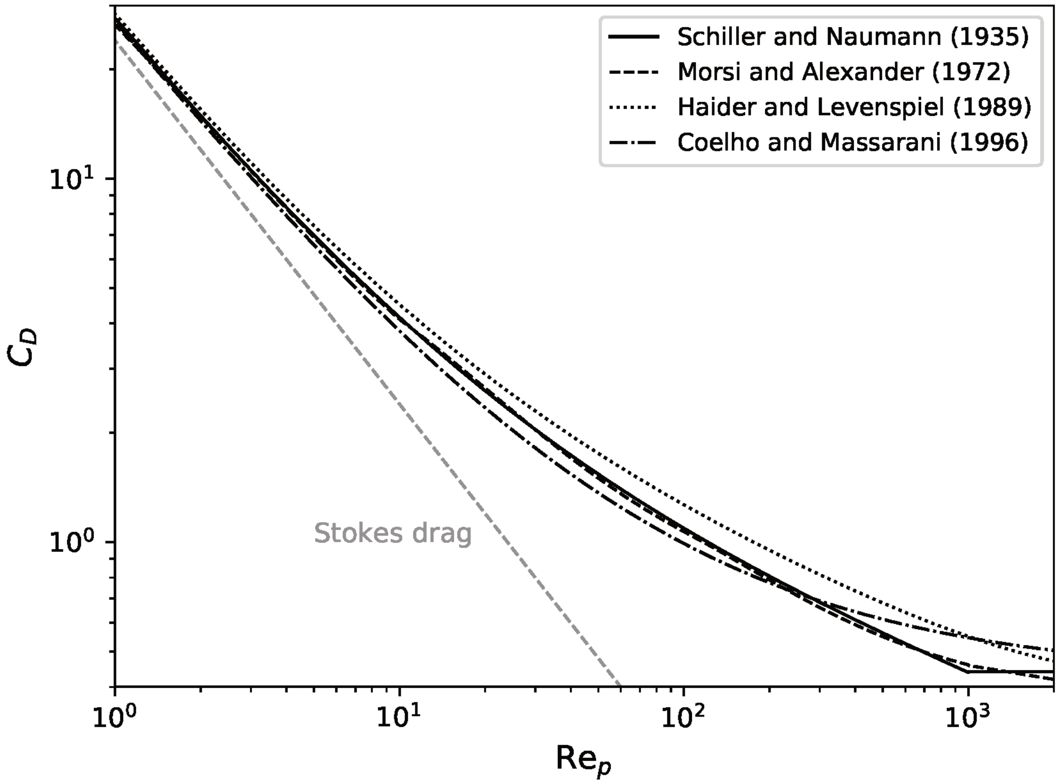

Figure 4 – Comparison of particle drag models for dilute flows.

correction is still very limited in the light of turbulent flows. After that, Mei (1992) used data from DNS simulations of Dandy and Dwyer (1990) to propose a correlation for a shear lift coefficient C_{LS}, which also fits well both Saffman (1965) and McLaughlin (1991) results, and has a higher range of validity: $0.1 < \mathrm{Re}_p < 100$ and $0.01 < \mathrm{Re}_S/\mathrm{Re}_p < 0.8$.

The general shear lift force expression is

$$\mathbf{F_{LS}} = 1.615 d_p^2 \sqrt{\mu \rho_g} C_{LS} \frac{(\mathbf{U}_g - \mathbf{u}_p) \times \boldsymbol{\omega}_g}{\sqrt{\|\boldsymbol{\omega}_g\|}} \,, \tag{3.42}$$

where the C_{LS} given by Mei (1992) is

$$C_{LS} = \begin{cases} \left(1 - 0.3314\sqrt{\beta}\right) \exp\left(-\frac{\mathrm{Re}_p}{10}\right) + 0.3314\sqrt{\beta}, & \text{if } \mathrm{Re}_p < 40; \\ 0.0524\sqrt{\beta \mathrm{Re}_p}, & \text{otherwise;} \end{cases} \tag{3.43}$$

$\boldsymbol{\omega}_g$ is the fluid vorticity ($\boldsymbol{\nabla} \times \mathbf{U}_g$), and $\beta = 0.5\mathrm{Re}_S/\mathrm{Re}_p$.

Sometimes the shear lift force expression can be presented in a slightly different way, to be more alike the generic expression for the drag force:

$$\mathbf{F_{LS}} = \frac{1}{2} \rho_g \frac{\pi}{4} d_p^3 C_{LS}^* (\mathbf{U}_g - \mathbf{u}_p) \times \boldsymbol{\omega}_g \,, \tag{3.44}$$

where the new shear lift force coefficient C_{LS}^* relates to the previous one as

$$C_{LS}^* = \frac{4.1126}{\sqrt{\mathrm{Re}_S}} C_{LS} \,. \tag{3.45}$$

A good exercise to understand the transversal aspect of the shear lift force, is to expand the term $(\mathbf{U}_g - \mathbf{u}_p) \times \boldsymbol{\omega}_g$ of Equation 3.42. In a Cartesian coordinate system, the vector is:

$$(\mathbf{U}_g - \mathbf{u}_p) \times \boldsymbol{\omega}_g = \begin{bmatrix} (V_g - v_p)\left(\frac{\partial V_g}{\partial x} - \frac{\partial U_g}{\partial y}\right) + (W_g - w_p)\left(\frac{\partial W_g}{\partial x} - \frac{\partial U_g}{\partial z}\right) \\ (U_g - u_p)\left(\frac{\partial U_g}{\partial y} - \frac{\partial V_g}{\partial x}\right) + (W_g - w_p)\left(\frac{\partial W_g}{\partial y} - \frac{\partial V_g}{\partial z}\right) \\ (U_g - u_p)\left(\frac{\partial U_g}{\partial z} - \frac{\partial W_g}{\partial x}\right) + (V_g - v_p)\left(\frac{\partial V_g}{\partial z} - \frac{\partial W_g}{\partial y}\right) \end{bmatrix} \tag{3.46}$$

where the velocity vectors were expanded in the three-dimensional cartesian system as $\mathbf{U}_g = [U_g, V_g, W_g]$ and $\mathbf{u}_p = [u_p, v_p, w_p]$.

3.1.2.3 Rotation lift force

Another source of lift force arises when the particle has a relative rotation in relation to the fluid surrounding it. The relative rotation can induce a difference of pressure and/or shear stress between two hemispheres and result in a force transversal to the flow, similarly to the shear-induced lift. The rotation-induced lift is also know as *Magnus force* after his work in rotating cylinders. The general expression for this force follows the analytical derivation of Rubinow and Keller (1961) for flows at $\mathrm{Re}_p << 1$ and $\mathrm{Re}_R/\mathrm{Re}_p << 1$, but appending a rotation lift coefficient C_{LR} to handle non-idealized cases, and considering the relative particle-fluid rotation $\boldsymbol{\Omega}_{\boldsymbol{rel}}$:

$$\mathbf{F_{LR}} = \frac{1}{2}\rho_g \frac{\pi}{4} d_p^3 C_{LR} [\boldsymbol{\Omega}_{\boldsymbol{rel}} \times (\mathbf{U}_g - \mathbf{u}_p)]\,, \tag{3.47}$$

where $\boldsymbol{\Omega}_{\boldsymbol{rel}} = \frac{1}{2}\boldsymbol{\omega}_g - \boldsymbol{\omega}_p$.

Many correlations for C_{LR} are available. One of the most utilized is that of Lun and Liu (1997), which uses Rubinow and Keller (1961) value for $\mathrm{Re}_p < 1$, and a curve fit for outside this range. The fit was based on Oesterlé *et al.* (1991) for $10 < \mathrm{Re}_p < 60$ and $2 < \mathrm{Re}_R/\mathrm{Re}_p < 12$, and on Tsuji *et al.* (1985) for $550 < \mathrm{Re}_p < 1600$ and $\mathrm{Re}_R/\mathrm{Re}_p < 1.4$. The intermediate range is assumed to be adjusted by the resulting curve. The expression is as follows:

$$C_{LR} = \begin{cases} 1, & \text{if } \mathrm{Re}_p < 1; \\ 0.178 + 0.822\mathrm{Re}_p^{-0.522}, & \text{otherwise.} \end{cases} \tag{3.48}$$

Another one was proposed by Oesterlé and Dinh (1998), for the $10 < \mathrm{Re}_p < 140$ and $2 < \mathrm{Re}_R/\mathrm{Re}_p < 12$ range:

$$C_{LR} = 0.45/\left(\frac{\mathrm{Re}_R}{\mathrm{Re}_p}\right) + \left[1 - 0.45/\left(\frac{\mathrm{Re}_R}{\mathrm{Re}_p}\right)\right] \exp\left[-0.05684\left(\frac{\mathrm{Re}_R}{\mathrm{Re}_p}\right)^{0.4} \mathrm{Re}_p^{0.7}\right], \tag{3.49}$$

where the particle rotation Reynolds number is

$$\mathrm{Re}_R = \frac{\rho_g \|\boldsymbol{\Omega}_{\boldsymbol{rel}}\| d_p^2}{\mu}\,. \tag{3.50}$$

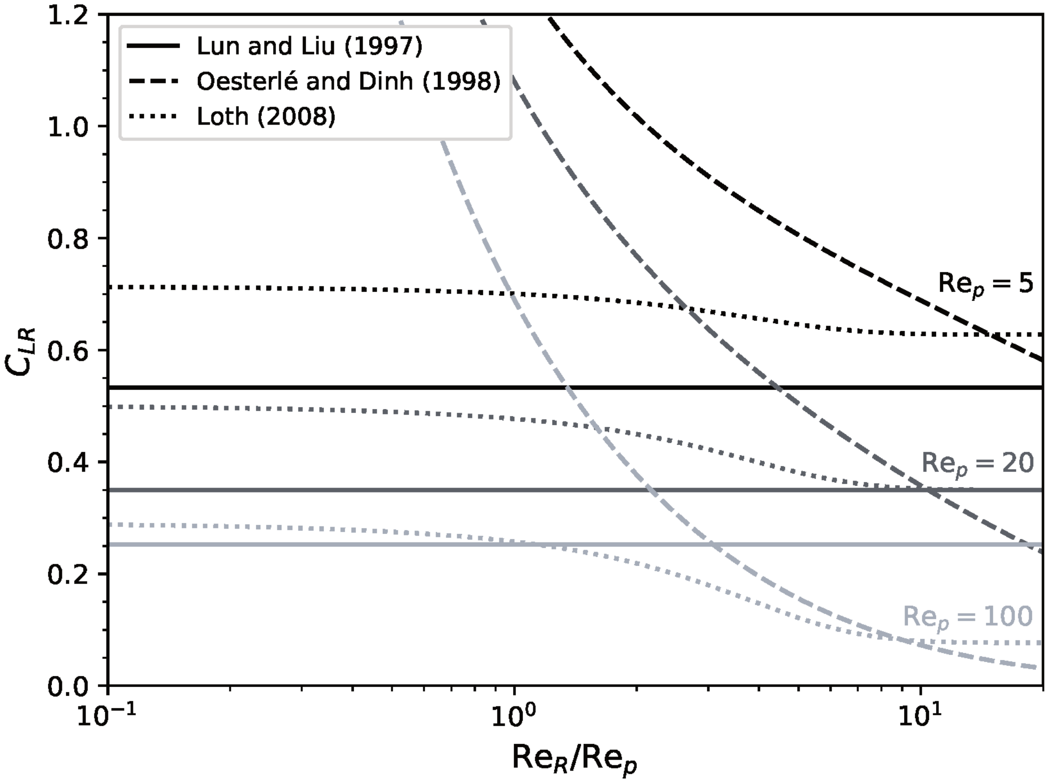

Figure 5 – Comparison of particle rotation lift models.

More recently, a correlation suitable for a wider range of applicability was proposed by Loth (2008) using multiple data sources, valid for $\mathrm{Re}_p < 2000$ and $\mathrm{Re}_R/\mathrm{Re}_p < 20$:

$$C_{LR} = 1 - \left\{0.675 + 0.15\left(1 + \tanh\left[0.28\left(\frac{\mathrm{Re}_R}{\mathrm{Re}_p} - 2\right)\right]\right)\right\}\tanh\left(0.18\sqrt{\mathrm{Re}_p}\right). \qquad (3.51)$$

All three correlations are compared in Figure 5, where typical values of Re_p are plotted for the maximum allowed range of $\mathrm{Re}_R/\mathrm{Re}_p$. To allow easier conclusions let us take Loth (2008) correlation as the reference, since in his original work the author shows a good agreement for his correlation with many data sources in a similar figure. This shows that, although there is some agreement among the correlations in different regions, in overall Loth (2008) correlation should be preferred for a wider range of applicability with a higher confidence.

The UNSCYFL3D code was being utilized with the Lun and Liu (1997) correlation for C_{LR} in previous works. However, for the present thesis and derived works, Loth (2008) correlation was used.

3.1.2.4 Fluid exerted torque

The fluid vorticity is also responsible to add torque to the particle. The expression under idealized conditions is also given by Rubinow and Keller (1961), and the general expression adding the fluid exerted torque coefficient for correction is

$$\mathbf{T_f} = \frac{1}{2}\rho_g\left(\frac{d_p}{2}\right)^5 C_R \|\boldsymbol{\Omega_{rel}}\|\boldsymbol{\Omega_{rel}}\,, \tag{3.52}$$

where C_R is taken from Dennis *et al.* (1980):

$$C_R = \begin{cases} \dfrac{64\pi}{\mathrm{Re}_R}, & \text{if } \mathrm{Re}_R < 32; \\ \dfrac{12.9}{\sqrt{\mathrm{Re}_R}} + \dfrac{128.4}{\mathrm{Re}_R}, & \text{otherwise.} \end{cases} \tag{3.53}$$

3.1.3 Euler-Lagrange coupling

As the phases are solved in different frameworks, the coupling between the phases is given by the interaction forces between the fluid and the particle. As previously mentioned, in the fluid phase this is taken into account by the last term of Equation 3.5 ($\mathbf{F_{gp}}$) which is calculated by the summation of the fluid exerted forces in Equation 3.35 over all particles considered in the control volume V:

$$\mathbf{F_{gp}} = \sum_{i=1}^{n_p} \frac{1}{V}\left(\mathbf{F_{D,i}} + \mathbf{F_{LS,i}} + \mathbf{F_{LR,i}}\right), \tag{3.54}$$

where the summation index i indicates the summation from the first up to the total number of particles n_p. These forces, in turn, are calculated through correlations that depend on the fluid characteristics at the particle position, as already discussed in subsection 3.1.2.

Note that some in simulations, one may choose to not take into account the effect of the particles in the fluid phase, characterizing the so called one-way coupling. This approach is usually only suitable for very low mass loadings. The more common approach where the effects into the fluid phase are taken into account, as presented in the equation above, is the two-way coupling. Another level of coupling is the four-way coupling, that is named when the two-way coupling is used between fluid and particle, and also the interaction between the particles themselves (particle-particle collisions) are taken into account.

3.2 Dense flows

To simulate flows at a higher particle mass loading, i.e. in the conditions outside of the ones stated in section 3.1, one needs to account for the physical space that the particles take up in the total volume. This essentially means that the some sort of volume fraction variable should appear in the gas phase equations, as will be presented in subsection 3.2.1. On the other hand, the particle phase modeling should also reflect the difference in force that the fluid will apply, given the population effect, which is subject to subsection 3.2.2.

3.2.1 Gas phase formulation

As already discussed throughout the present thesis, in order to account for the effect of the particles in the carrier phase, one has to either resolve the fluid-particle equations on the scale of the particle surface or use a gas phase formulation that accounts for the particle presence. For the present thesis, the volume filtered equations derived by Anderson and Jackson (1967) were chosen to solve the gas phase in a dense particulate flow. Their formulation was chosen as it presents mathematical rigor throughout the derivation, and was also successfully used by other authors. See, for instance, Capecelatro and Desjardins (2013) that have revisited the original formulation in their article and successfully applied this modeling in their following works.

In this formulation, the point-wise fluid variables are replaced by local mean variables, which are obtained by filtering them over regions larger than the particles but still smaller then the scale of the macroscopic flow. Thus, the point-wise variables will become variables that are volume averaged, and the resulting equations will have incorporated the effect of the space occupied by the particles in the domain. One will note that this filter shares some similarities with the filter applied to the dilute flows in subsubsection 3.1.1.2, in order to bring the fluid flow equation into a realistic framework of geometry size and Reynolds number for engineering simulations. A similar closure will be utilized to handle the resulting turbulent tensor.

An interesting alternative mathematical derivation that can be utilized to reach the very same formulation of Anderson and Jackson (1967), is introduced in Crowe *et al.* (2011). Their derivation does not use a filter function, but rather relies on averaging volumes as defined in Slattery (1972). Crowe *et al.* (2011) derivation is not revisited in the present thesis, but will serve as reference to introduce the volume filtered two-layer k-ε model.

3.2.1.1 Volume filtered equations

Firstly, let $g(r)$ be a filtering kernel defined for positive values of r, the distance from a point in the 3D space, which meets the following properties: $g(r) > 0$ for all r; $g(r)$ monotonically decreases for increasing r; $g(r)$ is a continuous function; $g(r)$ is normalized such that its integration over the entire physical space V_∞ is

$$\int_{V_\infty} g(r)\,\mathrm{d}V = 1\,, \tag{3.55}$$

where the physical space can be divided into gas occupied points V_g and particle occupied points V_p, or

$$V_\infty = V_g(t) + V_p(t)\,. \tag{3.56}$$

This filter allows the definition of the local gas volume fraction (or void fraction) α_g as a function of any point $\mathbf{x}$ in the entire physical space and time t:

$$\alpha_g(\mathbf{x}, t) = \int_{V_g(t)} g(\|\mathbf{x} - \mathbf{y}\|)\,\mathrm{d}\mathbf{y}\ , \tag{3.57}$$

where the integration is taken over all the points occupied by the gas phase $\mathbf{y}$, as indicated by $V_g(t)$. On the other hand, using the restriction

$$\alpha_g + \alpha_p = 1 \tag{3.58}$$

the particle volume fraction α_p can be defined complementary to α_g by integrating over the space occupied by the particle phase, giving

$$\alpha_p(\mathbf{x}, t) = 1 - \alpha_g(\mathbf{x}, t) = \int_{V_p(t)} g(\|\mathbf{x} - \mathbf{y}\|)\,\mathrm{d}\mathbf{y}\ . \tag{3.59}$$

This equation can be further simplified assuming that $g(r)$ has a small variation within a single particle (CAPECELATRO; DESJARDINS, 2013):

$$\alpha_p(\mathbf{x}, t) = \sum_{i=1}^{n_p} g(\|\mathbf{x} - \mathbf{x}_i\|) V_{p,i}\,, \tag{3.60}$$

where the summation is taken over the index i up to the total number of particles n_p.

Now, let $\mathbf{a}(\mathbf{x}, t)$ be any fluid point property of any tensorial order. It is then possible to write

$$\mathbf{a}(\mathbf{x}, t) = \overline{\mathbf{a}}(\mathbf{x}, t) + \mathbf{a}'(\mathbf{x}, t)\,, \tag{3.61}$$

where its filtered value $\overline{\mathbf{a}}(\mathbf{x}, t)$ is computed by taking the convolution product with the filtering kernel g, such that

$$\alpha_g \overline{\mathbf{a}}(\mathbf{x}, t) = \int_{V_g(t)} \mathbf{a}(\mathbf{y}, t) g(\|\mathbf{x} - \mathbf{y}\|)\,\mathrm{d}\mathbf{y}\ , \tag{3.62}$$

and $\mathbf{a}'(\mathbf{x}, t)$ is its residual field. Note that this is a similar decomposition as the one carried out in subsubsection 3.1.1.2, and the filter applied to it will have properties comparable to those defined in Equation 3.7.

At this point, Anderson and Jackson (1967) point out that the filter size must be larger than the particles but still smaller then the scale of the macroscopic flow. However, Capecelatro and Desjardins (2013) also note that a filter size with the order of some particle diameters is enough to meet this criterion. A consequence of this filter size definition, is that the spatial variation of local filtered variables is slow if compared with the spatial variation of $g(r)$, such that it is possible to write

$$\int_{V_f(t)} \overline{\mathbf{a}}(\mathbf{y}, t) g(\|\mathbf{x} - \mathbf{y}\|)\,\mathrm{d}\mathbf{y} \approx \overline{\mathbf{a}}(\mathbf{x}, t) \int_{V_f(t)} g(\|\mathbf{x} - \mathbf{y}\|)\,\mathrm{d}\mathbf{y} = \alpha_g(\mathbf{x}, t)\overline{\mathbf{a}}(\mathbf{x}, t)\,, \tag{3.63}$$

using Equation 3.57.

Now, for the filtering of the temporal and spatial derivatives Anderson and Jackson (1967) are able to demonstrate the following relations:

$$\int_{V_g(t)} \frac{\partial \mathbf{a}(\mathbf{y},t)}{\partial t} g(\|\mathbf{x}-\mathbf{y}\|)\,\mathrm{d}\mathbf{y} = \frac{\partial}{\partial t}\Big(\alpha_g(\mathbf{x},t)\overline{\mathbf{a}}(\mathbf{x},t)\Big) - \sum_{i=1}^{n_p} \int_{S_{p,i}} \mathbf{n}_i(\mathbf{y},t)\cdot\mathbf{u}_i(\mathbf{y},t)\mathbf{a}(\mathbf{y},t) g(\|\mathbf{x}-\mathbf{y}\|)\,\mathrm{d}\mathbf{y}\ , \quad (3.64)$$

and

$$\int_{V_g(t)} \boldsymbol{\nabla}\cdot\mathbf{a}(\mathbf{y},t) g(\|\mathbf{x}-\mathbf{y}\|)\,\mathrm{d}\mathbf{y} = \boldsymbol{\nabla}\cdot\Big(\alpha_g(\mathbf{x},t)\overline{\mathbf{a}}(\mathbf{x},t)\Big) - \sum_{i=1}^{n_p} \int_{S_{p,i}} \mathbf{n}_i(\mathbf{y},t)\cdot\mathbf{a}(\mathbf{y},t) g(\|\mathbf{x}-\mathbf{y}\|)\,\mathrm{d}\mathbf{y}\ , \quad (3.65)$$

where the index $S_{p,i}$ indicates that the integral is carried out over all the points in the surface of each particle under the summation, $\mathbf{n}_i$ is the particle surface unit vector, and $\mathbf{u}_i$ is the velocity at the surface of particle i, which is essentially the particle velocity. The main assumption that lead to the second term in the RHS of the equations above, is that the filter and differential operators are not commutative, mainly because of the particle surface contributions.

To reach the volume filtered equations, we can start from the point-wise ones, multiply them by the filtering kernel $g(r)$, and integrate them over all fluid occupied points. Let us start by the continuity equation (Equation 3.1):

$$\frac{\partial \rho_g}{\partial t} + \boldsymbol{\nabla}\cdot(\rho_g\mathbf{u}_g) = 0\,.$$

Applying the relations given in Equation 3.64 and Equation 3.65, one is able to recover

$$\frac{\partial}{\partial t}(\alpha_g\rho_g) + \boldsymbol{\nabla}\cdot(\alpha_g\rho_g\overline{\mathbf{u}_g}) = \sum_{i=1}^{n_p} \int_{S_{p,i}} \rho_g \mathbf{n}_i(\mathbf{y},t)\cdot\Big(\mathbf{u}_g(\mathbf{y},t)-\mathbf{u}_i(\mathbf{y},t)\Big) g(\|\mathbf{x}-\mathbf{y}\|)\,\mathrm{d}\mathbf{y}\ , \quad (3.66)$$

which can be reduced to

$$\frac{\partial \alpha_g}{\partial t} + \boldsymbol{\nabla}\cdot(\alpha_g\overline{\mathbf{u}_g}) = 0\,, \quad (3.67)$$

since ρ_g is constant and the velocity of particle and fluid are equal at the particle surface. An important note, is that one could start from the simplified continuity equation (Equation 3.4) and would still arrive at the equation above.

The same procedure is carried out with the linear momentum equation (Equation 3.2):

$$\frac{\partial}{\partial t}(\rho_g\mathbf{u}_g) + \boldsymbol{\nabla}\cdot(\rho_g\mathbf{u}_g\mathbf{u}_g) = \boldsymbol{\nabla}\cdot\boldsymbol{\tau}_g + \rho_g\mathbf{g}\,,$$

however note that the gas-particle interaction term has been omitted since it should appear as a result of the volume filtering procedure. The filter applied to the first and last term of this equation (temporal derivative and gravity related) is straightforward, but the remaining ones (advective term and stress tensor divergent) need special attention.

The advective term filtering shall be done in parts because of the dyadic product. As it was shown previously in subsubsection 3.1.1.2, here this term will also give rise to a turbulence tensor related to the velocity fluctuations. This turbulence tensor will be closed using a proper turbulence closure model later in the next subsubsection. Let the filter of this term be

$$\begin{aligned}\int_{V_g(t)} \boldsymbol{\nabla}\cdot\Big(\rho_g\mathbf{u}_g(\mathbf{y},t)\mathbf{u}_g(\mathbf{y},t)\Big)g(\|\mathbf{x}-\mathbf{y}\|)\,\mathrm{d}\mathbf{y} = &\\ \boldsymbol{\nabla}\cdot\int_{V_g(t)}\Big(\rho_g\mathbf{u}_g(\mathbf{y},t)\mathbf{u}_g(\mathbf{y},t)\Big)g(\|\mathbf{x}-\mathbf{y}\|)\,\mathrm{d}\mathbf{y}&\\ -\sum_{i=1}^{n_p}\int_{S_{p,i}}\mathbf{n}_i(\mathbf{y},t)\cdot\Big(\rho_g\mathbf{u}_g(\mathbf{y},t)\mathbf{u}_g(\mathbf{y},t)\Big)g(\|\mathbf{x}-\mathbf{y}\|)\,\mathrm{d}\mathbf{y}\ .& \qquad (3.68)\end{aligned}$$

Then, using Equation 3.61, the first RHS integral is decomposed into:

$$\begin{aligned}\int_{V_g(t)}\Big(\rho_g\mathbf{u}_g(\mathbf{y},t)\mathbf{u}_g(\mathbf{y},t)\Big)g(\|\mathbf{x}-\mathbf{y}\|)\,\mathrm{d}\mathbf{y} = \int_{V_g(t)}\Big(\rho_g\overline{\mathbf{u}_g}(\mathbf{y},t)\overline{\mathbf{u}_g}(\mathbf{y},t)\Big)g(\|\mathbf{x}-\mathbf{y}\|)\,\mathrm{d}\mathbf{y}&\\ +2\int_{V_g(t)}\Big(\rho_g\overline{\mathbf{u}_g}(\mathbf{y},t)\mathbf{u}'_g(\mathbf{y},t)\Big)g(\|\mathbf{x}-\mathbf{y}\|)\,\mathrm{d}\mathbf{y}&\\ +\int_{V_g(t)}\Big(\rho_g\mathbf{u}'_g(\mathbf{y},t)\mathbf{u}'_g(\mathbf{y},t)\Big)g(\|\mathbf{x}-\mathbf{y}\|)\,\mathrm{d}\mathbf{y}\ ,& \qquad (3.69)\end{aligned}$$

where

$$\int_{V_g(t)}\Big(\rho_g\overline{\mathbf{u}_g}(\mathbf{y},t)\overline{\mathbf{u}_g}(\mathbf{y},t)\Big)g(\|\mathbf{x}-\mathbf{y}\|)\,\mathrm{d}\mathbf{y} = \alpha_g\rho_g\overline{\mathbf{u}_g\mathbf{u}_g}\,, \qquad (3.70)$$

$$\int_{V_g(t)}\Big(\rho_g\overline{\mathbf{u}_g}(\mathbf{y},t)\mathbf{u}'_g(\mathbf{y},t)\Big)g(\|\mathbf{x}-\mathbf{y}\|)\,\mathrm{d}\mathbf{y} \approx 0\,, \qquad (3.71)$$

and

$$\int_{V_g(t)}\Big(\rho_g\mathbf{u}'_g(\mathbf{y},t)\mathbf{u}'_g(\mathbf{y},t)\Big)g(\|\mathbf{x}-\mathbf{y}\|)\,\mathrm{d}\mathbf{y} = \alpha_g\rho_g\overline{\mathbf{u}'_g\mathbf{u}'_g}\,. \qquad (3.72)$$

The filtering of the stress tensor divergent is also carried out in parts:

$$\begin{aligned}\int_{V_g(t)}\Big(\boldsymbol{\nabla}\cdot\boldsymbol{\tau}_g(\mathbf{y},t)\Big)g(\|\mathbf{x}-\mathbf{y}\|)\,\mathrm{d}\mathbf{y} = \boldsymbol{\nabla}\cdot\Big(\alpha_g\overline{\boldsymbol{\tau}_g}\Big)&\\ -\sum_{i=1}^{n_p}\int_{S_i}\mathbf{n}_i(\mathbf{y},t)\cdot\overline{\boldsymbol{\tau}_g}(\mathbf{y},t)g(\|\mathbf{x}-\mathbf{y}\|)\,\mathrm{d}\mathbf{y}&\\ -\sum_{i=1}^{n_p}\int_{S_i}\mathbf{n}_i(\mathbf{y},t)\cdot\boldsymbol{\tau}'_g(\mathbf{y},t)g(\|\mathbf{x}-\mathbf{y}\|)\,\mathrm{d}\mathbf{y}\ ,& \qquad (3.73)\end{aligned}$$

where

$$\sum_{i=1}^{n_p}\int_{S_i}\mathbf{n}_i(\mathbf{y},t)\cdot\overline{\boldsymbol{\tau}_g}(\mathbf{y},t)g(\|\mathbf{x}-\mathbf{y}\|)\,\mathrm{d}\mathbf{y} \approx \overline{\boldsymbol{\tau}_g}\cdot\boldsymbol{\nabla}\alpha_g\,, \qquad (3.74)$$

and

$$\sum_{i=1}^{n_p}\int_{S_i}\mathbf{n}\cdot\boldsymbol{\tau}'_g(\mathbf{y},t)g(\|\mathbf{x}-\mathbf{y}\|)\,\mathrm{d}\mathbf{y} = F_{gp} - \alpha_p\boldsymbol{\nabla}\cdot\overline{\boldsymbol{\tau}_g}\,. \qquad (3.75)$$

Replacing the last two equations into Equation 3.73, one is able to retrieve:

$$\int_{V_g(t)} \Big(\boldsymbol{\nabla} \cdot \boldsymbol{\tau}_g(\mathbf{y},t)\Big) g(\|\mathbf{x}-\mathbf{y}\|)\,\mathrm{d}\mathbf{y} = \boldsymbol{\nabla} \cdot \overline{\boldsymbol{\tau}_g} - \mathbf{F_{gp}}\,. \tag{3.76}$$

Note that in order to reach Equation 3.74, one needs to make use of Gauss' theorem and assume that both $\overline{\boldsymbol{\tau}_g}$ and $\boldsymbol{\nabla} \cdot \overline{\boldsymbol{\tau}_g}$ vary little in the distance covered by this integral, in comparison to $g(r)$ (CAPECELATRO; DESJARDINS, 2013). The equality in Equation 3.75 is a little harder to see, but a longer discussion about it is presented in subsection 3.2.3.

Finally, the volume filtered linear momentum balance for the gas phase becomes

$$\rho_g\left[\frac{\partial}{\partial t}(\alpha_g \mathbf{u}_g) + \boldsymbol{\nabla} \cdot (\alpha_g \overline{\mathbf{u}_g}\;\overline{\mathbf{u}_g})\right] = \boldsymbol{\nabla} \cdot \Big(\boldsymbol{\tau_g} - \boldsymbol{\alpha_g \rho_g}\overline{\mathbf{u}'_{\boldsymbol{g}}\mathbf{u}'_{\boldsymbol{g}}}\Big) + \alpha_g \rho_g \mathbf{g} + \mathbf{F_{gp}}\,. \tag{3.77}$$

The closure model for the stress tensor $\boldsymbol{\tau}_g$ is similar to that in Equation 3.3, but the molecular viscosity μ is replaced by a volume fraction dependent viscosity μ_α (ANDERSON; JACKSON, 1967; CAPECELATRO; DESJARDINS, 2013):

$$\boldsymbol{\tau}_g = -p\mathbf{I} + \mu_\alpha\Big[\boldsymbol{\nabla}\mathbf{u}_g + (\boldsymbol{\nabla}\mathbf{u}_g)^{\mathrm{T}}\Big] - \Big(\frac{2}{3}\mu_\alpha - \kappa\Big)(\boldsymbol{\nabla} \cdot \mathbf{u}_g)\mathbf{I}\,. \tag{3.78}$$

Note that some simplifications do not apply anymore, namely: μ_α is not constant, and varies with space and time; the divergent of the gas phase velocity is no longer zero, i.e., $\boldsymbol{\nabla} \cdot \overline{\mathbf{u}_g} \neq 0$. Nevertheless, Equation 3.78 can still be simplified by noting that the dilatational viscosity κ is zero for monoatomic gases at low density (such as the air).

In the present thesis, following Capecelatro and Desjardins (2013), the expression of Gibilaro *et al.* (2007) is utilized for the volume fraction dependent viscosity:

$$\mu_\alpha = \mu\alpha_g^{-2.8}\,. \tag{3.79}$$

3.2.1.2 Turbulence closure

In the mathematical formulation for dense flows, the turbulence tensor appears beforehand as a result of the filtering procedure that is carried out in order to obtain volume filtered equations that account for the particle volume fraction. This is different from the formulation for dilute flows, where a filter had to be applied in order to provide equations suitable for turbulent flows using turbulence closure models.

In the present thesis, the turbulence tensor is closed in a similar manner as Equation 3.11, but taking into account the same simplifications applied to Equation 3.78. Let the Boussinesq assumption be written as:

$$\alpha_g \rho_g \overline{\mathbf{u}'_g \mathbf{u}'_g} = -\alpha_g \mu_t\Big[\boldsymbol{\nabla}\overline{\mathbf{u}_g} + (\boldsymbol{\nabla}\overline{\mathbf{u}_g})^{\mathrm{T}} + \frac{2}{3}(\boldsymbol{\nabla} \cdot \mathbf{u}_g)\mathbf{I}\Big] + \frac{2}{3}\alpha_g \rho_g k\mathbf{I}\,. \tag{3.80}$$

Then, replacing Equation 3.78 and Equation 3.80 into Equation 3.77, and using the simplified notation for the filtered gas velocity as $\mathbf{U}_g$, one has:

$$\frac{\partial \alpha_g}{\partial t} + \boldsymbol{\nabla} \cdot (\alpha_{\mathbf{g}} \mathbf{U}_{\mathbf{g}}) = 0\,, \tag{3.81}$$

and

$$\rho_g \left[\frac{\partial}{\partial t}(\alpha_g \mathbf{U}_g) + \boldsymbol{\nabla} \cdot (\alpha_g \mathbf{U}_g \mathbf{U}_g) \right] = -\boldsymbol{\nabla} P + \boldsymbol{\nabla} \cdot \Big[\mu_{\mathrm{eff},\alpha} \Big(\boldsymbol{\nabla} \mathbf{U}_g + (\boldsymbol{\nabla} \mathbf{U}_g)^{\mathrm{T}} \Big) \Big] + \rho_g \mathbf{g} + \mathbf{F}_{\mathrm{gp}}\,, \tag{3.82}$$

where $P = p + 2/3 \alpha_g \rho_g k$, and

$$\mu_{\mathrm{eff},\alpha} = \mu_\alpha + \alpha_g \mu_t\,. \tag{3.83}$$

The closure model utilized here for μ_t is similar to the two-layer k-ε model applied for the closure of turbulence in the dilute formulation. The filtered equations for k and ε were not presented by Anderson and Jackson (1967), although they could be reached by applying the filter to the equations. Capecelatro and Desjardins (2013), for instance, showed this derivation for a generic scalar being transported, which could be assumed as k or ε . However, Crowe *et al.* (2011) present the mathematical formulation for volume filtered k and ε using their alternative derivation. These equations are presented here, but without showing the mathematical procedure. Let them be:

$$\rho_g \left[\frac{\partial}{\partial t}(\alpha_g k) + \boldsymbol{\nabla} \cdot (\alpha_g \mathbf{U}_g k) \right] = \boldsymbol{\nabla} \cdot \left[\alpha_g \Big(\mu + \frac{\mu_t}{\sigma_k} \Big) \boldsymbol{\nabla} k \right] + \alpha_g P_k - \alpha_g \rho_g \varepsilon + S_{k,\alpha_g} \tag{3.84}$$

and

$$\rho_g \left[\frac{\partial}{\partial t}(\alpha_g \varepsilon) + \boldsymbol{\nabla} \cdot (\alpha_g \mathbf{U}_g \varepsilon) \right] = \boldsymbol{\nabla} \cdot \left[\alpha_g \Big(\mu + \frac{\mu_t}{\sigma_\varepsilon} \Big) \boldsymbol{\nabla} \varepsilon \right] + C_{\varepsilon,1} \alpha_g \frac{\varepsilon}{k} P_k - C_{\varepsilon,2} \alpha_g \rho_g \frac{\varepsilon^2}{k} + S_{\varepsilon,\alpha_g}\,, \tag{3.85}$$

where S_{k,α_g} and S_{ε,α_g} would be sources to the equations. Crowe *et al.* (2011) present a good review of particle-induced turbulence modulation models, however such phenomena is neglected in the present thesis. The other equations introduced in subsubsubsection 3.1.1.2.2 are utilized without modification.

3.2.2 Particle phase formulation

The approach utilized to solve the particle phase motion in the dense formulation is the same as in the dilute formulation. However, the surface forces are taken into account in a different manner, following a more complete formulation. Knowing that the fluid exerted force upon a particle is actually due to the fluid normal and tangential stresses over the particle surface, one can write:

$$\begin{aligned}\mathbf{f} &= \int_{S_p} \boldsymbol{\tau}_g \cdot \mathbf{n}\,\mathrm{d}\mathbf{y} \\ &= \int_{S_p} (\overline{\boldsymbol{\tau}_g} + \boldsymbol{\tau}_g') \cdot \mathbf{n}\,\mathrm{d}\mathbf{y} \\ &= \int_{S_p} \boldsymbol{\nabla} \cdot \overline{\boldsymbol{\tau}_g}\,\mathrm{d}\mathbf{y} + \int_{S_p} \boldsymbol{\tau}_g' \cdot \mathbf{n}\,\mathrm{d}\mathbf{y} \\ &= V_p \boldsymbol{\nabla} \cdot \overline{\boldsymbol{\tau}_g} + \int_{S_p} \boldsymbol{\tau}_g' \cdot \mathbf{n}\,\mathrm{d}\mathbf{y}\ ,\end{aligned} \tag{3.86}$$

using the relations presented in subsubsection 3.2.1.1.

In Equation 3.86, one can note that there are two separated contributions: due to the resolved and unresolved stresses, respectively. The resolved stresses term is the part of the stress tensor that has been already mathematically solved in the gas phase equations. The unresolved ones were not, because they depend on the fluctuation part of the tensor. This term is what makes the traditional forces correlations to appear in the particle equations, such as drag, lift, and others.

Note that although this form of particle forces is not very common, it reduces to the traditional form if some simplifications are applied. Take, for instance, the $\boldsymbol{\tau}_g$ equation for a dilute flow such as in Equation 3.3:

$$\boldsymbol{\tau}_g = -p\mathbf{I} + \mu\Big[\boldsymbol{\nabla}\mathbf{u}_g + (\boldsymbol{\nabla}\mathbf{u}_g)^{\mathrm{T}}\Big] - \Big(\frac{2}{3}\mu - \kappa\Big)(\boldsymbol{\nabla}\cdot\mathbf{u}_g)\mathbf{I}\,.$$

The divergent applied to the first part is actually the pressure gradient force, which is utilized by some authors to simulate gas-particle flows. And if the flow contribution is removed from the pressure, remaining only the static contribution, that would be the same as the buoyancy force. Now for the tangential contribution, this is a term that is also often neglected because is usually small over the particle. However, these simplifications are not applied in the present thesis until their influences are further studied and understood.

Concerning the forces due to the unresolved stresses, it is common that in CFB riser simulations[1], the only traditional fluid exerted force taken into account is the drag. All transversal lift forces, and also the particle rotation equation, are usually neglected. Given the above, the equation for the particle position is retained as is (Equation 3.29),

$$\frac{\mathrm{d}\mathbf{x_p}}{\mathrm{d}t} = \mathbf{u_p}\,,$$

and the equation for the particle linear velocity is:

$$m_p\frac{\mathrm{d}\mathbf{u_p}}{\mathrm{d}t} = V_p\boldsymbol{\nabla}\cdot\overline{\boldsymbol{\tau}_g} + \mathbf{F_D} + m_p\mathbf{g}\,.$$

---

[1] CFB riser cases are the main simulations utilizing the dense flow formulation that the present thesis is concerned about.

The drag force general expression is modified in comparison to Equation 3.37, where now the relative gas-particle velocity is multiplied by the gas volume fraction:

$$\mathbf{F_D} = \frac{1}{2}\rho_g A_p C_D \alpha_g \|\mathbf{U}_g - \mathbf{u}_p\| \alpha_g (\mathbf{U}_g - \mathbf{u}_p)\,. \tag{3.87}$$

The drag force correlation also must be modified since the previously discussed ones are only valid for isolated spheres. For the present case, where multiple particles are close to each other, an expression derived from DNS simulations by Tenneti *et al.* (2011) is utilized, following Capecelatro and Desjardins (2013):

$$\begin{aligned} C_D = \frac{24}{\mathrm{Re}_{p,\alpha}} \Bigg[& \frac{\left(1 + 0.15\mathrm{Re}_{p,\alpha}^{0.687}\right)}{\alpha_g^2} \\ & + 5.81\frac{1-\alpha_g}{\alpha_g^2} + 0.48\frac{(1-\alpha_g)^{1/3}}{\alpha_g^3} \\ & + \alpha_g(1-\alpha_g)^3 \mathrm{Re}_{p,\alpha}\left(0.95 + 0.61\frac{(1-\alpha_g)^3}{\alpha_g^2}\right)\Bigg]\,, \end{aligned} \tag{3.88}$$

where

$$\mathrm{Re}_{p,\alpha} = \frac{\rho_g \alpha_g \|\mathbf{U}_g - \mathbf{u}_p\| d_p}{\mu}\,. \tag{3.89}$$

A comparison of the drag force evaluated by the standard expression using the Schiller and Naumann (1935) correlation with the modified one using the Tenneti *et al.* (2011) correlation is shown in Figure 6. In this comparison, the increase in drag that particle populations are subject to in relation to isolated ones, becomes very evident. Also, this increase keeps growing as the the gas volume fraction decreases.

3.2.3 Euler-Lagrange coupling

The coupling between gas and particle phase is different, but mathematically equivalent, in the dense formulation than it was in the dilute one. In the present formulation, the gas-particle interaction force is introduced as the weighted sum of the fluid-exerted force on the particle, defined in Equation 3.86, over all particles:

$$\mathbf{F_{gp}} = \sum_{i=1}^{n_p} g(\|\mathbf{x} - \mathbf{x}_i\|)\mathbf{f}_i\,. \tag{3.90}$$

Note that the summation is essentially equivalent to the gas-particle interaction term for the dilute formulation. However, for the dense formulation, there are more appropriate manners to do this calculation numerically, which will be discussed in section 4.2.

This new definition allows to shed some light on the mathematical integration presented in Equation 3.75. Let us multiply Equation 3.86 by the filtering kernel $g(\|\mathbf{x} - \mathbf{x}_p\|)$ and sum over all particles:

$$\sum_{i=1}^{n_p} g(\|\mathbf{x} - \mathbf{x}_i\|)\mathbf{f} = \sum_{i=1}^{n_p} g(\|\mathbf{x} - \mathbf{x}_i\|) V_p \boldsymbol{\nabla} \cdot \overline{\boldsymbol{\tau}_g} + \sum_{i=1}^{n_p} g(\|\mathbf{x} - \mathbf{x}_i\|) \int_{S_p} \boldsymbol{\tau}_g' \cdot \mathbf{n}\,\mathrm{d}\mathbf{y}\,. \tag{3.91}$$

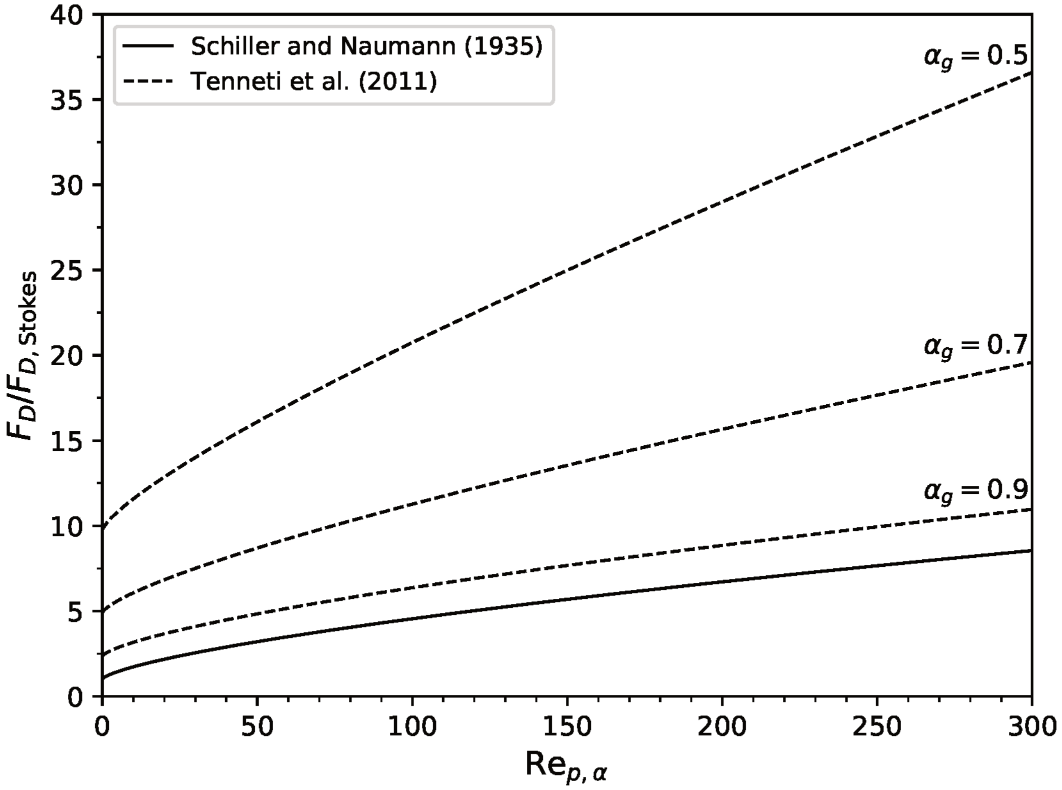

Figure 6 – Comparison of the particle drag force evaluated in the dilute and dense flow formulations.

Then, rearranging the equation above around its last term, using Equation 3.60 and Equation 3.90, Equation 3.75 is retrieved:

$$\sum_{i=1}^{n_p} g(\|\mathbf{x} - \mathbf{x}_i\|) \int_{S_p} \boldsymbol{\tau}_g' \cdot \mathbf{n} \, \mathrm{d}\mathbf{y} = \mathbf{F}_{\mathbf{gp}} - \alpha_p \boldsymbol{\nabla} \cdot \overline{\boldsymbol{\tau}_g} \,, \tag{3.92}$$

given that

$$\sum_{i=1}^{n_p} \int_{S_i} \mathbf{n} \cdot \boldsymbol{\tau}_g'(\mathbf{y}, t) g(\|\mathbf{x} - \mathbf{y}\|) \, \mathrm{d}\mathbf{y} \approx \sum_{i=1}^{n_p} g(\|\mathbf{x} - \mathbf{x}_i\|) \int_{S_p} \boldsymbol{\tau}_g' \cdot \mathbf{n} \, \mathrm{d}\mathbf{y} \tag{3.93}$$

after the simplification that $g(\|\mathbf{x} - \mathbf{y}\|)$ varies only a little over the distance of a particle diameter.

Regarding the ways in which the coupling can be carried out, there is no mathematical possibility to have a true one way coupling anymore. The presence of the volume fraction in the gas flow equations, already adds a level of coupling between the phases, such that two-way would be the lowest viable level of coupling. However, when a dense formulation is sought, is often because the loading of particles is very high, and thus, particle-particle collisions should not be neglected. Thus, in a dense formulation, often the four-way coupling is the only one utilized.

3.3 Other models

Some models are independent to whatever fluid or particle formulation is being utilized, be that either the dilute or dense formulation. Such models are presented in this section. Firstly, the so-called turbulent dispersion model is introduced, which has to be utilized to take an estimative of the fluid fluctuation velocity into account in the fluid-particle forces correlations. Then, the model to handle all particle collisions is presented, showing the generic hard-sphere model, which is then applied with modifications to handle the particle-particle and particle-wall collisions.

3.3.1 Turbulent dispersion

In the calculation of the gas-solid interaction force in both dilute and dense formulation (see subsection 3.1.2 and subsection 3.2.2), there is a dependency to the relative velocity between gas and particle. However, note that the gas velocity being utilized to calculate this relative velocity, is its filtered velocity, and using only this filtered velocity, without accounting for the turbulence of the fluid, can lead to erroneous results. To correct this, it is common to employ the so called turbulent dispersion models, which provide a way to estimate the fluid fluctuation velocity term from its turbulence resolved variables, in the present case k and ε. Note that in the present thesis, this term is only accounted for in the drag force, as experience shows that this is where this term makes the most difference.

The model utilized in the present thesis is based on a Langevin equation model, as taken from Sommerfeld *et al.* (1993 apud SOMMERFELD, 2001). Over the years, some constants suggested in the first works of Prof. Sommerfeld were changed, and the model presented herein follows more recent ones, such as Laín and Grillo (2007), Laín and Sommerfeld (2008) and all the ones following those. In this model, the gas fluctuation velocity at the m-th particle current position is correlated to the gas fluctuation velocity at the m-th particle previous position and to the gas turbulent quantities at the particle current position:

$$\mathbf{u}'_g\Big|_{p_m} = \mathbf{R}_p(\Delta t_p, \Delta\mathbf{r})\, \mathbf{u}'_g\Big|_{p_m^{(\text{old})}} + \sigma_g\sqrt{1-\mathbf{R}_p^2(\Delta t_p, \Delta\mathbf{r})}\,\xi\,, \tag{3.94}$$

where $\mathbf{R}_p(\Delta t_p, \Delta\mathbf{r})$ is a correlation function, σ_g is an estimate of the gas mean fluctuation velocity, and ξ is a normally distributed random number with mean value of zero and variance one.

The correlation function is composed by a Lagrangian part (R_L), which is a function of the Lagrangian time-step Δt_p, and an Eulerian part ($\mathbf{R}_E$), which is a function of the distance vector between the fluid particle and the actual solid particle $\Delta\mathbf{r}$. This dual part correlation is utilized in order to account for the crossing trajectories effect (CSANADY, 1963). The equation for $\mathbf{R}_p(\Delta t_p, \Delta\mathbf{r})$ is:

$$\mathbf{R}_p(\Delta t_p, \Delta\mathbf{r}) = R_L(\Delta t_p)\,\mathrm{diag}\Big(\mathbf{R}_E(\Delta\mathbf{r})\Big)\,, \tag{3.95}$$

where

$$R_L(\Delta t_p) = \exp\left(-\frac{\Delta t_p}{T_L}\right)\,, \tag{3.96}$$

and

$$\mathbf{R}_E(\Delta\mathbf{r}) = [f(\Delta\mathbf{r}) - g(\Delta\mathbf{r})]\frac{\Delta\mathbf{r}\Delta\mathbf{r}}{\|\Delta\mathbf{r}\|^2} + g(\Delta\mathbf{r})\mathbf{I}\,. \tag{3.97}$$

In addition to that, the Lagrangian integral time scale is

$$T_L = 0.24\frac{\sigma_g^2}{\varepsilon}\,, \tag{3.98}$$

and the functions f and g are

$$f(\Delta\mathbf{r}) = \exp\left(-\frac{\Delta\mathbf{r}}{L_E}\right)\,, \tag{3.99}$$

and

$$g(\Delta\mathbf{r}) = \left(1 - \frac{\Delta\mathbf{r}}{2L_E}\right) f(\Delta\mathbf{r})\,, \tag{3.100}$$

where the Eulerian length scale is

$$L_E = 3.0 T_L \sigma_g\,. \tag{3.101}$$

Finally, a good estimate for the gas mean fluctuation velocity can be taken from the very own definition of the turbulent kinetic energy k:

$$\sigma_g = \sqrt{\frac{1}{3}\left(\left\|\mathbf{u}_g'\right\|^2\right)} = \sqrt{\frac{2}{3}k}\,. \tag{3.102}$$

Note that this model introduced some quantities that may have a somewhat vague meaning right now, namely, the particle previous position $\mathbf{u}_g'^{\,(\mathrm{old})}$, the Lagrangian time-step Δt_p, and the distance between the fluid particle and the actual solid particle $\Delta\mathbf{r}$. However, their meaning will become clearer once the temporal and spatial discretization for the equations presented in this chapter are discussed in chapter 4.

3.3.2 Hard-sphere collision model

In the particle modeling utilized in the present thesis, there is the need to account for two types of collisions, namely the particle-particle and particle-wall collisions. Both of them are based on the hard-sphere model equations, but with further adjustments. Thus, firstly the hard-sphere collision model is presented generically, and following that, the appropriate specifics for each model are discussed. The model presented here is taken from Crowe *et al.* (2011).

The relations between pre- and post-collisional linear and angular velocities, for when the particles are allowed to slide in the tangential direction, are

$$\mathbf{u}_{p,1} = \mathbf{u}_{p,1}^{(0)} - (\mathbf{n} + f\mathbf{t})(\mathbf{n} \cdot \mathbf{G}^{(0)})(1+e)\frac{m_{p,2}}{m_{p,1} + m_{p,2}} \tag{3.103}$$

and

$$\boldsymbol{\omega}_{p,1} = \boldsymbol{\omega}_{p,1}^{(0)} - \frac{5}{d_{p,1}}(\mathbf{n} \cdot \mathbf{G}^{(0)})(\mathbf{n} \times \mathbf{t})f(1+e)\frac{m_{p,2}}{m_{p,1} + m_{p,2}}\,, \tag{3.104}$$

where the superscript "(0)" indicates the pre-collisional velocity and no superscript is the post-collisional velocity, the numeric subscript indicates the two colliding particles, $\mathbf{n}$ and $\mathbf{t}$ are the normal and tangential directions to the collision respectively, f is the friction coefficient to the Coulomb's law for friction, e is the restitution coefficient defined as the ratio between the pre- and post-collisional velocities in the normal direction, mathematically

$$e = -\frac{\mathbf{n} \cdot \mathbf{G}}{\mathbf{n} \cdot \mathbf{G}^{(0)}}\,, \tag{3.105}$$

the pre-collisional relative velocity is

$$\mathbf{G}^{(0)} = \mathbf{u}_{p,1}^{(0)} - \mathbf{u}_{p,2}^{(0)}\,, \tag{3.106}$$

and the post-collisional relative velocity is

$$\mathbf{G} = \mathbf{u}_{p,1} - \mathbf{u}_{p,2}\,. \tag{3.107}$$

If the tangential force is not high enough to maintain the sliding, the Coulomb's law for friction does not hold anymore, and the particle rolling has to be accounted for. The equations are then

$$\mathbf{u}_{p,1} = \mathbf{u}_{p,1}^{(0)} - \left[(1+e)(\mathbf{n} \cdot \mathbf{G}^{(0)})\mathbf{n} + \frac{2}{7}\left\|\mathbf{G}_{ct}^{(0)}\right\|\mathbf{t}\right]\frac{m_{p,2}}{m_{p,1} + m_{p,2}} \tag{3.108}$$

and

$$\boldsymbol{\omega}_{p,1} = \boldsymbol{\omega}_{p,1}^{(0)} - \frac{10}{7d_{p,1}}\left\|\mathbf{G}_{ct}^{(0)}\right\|(\mathbf{n} \times \mathbf{t})\frac{m_{p,2}}{m_{p,1} + m_{p,2}}\,, \tag{3.109}$$

where $\mathbf{G}_{ct}^{(0)}$ is the tangential component of the pre-collisional relative velocity at the contact point $\mathbf{G}_{c}^{(0)}$, given respectively by

$$\mathbf{G}_{ct}^{(0)} = \mathbf{G}_{c}^{(0)} - (\mathbf{G}_{c}^{(0)} \cdot \mathbf{n})\mathbf{n}\,, \tag{3.110}$$

and

$$\mathbf{G}_{c}^{(0)} = \mathbf{G}^{(0)} + \frac{d_{p,1}}{2}\boldsymbol{\omega}_{p,1}^{(0)} \times \mathbf{n} + \frac{d_{p,2}}{2}\boldsymbol{\omega}_{p,2}^{(0)} \times \mathbf{n}\,. \tag{3.111}$$

Note that following the definition of $\mathbf{G}_{ct}^{(0)}$, the tangential direction unit vector can be easier determined using

$$\mathbf{t} = \frac{\mathbf{G}_{ct}^{(0)}}{\left\|\mathbf{G}_{ct}^{(0)}\right\|}\,. \tag{3.112}$$

The sliding condition is checked using the inequality

$$\frac{\mathbf{n}\cdot\mathbf{G}^{(0)}}{\left\|\mathbf{G}_{ct}^{(0)}\right\|} < \frac{2}{7}\frac{1}{f(1+e)}\,, \tag{3.113}$$

where Equations 3.103 and 3.104 are used in case the condition above is true, and Equations 3.108 and 3.109 if false.

The equations for the partner particle, denoted by the numeric subscript “2”, would be similar. However, as will become clear in the next sections, they will not be necessary, because in the case of particle-particle collision the partner particle is fictitious, and in the case of particle-wall collision the partner is the wall itself, which will occur in some simplifications.

3.3.2.1 Stochastic particle-particle collision

In the standard hard-sphere model the collisions have to be checked by comparing the trajectories of pairs of particles: if the trajectories intersect within the time-step, a collision occurs; otherwise, it does not (BREUER; ALLETTO, 2012). However, this collision searching algorithm can take up to the order of $\mathcal{O}(n_p^2)$, if not efficiently programmed. Due to this high computational cost, and given the goal of the present thesis to provide a reasonably cheap model for dense gas-solid flows, a stochastic search of particle-particle collisions is employed. This stochastic model is coupled with the hard-sphere model, and follows the works of Oesterlé and Petitjean (1993) and Sommerfeld (2001).

To reduce the computational cost, the collision is not realized by the convergence of particles trajectories, but rather by statistical chance. To each real particle, a chance of collision is assigned accordingly to the concentration of particles in its vicinity, and to the diameter and velocity of its collision partner and its own. The probability of collision P_{coll} can be determined from

$$P_{\text{coll}} = 1 - \exp(-f_{\text{coll}}\Delta t)\,, \tag{3.114}$$

where the frequency of collisions f_{coll} is given from an analogy to the kinetic theory of gases, namely:

$$f_{\text{coll}} = \frac{\pi}{4}(d_{p,1}+d_{p,2})^2\|\mathbf{u}_{p,1}-\mathbf{u}_{p,2}\|\frac{n_p}{V}\,, \tag{3.115}$$

where n_p/V is the number of particles in the volume of the vicinity considered. Note that later in chapter 4 the size of the vicinity will turn out to be the discretization cell. The decision to whether or not the collision occurs is then made by drawing a uniformly distributed random number in the interval [0, 1] and comparing it to the probability calculated in Equation 3.114. The collision happens if the random number is smaller than the probability.

Although using the equations above already lowers the computational cost, each particle would still need to be compared to every other one in the domain to calculate the probabilities. To further reduce the cost, each real particle is compared only to one fictitious particle. This fictitious particle has its properties statistically drawn from distributions based on all particles of the vicinity. A log-normal distribution is utilized to describe the particle diameter (HEINTZENBERG, 1994), and a normal distribution for the linear and angular particle velocities:

$$d_{p,2} = d_{p,\text{fict.}} = \exp\left\{\mathrm{E}[\ln(d_p)] + \mathrm{Var}[\ln(d_p)]\xi\right\}, \tag{3.116}$$

$$\mathbf{u}_{p,2} = \mathbf{u}_{p,\text{fict.}} = \mathrm{E}[\mathbf{u}_p] + \mathrm{Var}[\mathbf{u}_p]\xi + \mathbf{u}'_{p,\text{fict.}}, \tag{3.117}$$

$$\boldsymbol{\omega}_{p,2} = \boldsymbol{\omega}_{p,\text{fict.}} = \mathrm{E}[\boldsymbol{\omega}_p] + \mathrm{Var}[\boldsymbol{\omega}_p]\xi, \tag{3.118}$$

where $\mathrm{E}[X]$ is the expected value (mean) of X, $\mathrm{Var}[X]$ is the variance of X, and ξ is a random normal value with $\mathrm{E}[\xi] = 0$ and $\mathrm{Var}[\xi] = 1$. The mean and variance of $\ln(d_p)$ can be calculated from the mean and variance of d_p, which are known, as follows:

$$\mathrm{E}[\ln(d_p)] = \ln(\mathrm{E}[d_p]) - \frac{1}{2}\mathrm{Var}[\ln(d_p)], \tag{3.119}$$

$$\mathrm{Var}[\ln(d_p)] = \ln\left(\frac{\mathrm{Var}[d_p]}{(\mathrm{E}[d_p])^2} + 1\right). \tag{3.120}$$

Note that in the process of generating the fictitious particle linear velocity, the influence of the turbulent dispersion must also be taken into account:

$$\mathbf{u}'_{p,\text{fict.}} = R(\mathrm{St})\, \mathbf{u}'_g\Big|_{p_1} + \boldsymbol{\sigma}_p\sqrt{1 - R(\mathrm{St})^2}\xi \tag{3.121}$$

where

$$R(\mathrm{St}) = \exp\left(-0.55\,\mathrm{St}^{0.4}\right), \tag{3.122}$$

$\mathbf{u}'_g\Big|_{p_1}$ comes from Equation 3.94, and $\boldsymbol{\sigma}_p$ is the actual RMS fluctuation velocity of the real particle. The Stokes number definition utilized here is the following:

$$\mathrm{St} = \frac{\rho_p d^2_{p,\text{fict.}}}{18\mu}\frac{1}{T_E}, \tag{3.123}$$

where the Eulerian turbulence time scale is

$$T_E = 0.3\frac{k}{\varepsilon} \tag{3.124}$$

Once the fictitious collision partner has been defined, and the chance of that collision occurring has been calculated, one needs to settle the point of collision at the real particle surface so that the normal and tangential collision vectors can be determined. The

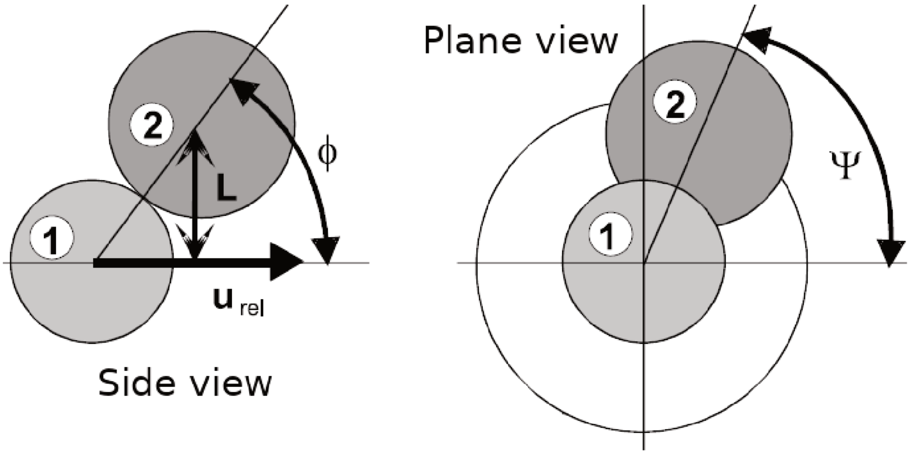

Figure 7 – Collision angles from a reference in the coordinated system centered on the particle. Adapted from Sommerfeld (2001).

point of collision is also given by chance using two angles with reference in a coordinate system centered on the particle, as shown in Figure 7. The first angle is determined from

$$\begin{aligned} L &= \sqrt{\xi_x^2 + \xi_z^2} \qquad \text{with } L < 1\,, \\ \phi &= \arcsin(L)\,, \end{aligned} \tag{3.125}$$

where ξ_x and ξ_z are uniform random numbers in the range [0, 1]; and Ψ is a uniform random number in the range $[0,\ 2\pi]$.

To determine the normal collision vector, it is easier to firstly identify the unit vectors in the coordinate system defined with the help of the relative velocity between the two particles $\mathbf{u}_{p,\text{rel}}$. The normal vector of this new coordinate system is parallel to the relative velocity vector itself:

$$\mathbf{n}_\text{rel} = \frac{\mathbf{u}_{p,\text{rel}}}{\|\mathbf{u}_{p,\text{rel}}\|}\,. \tag{3.126}$$

Then, the tangent and binormal vectors can be determined using the second and third columns of the Householder matrix (LOPES *et al.*, 2013):

$$\mathbf{t}_\text{rel} = \begin{cases} \begin{bmatrix} -n_{\text{rel},y} & 1 - \dfrac{n_{\text{rel},y}^2}{n_{\text{rel},x}+1} & -\dfrac{n_{\text{rel},y}n_{\text{rel},z}}{n_{\text{rel},x}+1} \end{bmatrix}^\text{T} & \text{if } n_{\text{rel},x} \geq 0\,, \\ \begin{bmatrix} n_{\text{rel},y} & 1 + \dfrac{n_{\text{rel},y}^2}{n_{\text{rel},x}-1} & \dfrac{n_{\text{rel},y}n_{\text{rel},z}}{n_{\text{rel},x}-1} \end{bmatrix}^\text{T} & \text{otherwise}\,; \end{cases} \tag{3.127}$$

$$\mathbf{b}_\text{rel} = \begin{cases} \begin{bmatrix} -n_{\text{rel},z} & -\dfrac{n_{\text{rel},y}n_{\text{rel},z}}{n_{\text{rel},x}+1} & 1 - \dfrac{n_{\text{rel},z}^2}{n_{\text{rel},x}+1} \end{bmatrix}^\text{T} & \text{if } n_{\text{rel},x} \geq 0\,, \\ \begin{bmatrix} n_{\text{rel},z} & \dfrac{n_{\text{rel},y}n_{\text{rel},z}}{n_{\text{rel},x}-1} & 1 + \dfrac{n_{\text{rel},z}^2}{n_{\text{rel},x}-1} \end{bmatrix}^\text{T} & \text{otherwise}\,. \end{cases} \tag{3.128}$$

Finally, the collision normal vector $\mathbf{n}$ can be determined using the principle of successive rotations (Euler angles). It is enough to rotate vector $\mathbf{n}_\text{rel}$ by ψ around the $\mathbf{n}_\text{rel}$

axis itself, and then ϕ around the $\mathbf{b}_{\mathrm{rel}}$ axis, resulting in the following rotation matrix:

$$\mathbf{R} = \begin{bmatrix} \cos\phi & -\sin\phi & 0 \\ \cos\psi\sin\phi & \cos\psi\cos\phi & -\sin\psi \\ \sin\psi\sin\phi & \sin\psi\cos\phi & \cos\psi \end{bmatrix} . \tag{3.129}$$

However, as the angles of rotation are defined in relation to the local coordinate system, in which the vector $\mathbf{n}_{\mathrm{rel}}$ is always $[1\ 0\ 0]^{\mathrm{T}}$, the collision normal vector is given simply by:

$$\mathbf{n} = \cos\phi\, \mathbf{n}_{\mathrm{rel}} + \cos\psi\sin\phi\, \mathbf{t}_{\mathrm{rel}} + \sin\psi\sin\phi\, \mathbf{b}_{\mathrm{rel}} . \tag{3.130}$$

This last part, the calculation of the the unit vectors using the Householder matrix, was introduced in the code during the present thesis. Before that, the determination of the collision normal angle was carried out in a simpler manner, but that could produce singularity values in very rare cases.

3.3.2.2 Particle-wall collisions

The particle-wall collision model can be regarded as a special case of two colliding spheres using the hard-sphere model, where the second sphere is the wall and will assume the following properties: $m_{p,2} >>> m_{p,1}$ such that

$$\frac{m_{p,2}}{m_{p,1} + m_{p,2}} \approx 1 , \tag{3.131}$$

$\mathbf{u}_{p,2} = 0$, $\boldsymbol{\omega}_{p,2} = 0$, and $d_{p,2} \to \infty$. Applying these simplifications to the standard hard-sphere model, the particle-wall collision equations become:

$$\mathbf{u}_{p,1} = \mathbf{u}_{p,1}^{(0)} - (\mathbf{n} + f\mathbf{t})(\mathbf{n} \cdot \mathbf{u}_{p,1}^{(0)})(1 + e) \tag{3.132}$$

and

$$\boldsymbol{\omega}_{p,1} = \boldsymbol{\omega}_{p,1}^{(0)} - \frac{5}{d_{p,1}}(\mathbf{n} \cdot \mathbf{u}_{p,1}^{(0)})(\mathbf{n} \times \mathbf{t}) f (1 + e) , \tag{3.133}$$

for a sliding condition of the particle;

$$\mathbf{u}_{p,1} = \mathbf{u}_{p,1}^{(0)} - \left[(1 + e)(\mathbf{n} \cdot \mathbf{u}_{p,1}^{(0)})\mathbf{n} + \frac{2}{7}\left\|\mathbf{G}_{ct}^{(0)}\right\|\mathbf{t}\right] \tag{3.134}$$

and

$$\boldsymbol{\omega}_{p,1} = \boldsymbol{\omega}_{p,1}^{(0)} - \frac{10}{7d_{p,1}}\left\|\mathbf{G}_{ct}^{(0)}\right\|(\mathbf{n} \times \mathbf{t}) , \tag{3.135}$$

for non-sliding. The pre-collisional relative velocity at the contact point can also be simplified as

$$\mathbf{G}_{c}^{(0)} = \mathbf{u}_{p,1}^{(0)} + \frac{d_{p,1}}{2}\boldsymbol{\omega}_{p,1}^{(0)} \times \mathbf{n} , \tag{3.136}$$

and the test to the sliding condition becomes

$$\frac{\mathbf{n} \cdot \mathbf{u}_{p,1}^{(0)}}{\left\|\mathbf{G}_{ct}^{(0)}\right\|} < \frac{2}{7}\frac{1}{f(1 + e)} . \tag{3.137}$$

A simpler expression is often presented in the literature if one defines a new coordinate system aligned with the wall normal vector. It is an obvious choice to align the normal collision vector with one of the coordinate system axis, and the other two in the tangential direction. However, that would need a transformation of the reference system to come back to the fluid flow coordinate system. That approach is not followed in the present thesis.

Although the recently presented model is enough to account for the particle-wall collisions, it leaves out the influence of the wall material roughness, which is a very important feature to correctly predict the velocity and distribution of the particles in particle-laden flows, as shown by many (SOMMERFELD; HUBER, 1999; KUSSIN; SOMMERFELD, 2002; SOMMERFELD; KUSSIN, 2004; BENSON *et al.*, 2005; LAÍN; SOMMERFELD, 2012; ALLETTO; BREUER, 2013; SOUZA *et al.*, 2014; VREMAN, 2015; SOLNORDAL *et al.*, 2015b; DUARTE *et al.*, 2017). In the present thesis, the wall roughness is accounted for utilizing the procedure detailed in Sommerfeld and Huber (1999), where the rebound angle of the particle leaving the wall is composed assumed to have a stochastic contribution added to the incoming angle:

$$\theta_{\text{reb.}} = \theta_{\text{inc.}} + \Delta\gamma\ \xi\,, \tag{3.138}$$

where $\Delta\gamma$ is the parameter that controls the wall roughness and ξ is a normally distributed random number with mean zero and variance one. The roughness parameter is known to a certain extend for common cases from the works of Prof. Sommerfeld's group, but in other cases it depends on trial and error to adjust the value.

Chapter 4

Numerical and computational methods

> *In this chapter, the mathematical models stated in the last chapter are discussed in matters of how to solve them numerically using computational tools. "Computers can do two things: (1) move data form one place to another and (2) linear algebra". (Mark Hoemmen,* Sandia Labs*, as cited by Paul Constantine @DrPaulynomial).*

In the previous chapter, the complete set of the mathematical equations suitable to model all gas-particle flows concerned in the present thesis were presented and discussed. However, the solution of such equations is not straightforward. For the gas-phase equations, for instance, currently there is not a single mathematical method that can be applied to solve such equations in a three-dimensional and transient framework such as needed in here. On the other hand, the particle-phase equations are much simpler, but still cannot be solve analytically due to the dependency on the gas velocity.

Because of such difficulties, the equations are discretized in space and time to be available for solving by numerical methods, which are implemented in the UNSCYFL3D code. Also a number of other methods are necessary, for example, particle tracking algorithms, calculation of cell volumes, and others, which are not numerical equation solving methods, but are computational ones, and shall also be presented here.

All the methods presented in this chapter are more completely described and discussed in the references cited herein, as the intention here is not to provide a review of the already established methods, but merely present them as part of the methodology utilized in the present thesis. Also, to show every detail of the numerical and computational algorithms utilized in the UNSCYFL3D code would be prohibitive as it alone would take its own document. The reader is referred to earlier implementation theses and articles such as Salvo (2013), Souza *et al.* (2014) and Martins (2016), for more information. However, when deemed necessary as in the case of some newer methods that were implemented during and for the present thesis, a more thorough discussion is presented.

4.1 Gas phase

Given the difficulty in solving the fluid flow equations, CFD has risen as one of the most utilized tool for engineering analysis of fluid flows. The numerical method mostly utilized for the numerical solution in CFD is the Finite Volume Method (FVM), which is thoroughly described in many textbooks, not only classical ones (PATANKAR, 1980; MALISKA, 2004), but also reedited classical (FERZIGER *et al.*, 2020) and new ones (MOUKALLED *et al.*, 2016). All the methods presented in the current section are derived from the adoption of the discretization of the mathematical equations by the FVM, and are needed for a complete and suitable discretization of the mathematical equations into the computer code for numerical solving.

4.1.1 Finite Volume Method

The FVM consists on discretizing both space and time considered in the analysis, similarly to other approaches such as the finite differences method, and then integrating the transport equations in such multiple discretized domains. The pieces derived from the discretized domain are the mesh cells, an the size of the discretization in the time is the time-step. Such procedure will turn the Partial Differential Equations (PDE) into a system of algebraic equations. Such system is usually non-linear, but it is linearized for solving.

Using a generic variable ϕ to represent all transported variables using a single transport equation, and recalling the Gauss-Ostrogradsky divergence theorem to represent a volume integral of a divergent as a surface integral, the FVM can be briefly represented as follows:

$$\int_{V_C} \frac{\partial}{\partial t}(\alpha_g \rho_g \phi)\,\mathrm{d}V + \oint_{S_C} (\alpha_g \rho_g \mathbf{U}_g \phi) \cdot \mathbf{n}\,\mathrm{d}S = \oint_{S_C} (\Gamma \boldsymbol{\nabla} \phi) \cdot \mathbf{n}\,\mathrm{d}S + \int_{V_C} S_\phi\,\mathrm{d}V \ , \tag{4.1}$$

where V_C indicates the integration over the control volume delineated by the discretized space (the computational cell) V, S_C indicates the closed surface integral over all the faces that form the surface of the computational cell S, Γ is a generic diffusion coefficient, and S_ϕ a generic source term.

Under the classical assumptions of the FVM method, Equation 4.1 becomes

$$\left[\frac{\partial}{\partial t}(\alpha_g \rho_g \phi)\right]\Bigg|_C V_C + \sum_{f\sim \mathrm{nb}(C)} \dot{m}_f \phi_f = \sum_{f\sim \mathrm{nb}(C)} \Big[\Gamma(\boldsymbol{\nabla}\phi \cdot \mathbf{n})S\Big]\Big|_f + S_\phi\Big|_C V_C \tag{4.2}$$

for a given cell C sharing the faces f with its neighboring cells, where

$$\dot{m}_f = \Big[\alpha_g \rho_g (\mathbf{U}_g \cdot \mathbf{n}) S\Big]\Big|_f \ . \tag{4.3}$$

Note that the introduction of α_g does not bring great difficulties into the discretized equation if compared to the standard one (recalled by taking $\alpha_g = 1$), and one just needs to take a bit o care in redoing all discretization steps to not miss any accounting of the new variable. The only term where it appears explicitly is in the transient term, but which does not complicate the discretization. In the advection term, α_g is incorporated into the face mass flux, which also simplifies all the changing in the code in relation to the old formulation. One addition that has to be paid attention to, is the transient term in the continuity equation, for in the standard formulation this term was non-existent. With this addition, a new term will appear in the pressure-correction equation of the SIMPLE algorithm (see subsection 4.1.5).

4.1.2 Discretization of terms

The discretization of the terms in Equation 4.2 are discussed in the present section. The discretization of the volume fraction at the cell face α_f is carried out using central differences, i.e. assuming a linear change between cell centers.

The transient term is discretized differently for the dilute and for the dense formulation. In the former, the *Second Order Upwind Euler* (SOUE) scheme is applied, which is second-order accurate using three time levels. On the other hand, in the dense formulation due to difficulties in the convergence and for a more fast testing of the new implementation, the *First Order Implicit Euler* one was utilized. Note that in both formulations the temporal discretization was carried out in an implicit way, in which all remaining terms of Equation 4.2 are taken at the newest time-level. The implicit time discretization generate a linear system that needs to be solved iteratively for each time-step.

In the advective term (second term on the LHS), one notes that the variables have to be evaluated at the cell face instead of in the center. The evaluation of ϕ_f follows the *Second Order Upwind* (SOU) scheme in a *Deferred Correction* (DC) approach (KHOSLA; RUBIN, 1974). The DC approach is utilized to provide more stability in the solution by increasing the diagonal dominance of the linear system. This is achieved by splitting the SOU estimation of the face values in an implicit part of lower order, using the *Upwind* (U) scheme, plus an explicit part (evaluated at the old time-level) of higher order, mathematically:

$$\dot{m}_f \phi_f^{(\mathrm{SOU})} = \underbrace{\dot{m}_f \phi_f^{(\mathrm{U})}}_{\text{implicit}} + \underbrace{\dot{m}_f \left(\phi_f^{(\mathrm{SOU})} - \phi_f^{(\mathrm{U})} \right)}_{\text{explicit}} . \tag{4.4}$$

The diffusive (gradient-related) term is accounted in the cell face assuming that ϕ varies linearly between cell centroids, i.e. utilizing the *Central Differencing* scheme. However an important part of this discretization is to account for the possible non-orthogonality of the mesh. In the UNSCYFL3D the correction by Mathur and Murthy (1997) is employed, namely the *over-relaxed* approach (MOUKALLED *et al.*, 2016).

4.1.3 Linear system

Replacing all discretized terms into Equation 4.2 and making all modifications in the boundary cells due to the chosen boundary conditions will result in a linear system of the following kind:

$$a_C \phi_C + \sum_{F \sim \mathrm{NB}(C)} a_F \phi_F = b_C \,, \tag{4.5}$$

where a is the coefficient matrix, F denote the neighboring cells of cell C, and b is the vector that sums up all explicit terms.

This equation is written for each one of the computational cells of the mesh, which are dependent on each other, hence producing a system of equations. This algebraic equation system is solved in the UNSCYFL3D using the *Bi-Conjugate Gradient* method (BiCG) with *Successive Over-Relaxation* (SOR). The only exception is the linear system formed by the pressure correction equation which needs a special algorithm (discussed in the next subsection).

4.1.4 Rhie-Chow interpolation

It is also an already established concept that in incompressible segregated solution approaches for collocated meshes, a special interpolation must be considered for the gas face velocity utilized in Equation 4.3, namely the Rhie-Chow interpolation (RHIE; CHOW, 1983). In the previous version of the UNSCYFL3D code the basic version of the Rhie-Chow interpolation was applied:

$$\mathbf{U}_g\Big|_f = \left\langle \mathbf{U}_g\Big|_f \right\rangle - \frac{\langle V_f \rangle}{\langle a_f \rangle}\Big(\boldsymbol{\nabla} P_f - \langle \boldsymbol{\nabla} P_f \rangle\Big) \,, \tag{4.6}$$

where the $\langle \quad \rangle$ operator indicates a quantity calculated by a simple linear interpolation in opposition to the true value at the face, and the relation between the face interpolated Volume and a is

$$\frac{\langle V_f \rangle}{\langle a_f \rangle} = \frac{V_C + V_F}{a_C + a_F} \,. \tag{4.7}$$

Note that the "true" value of the pressure gradient in the above case would be calculated by taking the gradient directly into the face by a method such as the Green-Gauss or the least-square. In the present thesis, the Green-Gauss is utilized.

However, recent advances in this area have been showing that more additions to Equation 4.6 are necessary in order to provide more accurate results (ZHANG *et al.*, 2014; CUBERO *et al.*, 2014; MOUKALLED *et al.*, 2016; TUKOVIĆ *et al.*, 2018; BARTHOLOMEW *et al.*, 2018). For instance, in order to guarantee a time-step independent interpolation, the following term has been added to the RHS (already accounting for the volume-averaged equations):

$$\frac{\rho_g}{\Delta t}\frac{\langle V_f\rangle}{\langle a_f\rangle}\left[\left(\alpha_g\mathbf{U}_g\right)\Big|_f^{\text{old}} - \left\langle\left(\alpha_g\mathbf{U}_g\right)\Big|_f^{\text{old}}\right\rangle\right]. \tag{4.8}$$

Other additions to the Rhie-Chow interpolation equation are also recommended, such as the correction for relaxation independent results. However, in the present work this correction was not added as its influence is very small. Another inclusion that was tested was for the correction related to the source terms. Summing up all source terms (gravity related and particle related) into a vector $\mathbf{B}$, one can account its correction in a simple manner as:

$$\frac{\langle V_f\rangle}{\langle a_f\rangle}\Big(\mathbf{B}_f - \langle\mathbf{B}_f\rangle\Big). \tag{4.9}$$

However, this correction is presented with different interpolations in each work. The simple method applied here showed almost no influence in the results and in the convergence because the sources terms due to the particle are already very smooth because of the artificial diffusion included. This diffusion is discussed in the next section, on the numerical and computational methods for the particle phase.

The final Rhie-Chow interpolation equation implemented and utilized in the present thesis is as follows:

$$\begin{aligned}\mathbf{U}_g\Big|_f = \left\langle\mathbf{U}_g\Big|_f\right\rangle - \frac{\langle V_f\rangle}{\langle a_f\rangle}\Big(\boldsymbol{\nabla}P_f - \langle\boldsymbol{\nabla}P_f\rangle\Big)&\\ + \frac{\rho_g}{\Delta t}\frac{\langle V_f\rangle}{\langle a_f\rangle}\left[\left(\alpha_g\mathbf{U}_g\right)\Big|_f^{\text{old}} - \left\langle\left(\alpha_g\mathbf{U}_g\right)\Big|_f^{\text{old}}\right\rangle\right]&\\ + \frac{\langle V_f\rangle}{\langle a_f\rangle}\Big(\mathbf{B}_f - \langle\mathbf{B}_f\rangle\Big).&\end{aligned} \tag{4.10}$$

Note that the works on Rhie-Chow interpolation consistently reiterate the importance of applying a consistent formulation in order to obtain consistent results and also to improve convergence. Of those, some also stress the influence of the correct interpolation taking into account the α_g, which needs to added in the derivation, in opposition to using the standard interpolation to a single-phase formulation (CUBERO *et al.*, 2014; BARTHOLOMEW *et al.*, 2018). In the present thesis, the implementation of the corrected Rhie-Chow interpolation was carried out in accordance to all remarks presented in the aforementioned works.

4.1.5 SIMPLE

The solution of the entire set of equations is performed in a segregated manner utilizing the Semi IMplicit Pressure Linked Equations (SIMPLE) algorithm Patankar (1980). This approach is well-know in the CFD literature, and only minor modifications need to be carried out in the equations in order to account for α_g. But the steps of the algorithm are the same.

The first step is solving the discretized momentum equations utilizing the previous estimates for the pressure and face velocities. The volume fraction is given and constant for the duration of the fluid time-step, as it is only updated in the particle iteration cycle. After this first estimative of the velocities, the cell face velocities (and consequently the cell face mass fluxes) can be corrected using the Rhie-Chow equation.

After the estimation of the velocities, a linear system for the pressure correction (P') is assembled:

$$a_C^{(P)} P'_C + \sum_{F \sim \mathrm{NB}(C)} a_F^{(P)} P'_F = b_C^{(P)} \,. \tag{4.11}$$

This system, however, has special characteristics that make it not suitable to be solved by the BiCG method as the other systems. In this case, the Algebraic Multi-Grid (AMG) method is utilized. The AMG utilized in the UNSCYFL3D code is taken from Notay (2010), with further improvements by Notay (2012) and Napov and Notay (2012)[1].

Note that for the volume-averaged equations some modifications are necessary on the coefficient of Equation 4.11:

$$\underbrace{a^{(P)}}_{\text{volume averaged}} = \alpha_g\Big|_f \underbrace{a^{(P)}}_{\text{standard}} \,, \tag{4.12}$$

and

$$\underbrace{b_C^{(P)}}_{\text{volume averaged}} = \underbrace{b_C^{(P)}}_{\text{standard}} + \frac{\rho_g V_C}{\Delta t}\left(\alpha_g\Big|_C - \alpha_g\Big|_C^{\text{old}}\right) , \tag{4.13}$$

where the $\alpha_g|_f$ multiplication in Equation 4.12 comes from the definition of the cell face mass flux in Equation 4.3, and the last term in Equation 4.13 is from the transient term in the continuity equation. This last term addition has shown to bring some convergence issues in some simulations.

After this step, the cell-center velocities, the cell faces mass flux and the cell-center pressure are updated with P' using the appropriate expressions. The discretized equations for the turbulence equations are solved next. Then, the convergence is checked and the loop is ran again as many times as needed in order to achieve convergence within the specified criteria.

4.2 Particle phase

In comparison to the gas phase numerical methods, the particle phase solution is much simpler on the numeric standpoint, given that the equations are mathematically simpler.

---

[1] Available at <agmg.eu>

However, many computational methods are necessary in order to correctly determine the position and velocity of the particles in the Eulerian space, and also to provide a reasonably computational cheap model.

4.2.1 Parcel representation

The computational requirements to solve each single particle present in a flow can become very high in some cases, see for instance industrial scale CFB risers that can hold up to 10^9 or even 10^{12} particles. Take the simple case where one would need to store only six basic information such as current position and linear velocity vector, this alone would require about 45 GigaBytes of memory. This is a uncommon value for RAM memory (fast access memory), and store such amount of information in hard drives would make a simulation many times slower. One common alternative to this problem, is to consider that one single Lagrangian entity, now called a parcel, is actually a representation of the position and velocity of several real particles. This way, the number of Lagrangian entities can be reduced by several orders of magnitude.

Although in the case of dilute flows the aforementioned problem is much less common, the parcel approach can also help when there are only a few real particles in the domain. In this case, a very long simulation would have to be run to achieve a smooth statistical field, for example. Using more parcels than the actual number of real particles would assign to them a fractional weight, but would speed up the statistical convergence.

4.2.2 ODE integration

The solution of the particle ordinary differential equations - namely Equations 3.29, 3.30 and 3.31 - is carried out using a numerical integration much simpler than the FVM. The algorithm is based on an analytic integration of the equations, assuming that $\mathbf{u}_p$ on the drag force relative velocity can be integrated, but the gas velocity, the Re_p, and all other forces a are constant during the time-step:

$$\mathbf{x}_p = \mathbf{x}_p^{(\mathrm{old})} + \mathbf{u}_g \Delta t_p + a\tau_p \Delta t_p + \left(\mathbf{u}_p^{(\mathrm{old})} - \mathbf{u}_g - a\tau_p\right)\tau_p\left(1 - e^{-\frac{\Delta t_p}{\tau_p}}\right); \tag{4.14}$$

$$\mathbf{u}_p = \mathbf{u}_g + e^{-\frac{\Delta t_p}{\tau_p}}\left(\mathbf{u}_p^{(\mathrm{old})} - \mathbf{u}_g\right) - a\tau_p\left(e^{-\frac{\Delta t_p}{\tau_p}} - 1\right); \tag{4.15}$$

$$\boldsymbol{\omega}_p = 0.5\boldsymbol{\omega}_g - \boldsymbol{\Omega}_{\mathrm{rel}}^{(\mathrm{old})} e^{-\Delta t_p C_R^*}; \tag{4.16}$$

where the gas instantaneous velocity is estimated using the turbulent dispersion model (see subsection 3.3.1)

$$\mathbf{u}_g = \left(\mathbf{U}_g + \mathbf{u}'_g\Big|_p\right), \tag{4.17}$$

the particle relaxation time is corrected for non-Stokes drag

$$\tau_p = \frac{1}{C_D}\frac{24}{Re_p}\frac{\rho_p d_p^2}{18\mu}\,, \tag{4.18}$$

and

$$C_R^* = \frac{C_R \rho_g d_p^5 \left\| \mathbf{\Omega}_{\text{rel}}^{(\text{old})} \right\|}{64 I_p}\,. \tag{4.19}$$

This approach is also utilized by Prof. Sommerfeld, and early tests from our research group in cyclones and pipe particle-laden flows, show that the present method achieves the same accuracy as a second-order Runge-Kutta method.

4.2.3 Interpolation and tracking

When the particle are at the exact location of the cell center, all gas properties at its location are easily determined, by the very own definition of the FVM. However, this is very unlikely to occur, and in that case it is very important that the gas properties are interpolated to the particle position for a more accurate prediction. In the UNSCYFL3D code, the Shepard (1968) algorithm for this interpolation is utilized. This algorithm is based on a simple mean weighted by the inverse of the distance to the neighbors of the host cell.

The tracking of the particle is another very important algorithm to take into account. This algorithm is responsible to assign each particle into its respective host cell. As the mesh is not structured, this assignment is not easy, and the calculations need to take into account each particle initial position, and initial host cell, to determine its final ones according to its displacement. In the UNSCYFL3D code, the algorithm from Haselbacher *et al.* (2007) is utilized, which can deal with polyhedral meshes and allows calculation when the particle crosses multiple cells.

4.2.4 Particle volume distribution

The inclusion of α_g in the mass and momentum equations for the gas phase solution, was performed during the present thesis. Beyond adding α_g and modifying some of the SIMPLE and Rhie-Chow equations, one special feature had to be added to the code, the diffusion of the α_g and $\mathbf{F}_{gp}$ field. As already discussed in section 2.3, this diffusion is carried out to promote the particle volume and forces distribution in all cells around the host cell (CAPECELATRO; DESJARDINS, 2013; SUN; XIAO, 2015b). This is particularly important near the walls, where the particles are larger than the cell. Also, this procedure stabilizes the solution, preventing nonphysical pressure oscillations (PENG *et al.*, 2014).

This algorithm starts by first calculating α_g and $\mathbf{F}_{gp}$ in each cell considering that all the value of a particle volume and interaction force is accounted for the host cell. In the next step, a controlled diffusion is introduced so that influence is spread in the neighboring cells. The transient diffusion equation

$$\frac{\partial \alpha_g}{\partial t^*} = D \nabla^2 \alpha_g \tag{4.20}$$

is solved after each particle cycle, to be used in the next gas time-step. Note that the same equation is also used to diffuse $\mathbf{F}_{gp}$. Equation 4.20 is solved in an independent time frame t^*, given as a function of the intended width of spread

$$D t^* = \frac{\delta_{\text{diff}}}{16 \ln 2} \, . \tag{4.21}$$

In the present thesis, the suggestions from Capecelatro and Desjardins (2013) were followed, where a value of $\delta_{\text{diff}} = 3 d_p$ is adopted for monodisperse flows and $\delta_{\text{diff}} = \max(d_p)$ for polydisperse ones.

This equation is also discretized using the FVM as described before, and is solved utilizing the BiCG method. The total time of diffusion is solved in three time-steps, following the considerations of Sun and Xiao (2015b). These authors showed that solving it in only one time-step may generate a spurious field, and more than three is unnecessary. We also tested this influence in a simple one-dimensional fictitious field, and achieved the same conclusion.

Note that as in the present thesis the concept of parcels is utilized, where many particles may be represented by a single one, and that the stochastic collision model does not prevent multiple particles to close together (even at the same position), it may occur that non-realistic α_g and $\mathbf{F}_{\text{gp}}$ fields are achieved. In such occasions, a limitation of $\alpha_g > 0.36$ (following the random packing theory) is applied so that there are no problems with the gas equations. However the limitation of $\mathbf{F}_{\text{gp}}$ is not straightforward, and has not been implemented in the current state of the UNSCYFL3D code. This brings convergence problems in locations with high concentrations of particles. This is discussed in section 6.3.

Chapter 5

Results and discussion: dilute flows

This chapter is dedicated to simulations and analyses carried out in dilute particle-laden cases. Simulations in horizontal and vertical ascending flows are performed to evaluate the influence of gas-particle coupling, turbulence closure model, particle mass loading, and also to validate some steps of the modeling.

Although the UNSCYFL3D code has been extensively utilized and validated for dilute particle-laden flows, many boundaries remain. One of them is that only monodisperse simulations had been performed before the present thesis, and another one is that only particle mass loadings up to $\eta = 1.0\,\mathrm{kg_{part.}/kg_{air}}$ has been simulated. In this chapter these boundaries are taken further in the direction of higher mass loadings, trying to reflect the situations that are encountered in risers, and trying to better understand the particle-laden flows characteristics and modeling features before going into dense flows. Horizontal and vertical ascending flows in pipes are presented to assess the effect of gas-particle coupling, turbulence closure model and particle mass loading on the predictions.

5.1 Polydisperse validation

The CFD code UNSCYFL3D has been extensively validated and utilized in a large number of dilute particle-laden flows in geometries like channels and circular pipes, as already mentioned. However, the earlier works have been carried out in monodisperse flows, where only one mean diameter had been assumed to represent the particles. At the very beginning of the present thesis, the code was being modified to be able to account for particles with a diameter distribution.

In light of the aforementioned, one of the first steps to the present thesis was to perform some simulations in already known validation cases in order to to verify the

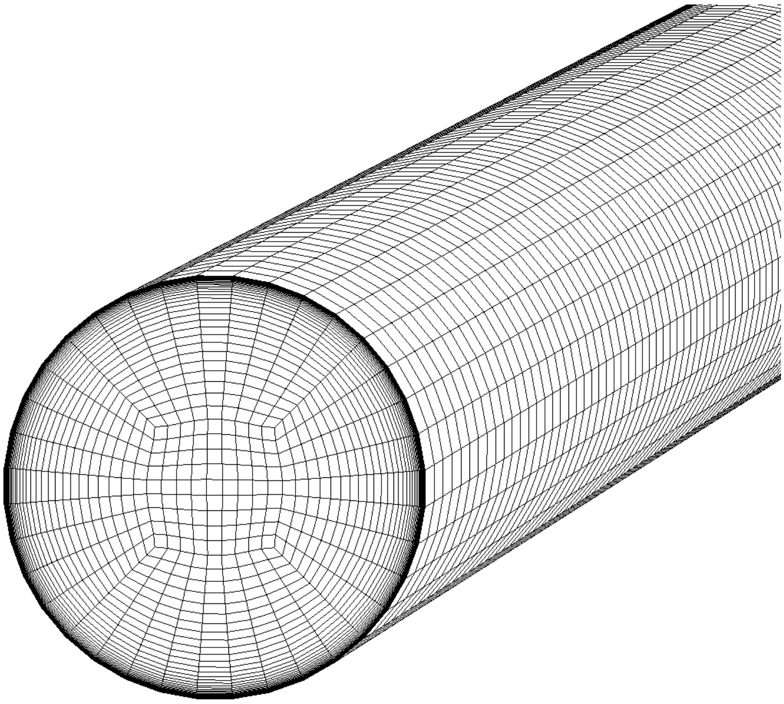

Figure 8 – Computational mesh utilized for circular pipes simulations.

implementation of the polydisperse model, but also to validate the model that had been subject to some early modifications, as stated throughout this document.

The validation performed in this section is a dilute particle-laden flow in a horizontal pipe, experimentally carried out by Huber and Sommerfeld (1998) (namely “Case 3”), and later also simulated by Laín and Sommerfeld (2013) using a very similar model as the present one.

5.1.1 Computational domain

The computational domain for the simulation is a circular pipe with 150 mm internal diameter and 10.6 m length. The construction of a computational mesh for circular pipes is very straightforward and was done by the use of the well-known O-Grid approach for hexahedral cells utilizing the commercial software ANSYS ICEMCFD. A total number of about 570 thousand hexahedral cells was needed, where the height of the first wall adjacent cell is 1.1×10^{-5} m to ensure $y^+ = 1$. From the wall towards the center of the pipe, the cells are allowed to grow 20% from its previous size, up to about halfway between the wall and the center. After that the size remains constant. In Figure 8 a general overview of the mesh is presented. Note the high concentration of lines near the wall, indicating the presence of more cells.

Note that as all simulations presented in this chapter comprehend circular pipes, although in different orientations (horizontal and vertical), all computational meshes are constructed in very close way to the one presented here. Of course that as the pipe diameter

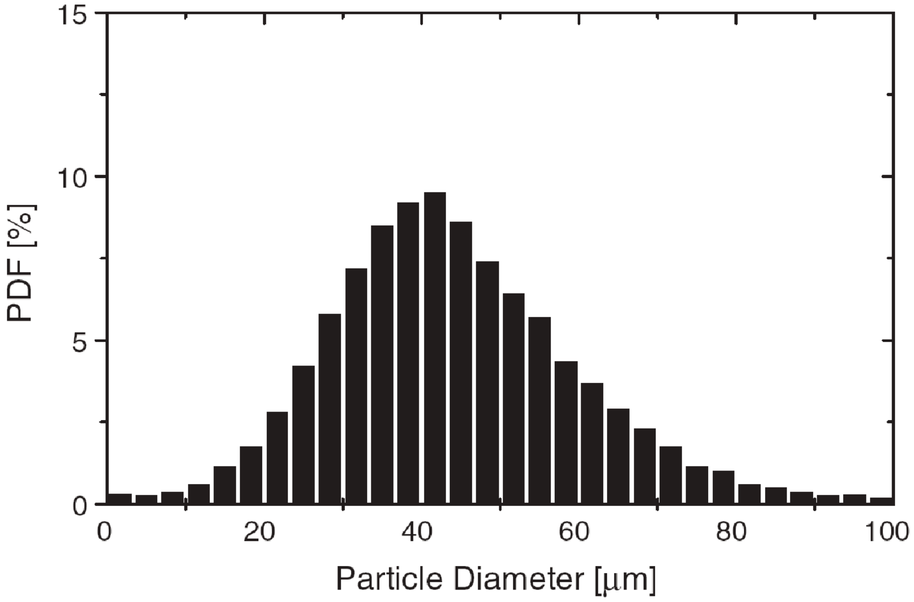

Figure 9 – Diameter distribution for the particles in the experiment of Huber and Sommerfeld (1998). Figure taken from Laín and Sommerfeld (2013).

and length changes, the cell count will also change. But the guidelines used to draw this mesh, in terms of ensuring $y^+ = 1$ at the wall, and grow ratio, are the same.

5.1.2 Simulation setup

The condition simulated from Huber and Sommerfeld (1998) is carried out at an average air velocity of 27 m/s with a particle mass loading $\eta = 0.7\,\mathrm{kg_{part.}/kg_{air}}$. Physical properties of the air were taken as $\rho_g = 1.2\,\mathrm{kg/m^3}$ and $\mu = 1.8{\times}10^{-5}\,\mathrm{kg/(m\,s)}$, and the particles' is $\rho_p = 2500\,\mathrm{kg/m^3}$. Note that the physical properties of the air will be the same for all simulations in the present thesis.

A diameter distribution is available for this case from Huber and Sommerfeld (1998) that will be used to ensure a better prediction and test the new implementation. The distribution is show in Figure 9. In the UNSCYFL3D code the distribution has to be accounted in a discrete manner, where to each discrete diameter a number of parcels are assigned. The effective distribution utilized in this case is presented in Table 1, where the continuous distribution was separated into seven diameters.

The parameters for particle-particle and particle-wall collision are taken to be the same as in Laín and Sommerfeld (2013), to allow for a direct comparison. For the particle-wall collision model, the wall roughness was taken as $\Delta\gamma = 10°$, meaning a very rough wall such as carbon-steel for instance, the static friction coefficient is 0.5, and the dynamic friction and restitution coefficients are functions of the impact angle (θ_{in}, in degrees), respectively:

$$f = \max\left(0.5 - \frac{0.35}{20}\theta_{in}, 0.15\right), \tag{5.1}$$

Table 1 – Diameter distribution for Huber and Sommerfeld (1998) case.

Diameter (µm)	No. of parcels
20	28
30	68
40	86
50	61
60	34
70	16
80	6

and

$$e = \max\left(1 - \frac{0.3}{22}\theta_{in}, 0.7\right). \tag{5.2}$$

These functions will provide a higher value of the coefficient at zero impact angle, initially. The value then decreases with the increase in the angle down to a minimum value, from where it remains constant. On the other hand, for the particle-particle collisions only constant values are utilized, 0.9 for the restitution coefficient and 0.4 for the friction coefficient.

In all simulations, present and future in this chapter, a time-step of 10^{-4} s was used for the fluid flow (Eulerian part) and 10^{-5} s for the particles (Lagrangian part). This different time-step is achieved by solving one step of the fluid flow, and then ten sub-steps of the particles before returning to the fluid flow. These values of time-steps are a common practice in many works from the group and also from other authors, and have been extensively shown to be enough to provide time-step size independent results.

5.1.3 Mesh size assessment

As the computational mesh presented in subsection 5.1.1 will be utilized as basis for all pipe flow simulations in the present thesis, it is important to assess its refinement independence to the results of both gas and particle phase. Note that for this evaluation, a one-way coupling with the k-ε model is utilized, because only the mesh size influence is important. The mesh previously presented is taken as the fine mesh and one with roughly 25% the number of cells is the coarse one.

The gas and particle phase velocities in the main flow direction are compared in Figure 10. Note that the plot is turned sideways to simulate the flow direction, with the gravity pointing downwards, and provide a better visualization. The influence of the mesh

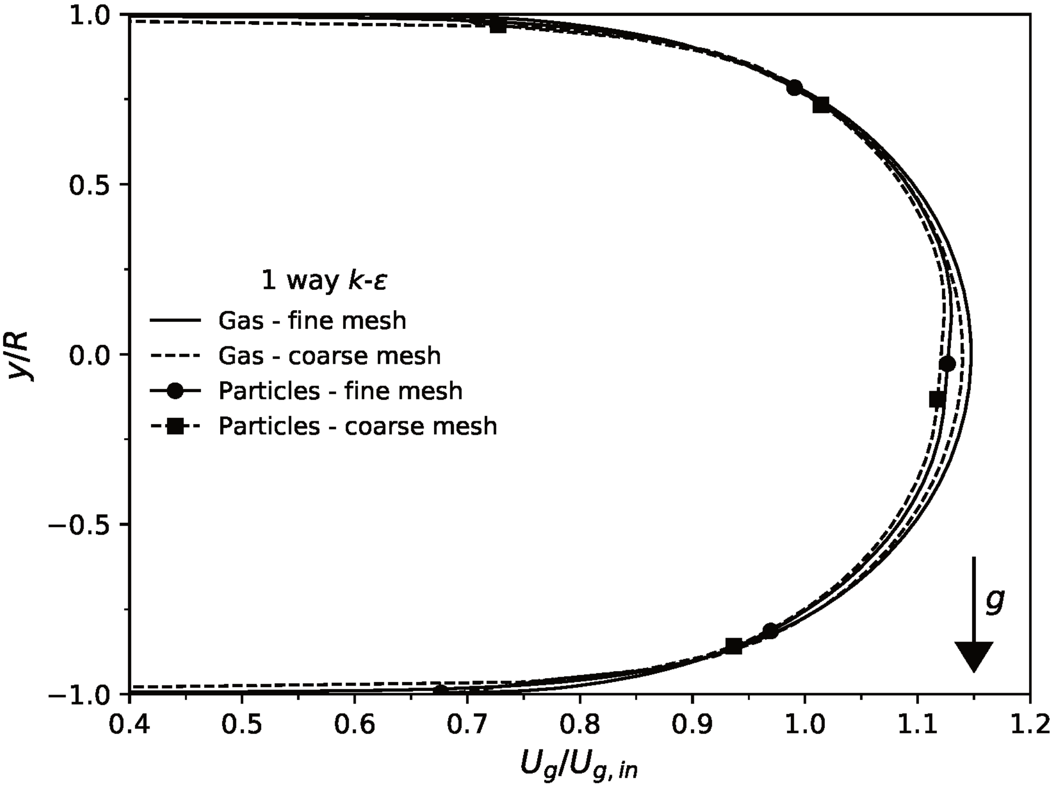

Figure 10 – Influence of the mesh size in the gas and particle phase velocity.

in the velocities is very small in both the center and in the near-wall region, although this near-wall region difference can be more important, because of the y^+ requirement.

In Figure 11 the particles diameter profile is presented, which also shows a very close matching at the central region, but a little more difference in the near-wall zone, probably because of the insufficient number of cells in this region. Overall, it is clear that the influence of the mesh is small for such different meshes, so that the fine one can be taken as suitable.

5.1.4 Validation and gas-particle coupling

To evaluate the validation of the model, comparisons for the particle phase average and fluctuation (RMS) velocity as well as diameter distribution are plotted against the experimental measurements from Huber and Sommerfeld (1998). Comparisons are also carried out assessing the influence of the gas-particle coupling – namely one, two and four-way coupling – and the turbulence closure model – k-ε and Reynolds Stress Model. The gas phase velocity was not available for comparison.

The particle average and RMS velocity profiles using the k-ε model is presented in Figure 12 in comparison to the experimental data assessing its agreement and the influence of the gas-particle coupling. Firstly, knowing that the four-way coupling should be the most physically accurate model, one can observe that a reasonably good agreement is achieved

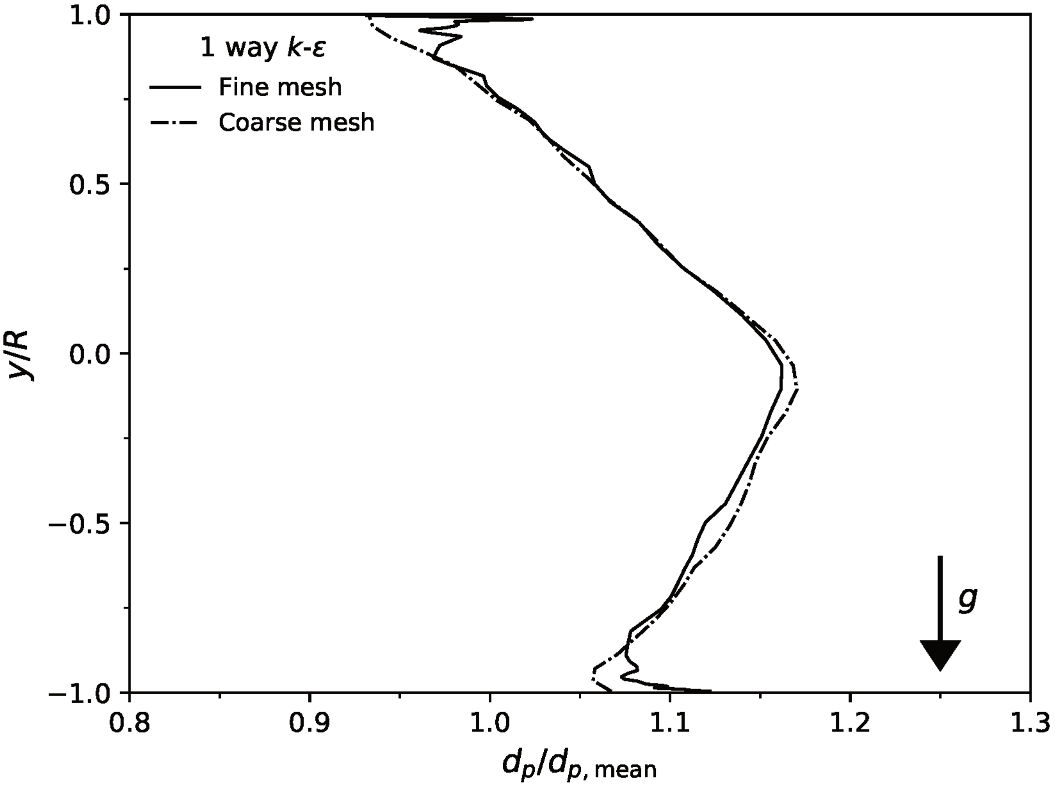

Figure 11 – Influence of the mesh size in the particle phase diameter distribution.

for the particle average velocity. There is some underprediction at the central region of the pipe and some overprediction towards the wall. The agreement to the fluctuation velocity profile is not so good, but it is known that the fluctuation variables are harder to predict, specially using an approach such as the present one.

It is interesting to also evaluate the influence of the gas-particle coupling on this profile. Although almost none difference is spotted in the fluctuation velocity, an odd behavior is shown in the average velocity. The profile using one-way coupling shows a close agreement to the four-way one and to the experimental data, but the two-way one presents an increase in the velocity at the top region while a decrease in the center to bottom one. This reduction is actually caused by the higher concentration of particles in this zone, that will "consume" momentum from the fluid. After the fluid gets slower in this region it will also make the particles slower. The one-way coupling obviously do not account for this since the fluid is frozen before the injection of the particles. The particles accumulate at this area because of the high wall roughness that make the particles rebound back up. The introduction of the particle-particle collisions (four-way coupling) makes the particle collide more at this region, due to the high concentration, and cause a redispersion that smooths out the velocity profile. This behavior is recurrent in horizontal pipe flows, and has also been previously shown in Prof. Sommerfeld's works and confirmed by some simulations using the UNSCYFL3D code.

In Figure 13 the particle diameter distribution profile is presented in comparison to

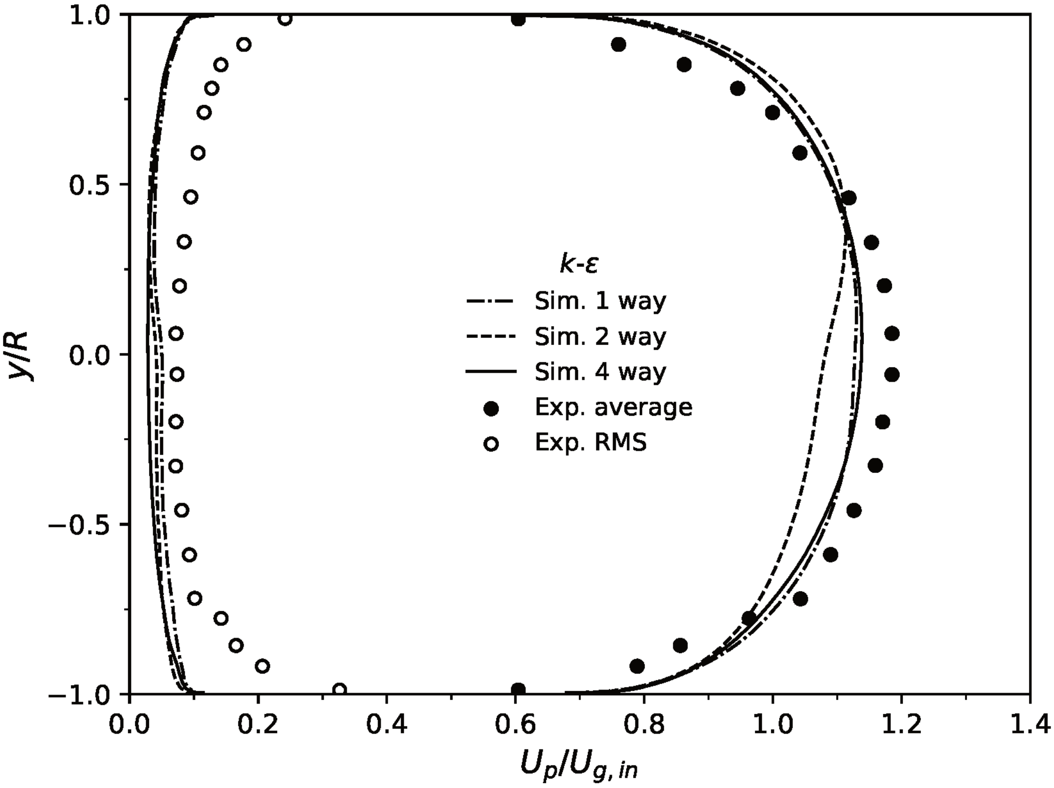

Figure 12 – Particle average and fluctuation (RMS) velocity profiles using the k-ε model with one-, two- and four-way coupling, in comparison to experimental data from Huber and Sommerfeld (1998).

the experimental data. Again, one can observe a reasonably good agreement of the four-way coupling profile, being able to closely predict all regions of the pipe. This profile shows that the distribution of the particles in pipe is not exactly monotonic, always increasing from top to bottom, as one would expect from gravity force alone. In fact, particle-wall and particle-particle collisions play important roles in the deposition, such that, aside from one point at the inferior wall, the higher diameters are actually halfway between the center of the pipe and the bottom wall. Note that the one- and two-way coupling were not able to correctly predict this, and showed the higher diameter region at the center of the pipe.

Simulations of this very same case were also carried out by Laín and Sommerfeld (2013) using the standard k-ε model with two- and four-way coupling, but were not drawn in the previous figures because the visualization would be hindered. The authors presented results that were very close to the present ones, and, therefore, had the same conclusions, which also helps to ensure that the present model is validated. Simulation from Laín and Sommerfeld (2013) had a slightly better agreement at the center of the pipe for both average and RMS velocities and similar at the walls. Regarding the diameter distribution, it was slightly better at the bottom wall, but slightly worse at the top.

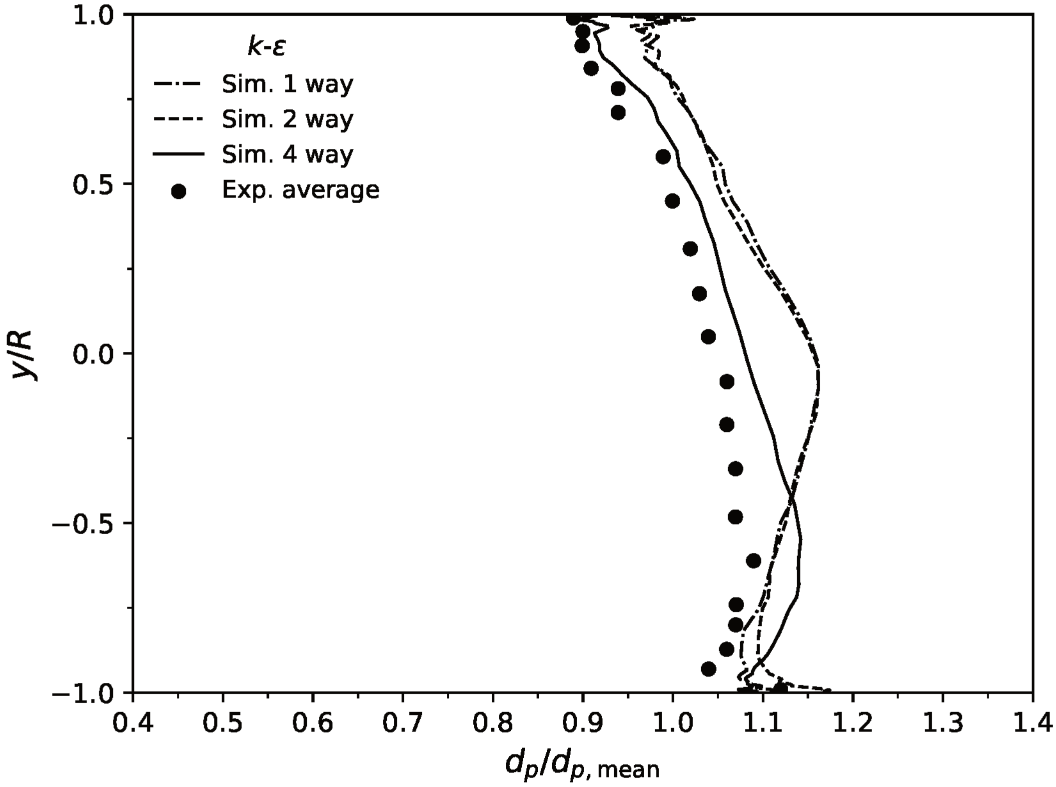

Figure 13 – Particle diameter distribution profile using the k-ε model with one-, two- and four-way coupling, in comparison to experimental data from Huber and Sommerfeld (1998).

5.1.5 Influence of turbulence model

An assessment of two different turbulence models was carried out to understand its influence on both gas and particle phases profiles, namely the two-layer k-ε model already presented in the mathematical modeling chapter, and the Reynolds Stress Model (WILCOX, 1993) that is also URANS based but uses one transport equation for each one of the six components of the turbulent Reynolds stress. The RSM is known to provide better results than two-equation models, but also comes with a more difficulty in convergence and sensibility to the mesh quality. For that reason, it is used herein more as a comparison to the limit of the model used at the present thesis.

Firstly, the gas velocity in a single-phase flow is presented for this case in Figure 14. Although there is no experimental data available, they can be compared to each other. The RSM model clearly predicts a higher velocity at the central region of the pipe, about 5% difference, but lower at the walls for mass conservation. At points very near the wall, almost no difference is noted.

The difference in gas velocity also causes a difference in the particle-phase velocity, as presented in Figure 15. The fluctuation velocity remains nearly the same but a considerable better agreement is achieved for the average velocity. In the central region the RSM predicts

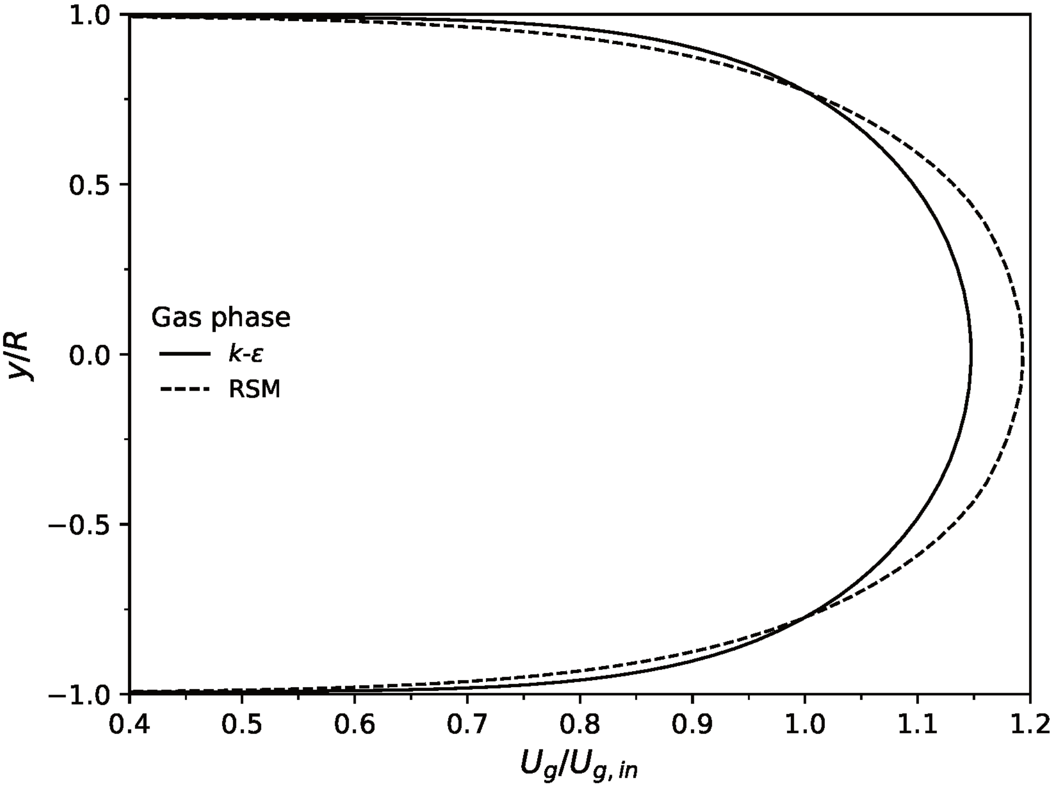

Figure 14 – Gas average velocity profile using the k-ε and RSM model in an unladen flow.

a higher velocity that ends up agreeing better with the experimental profile, which causes a lower velocity towards the wall that also agrees better than the two-layer k-φ.

Although difference was observed for the velocity profiles, in the diameter distribution profile presented in Figure 16 almost no change is noted. The only noticeable difference is at the top wall region where lower diameters are predicted by the RSM than by the two-layer k-ε. It is not possible to state if one is better than the other for the prediction of this variable.

Even though the RSM model provides better predictions for the variables analyzed here in comparison to the two-layer k-ε model, the latter is still suitable for particle-laden simulations, providing reasonable accuracy. Also, the RSM model takes much longer computational time to simulate, which is a core concern to the present thesis, and often presents convergence issues even in very fine quality mesh. For this reason, the two-layer k-ε model is continued to be used throughout the thesis.

5.2 Particle mass loading

In this section an evaluation of the influence of the particle mass loading on the flow will be carried out for two flow configurations, horizontal and vertical ascending. The choice of vertical ascending flow cases is not by chance, but because it shares a lot of characteristic

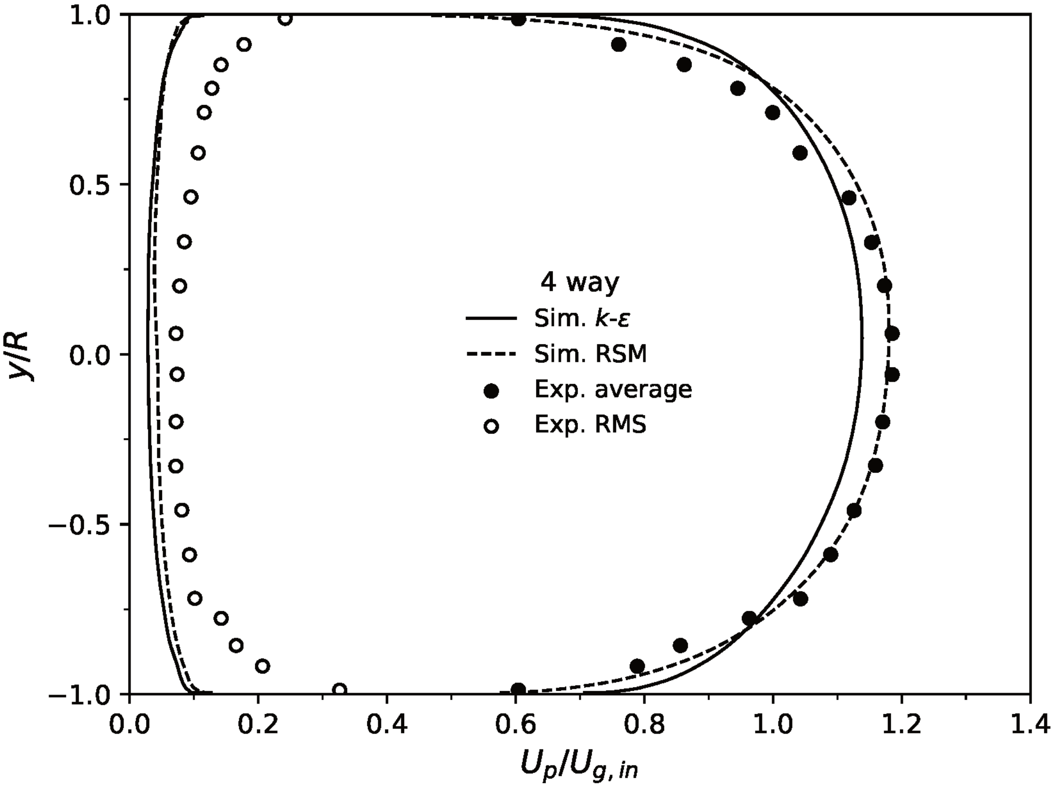

Figure 15 – Particle average and fluctuation (RMS) velocity profiles using the k-ε and RSM model with four-way coupling, in comparison to experimental data from Huber and Sommerfeld (1998).

with flows in risers. The UNSCYFL3D code had only been used for particle mass loadings of up to $\eta = 1.0\,\text{kg}_{\text{part.}}/\text{kg}_{\text{air}}$ so far, and that was in the riser simulations of Utzig (2016). In standard pipe and channel flow simulations the loadings were much lower. Simulations are carried out in order to better understand the limit of validity of this modeling.

5.2.1 Horizontal flow

For the horizontal flows study, four experiments performed by Tsuji and Morikawa (1982) were simulated for comparison. The experiments were all carried out using an air velocity of 15 m/s only changing the particle mass loading, namely: 0.4, 0.9, 2.2 and 2.8 $\text{kg}_{\text{part.}}/\text{kg}_{\text{air}}$. Also, all of them used the same particle diameter distribution with mean diameter $\overline{d_p} = 210\,\mu\text{m}$, shown in Figure 17, and $\rho_p = 1000\,\text{kg/m}^3$. Note that this diameter distribution has two peaks, one at 150 µm and another one at 275 µm, roughly. The experimental setup used by the authors is a circular pipe with 30.5 mm internal diameter and 3.56 m long, and the data acquisition was made at the end of the pipe in the vertical centerline.

The particles sizes were discretized into 14 values as presented in Table 2. All cases used the same setup for particle-wall and particle-particle collision parameters as the first case of this section. The pipe is made of a smooth material, so that its roughness is simulated with a wall roughness parameter of 0.5°.

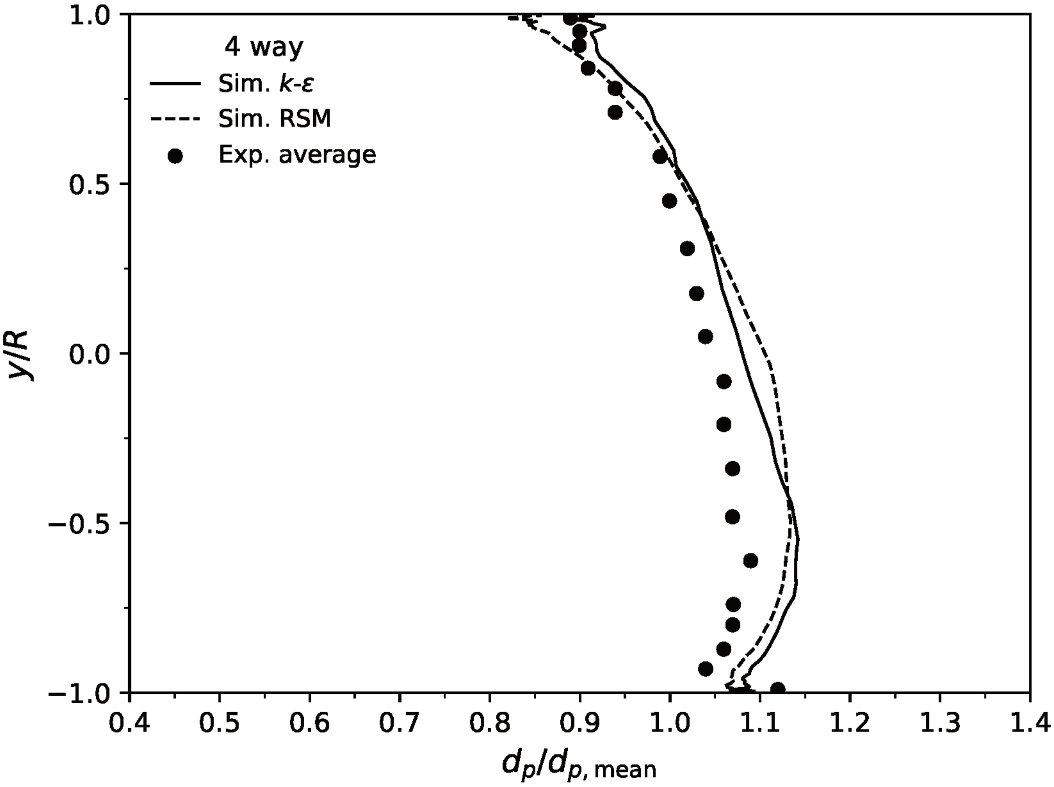

Figure 16 – Particle diameter distribution profile using the k-ε and RSM model with four-way coupling, in comparison to experimental data from Huber and Sommerfeld (1998).

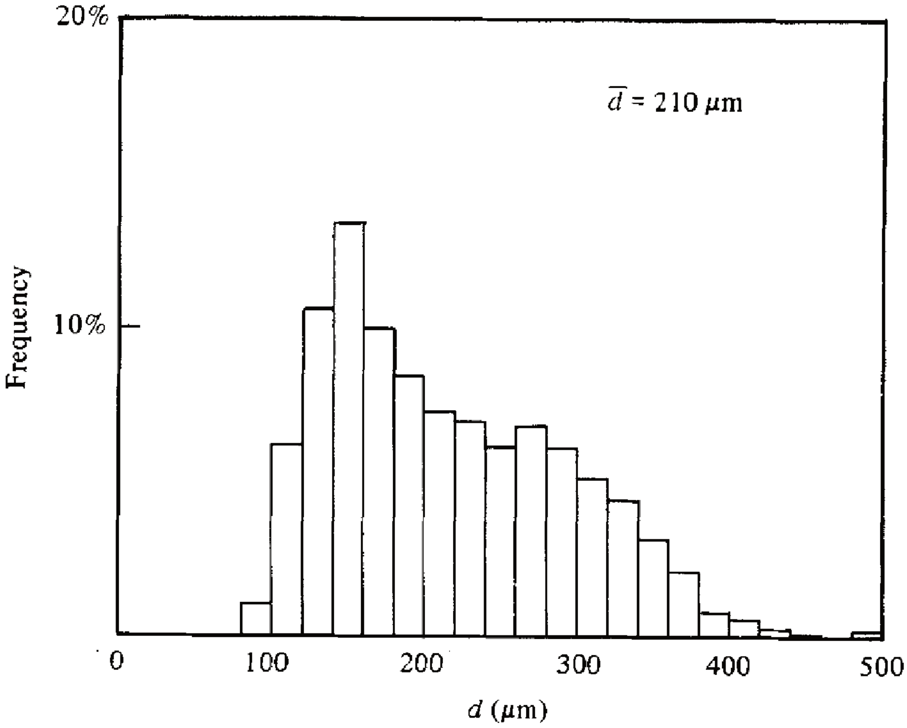

Figure 17 – Diameter distribution for the particles in the experiments of Tsuji and Morikawa (1982). Figure taken from Tsuji and Morikawa (1982).

Table 2 – Diameter distribution for Tsuji and Morikawa (1982) case.

Diameter (µm)	No. of parcels
110	2
130	3
150	3
170	3
190	2
210	2
230	2
250	2
270	2
290	2
310	1
330	1
350	1
370	1

5.2.1.1 Simulations

Figure 18 shows the fluid velocity profiles for all cases in order of increasing η. It can be noted that a very good agreement is achieved for particle mass loadings up to 0.9, which is consistent with previous simulations using this modeling. For $\eta = 0.4\,\mathrm{kg_{part.}/kg_{air}}$ all three gas-particle couplings provide similar results because the profile is still parabolic. At $\eta = 0.9\,\mathrm{kg_{part.}/kg_{air}}$ the profile is not parabolic anymore, showing a little of decrease in the velocity for the bottom region. This shows some discrepancy in relation to the one-way coupling, but the two- and four-way ones still provide reasonable accuracy. For $\eta = 2.2\,\mathrm{kg_{part.}/kg_{air}}$ the numerical profile starts to deviate more from the experiments, where the four-way coupling under-predicts the velocity un the upper region, but the two-way still provides some agreement. At the highest mass loading, there is no agreement with the profile anymore, although the order of magnitude of the velocity is right.

One can note that starting at $\eta = 2.2\,\mathrm{kg_{part.}/kg_{air}}$ a bi-modal experimental velocity profile is seen. One hypothesis is that the particle diameter distribution could be responsible for this, which has a nearly bi-modal distribution. If that is the case, the poor agreement from the simulation can be due to the particle-particle collision model, that is only statistical and can not account for this phenomenon, and only a deterministic one would be able to predict it. To the best of the author's knowledge, there is no particle-laden

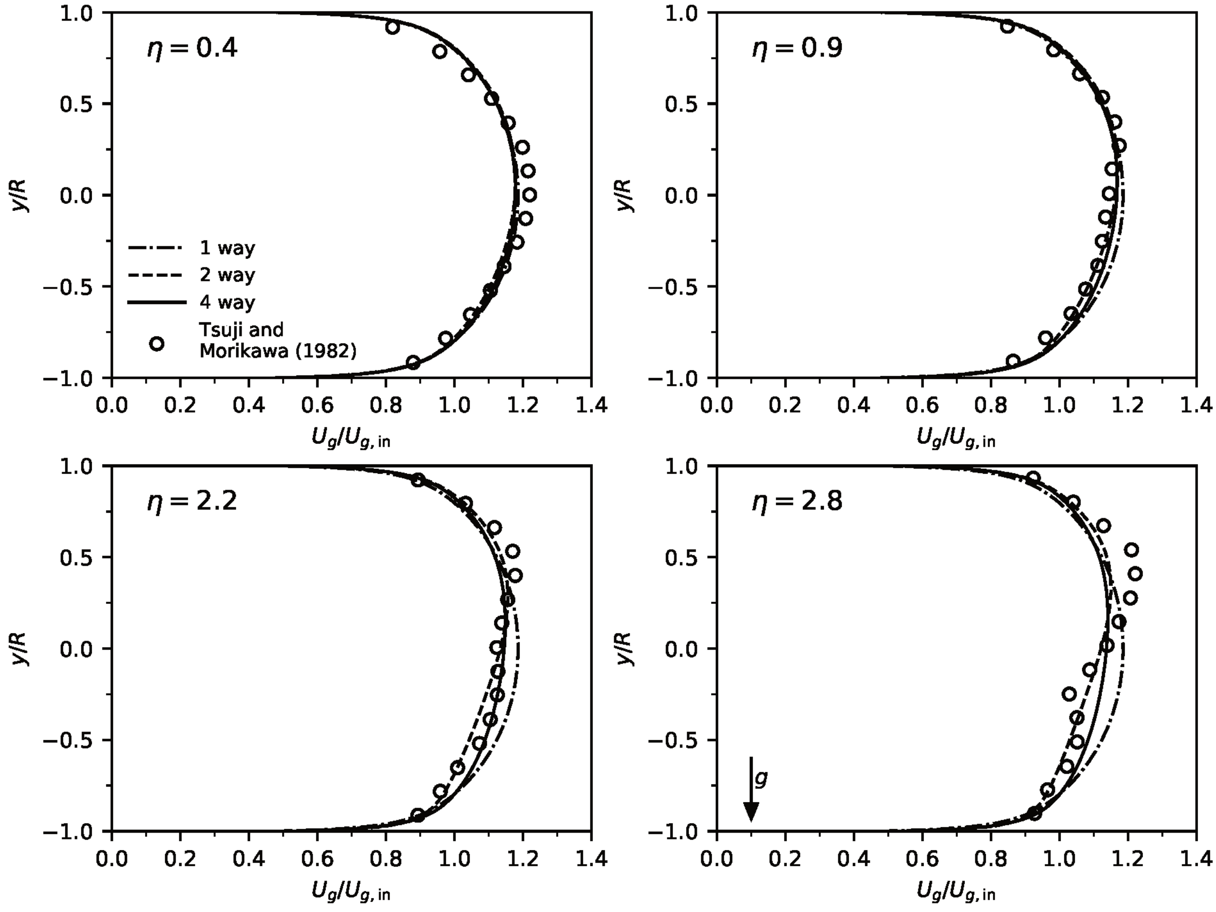

Figure 18 – Gas average velocity profiles using the k-ε model with one-, two- and four-way coupling, in comparison to experimental data from Tsuji and Morikawa (1982).

simulations demonstrating such phenomenon. However, other experiments of Tsuji and Morikawa (1982) with the same particle diameter distribution and high mass loading, but at a different fluid velocity do not show this characteristic. This does not refute the hypothesis, but only shows that a non-linear interaction of factors can exist.

Regarding the differences of the two and four-way coupling, one can note that either approach is valid up to $\eta = 0.9$. At higher mass loadings, the two-way coupling still keeps showing good qualitative behavior with a lower velocity at the lower region and higher at the upper region, but not matching the profiles exactly. This behavior is expected and shown also in the experiments, because the sedimentation of the solids in the lower region draws momentum from the fluid phase and induces its acceleration in the top. However, it seems that the four-way coupling almost do not capture this behavior in the last two cases. This occurs because of an excessive number of collisions that end up redistributing the particles in the pipe, as it will be better clarified by the particle concentration profiles. It is not clear if this is a limit reached by the collision model. One model that should help is introducing a collision efficiency into Sommerfeld's collision model as suggested by himself in Blei *et al.* (2002), which would reduce the number of collisions in polydisperse flows.

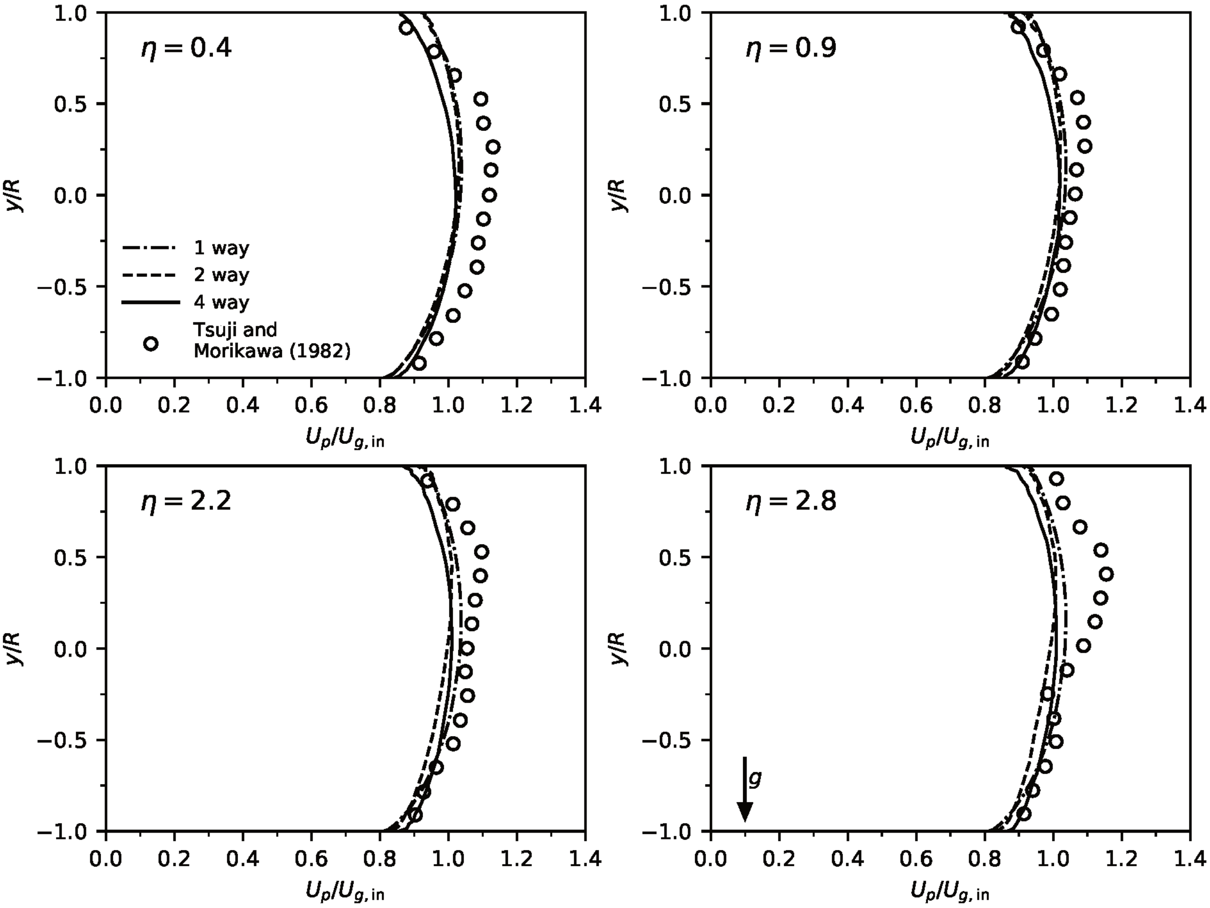

Figure 19 – Particle average velocity profiles using the k-ε model with one-, two- and four-way coupling, in comparison to experimental data from Tsuji and Morikawa (1982).

In Figure 19 the particle phase velocity is presented, also in order of increasing mass loading. Apart from some deviations in magnitude in the first case, one can state that good agreement is achieved up to $\eta = 2.2$. For $\eta = 2.8$ the agreement is weak and a very pronounced bi-modal profile is depicted. The trend of the four-way coupling to flatten the profile, in contrast to the two-way which presents lower velocity in the lower region and higher in the upper region, is also seen, but into a lesser extend that in the fluid velocity profiles.

The particle phase concentration profiles are shown in Figure 20. This figure is used to show how much more deposition is present in the one- and two-way couplings, which causes the momentum deficit in this region as shown before. However, as the collision are taken into account (four-way), much of the particles in this region migrate to the center and upper region, flattening the profiles.

All particle diameter distribution profiles are also compared, shown in Figure 21. Now one can observe that in all cases for one- and two-way coupling the bigger particles end up in the top region, while the small ones stay at the bottom. It is unclear if that is a

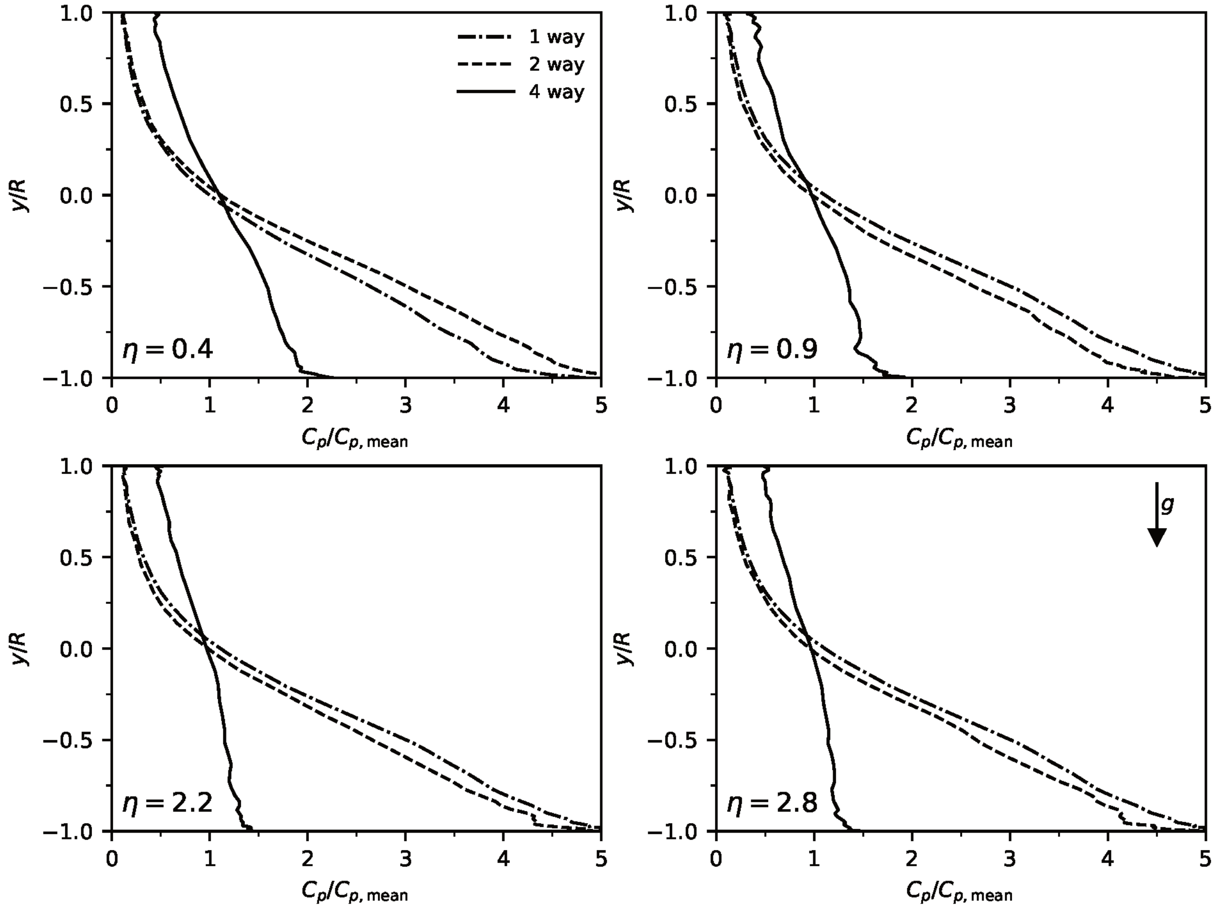

Figure 20 – Particle normalized concentration profiles using the k-ε model with one-, two- and four-way coupling, for the simulations of Tsuji and Morikawa (1982) cases.

physically possible scenario, because it has been shown in the first case of this chapter an experimental profile where the bigger particles were not more concentrated at the bottom wall, but nearer the center. Also note that in all four-way simulations this profile is either flattened or inverted.

5.2.2 Vertical ascending flow

In the vertical ascending flow study twelve simulations were carried out, six from Tsuji *et al.* (1984) and six from Mathisen *et al.* (2008). The experimental facility used by Tsuji *et al.* (1984) is a circular pipe with 30.5 mm internal diameter and 5.11 m long, where the data acquisitions were made at the end of the pipe in the horizontal centerline. And the facility from Mathisen *et al.* (2008) is a circular pipe with 42 mm internal diameter and 4 m long, but where the data acquisitions were made after the first 2 m in the horizontal centerline.

The selected cases from Tsuji *et al.* (1984) can be compared in pairs since there are two case at $\eta \approx 1\,\text{kg}_{\text{part.}}/\text{kg}_{\text{air}}$, two at $\eta \approx 2\,\text{kg}_{\text{part.}}/\text{kg}_{\text{air}}$, and two at $\eta \approx 4\,\text{kg}_{\text{part.}}/\text{kg}_{\text{air}}$. The difference is the particle diameter distribution and the velocity. Also the fluid velocity

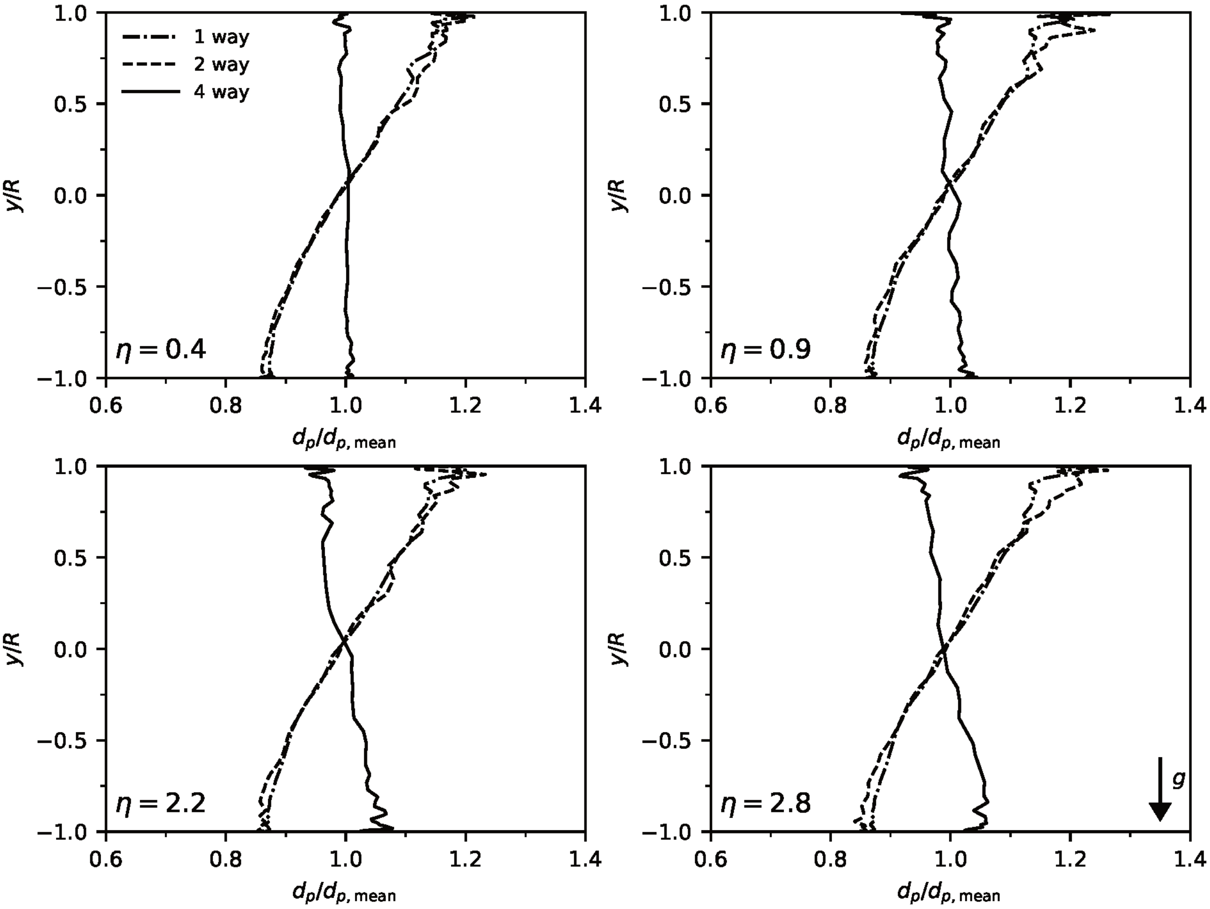

Figure 21 – Particle diameter distribution profiles using the k-ε model with one-, two- and four-way coupling, for the simulations of Tsuji and Morikawa (1982) cases.

is not the same for all cases because it was measured as an average during the experiment, due to how the control system was designed. In this work, they used two different particle distributions, one with mean diameter of 200 µm and one with 500 µm, both with $\rho_p = 1020\,\mathrm{kg/m^3}$. The continuous distribution was not provided, so only the mean diameter was utilized.

In the simulations from Mathisen *et al.* (2008), firstly two cases at the same η and diameter distribution were simulated, but with different inlet velocity. After that, the cases were performed in increasing order of particle mass loading, from $\eta = 3.1\,\mathrm{kg_{part.}/kg_{air}}$ up to $\eta = 7.9\,\mathrm{kg_{part.}/kg_{air}}$, keeping the same inlet velocity and roughly the same diameter distribution. They used two different sets of particles, one with mean diameter of 518 µm and $\rho_p = 2500\,\mathrm{kg/m^3}$, and another one with mean diameter of 530 µm and $\rho_p = 3800\,\mathrm{kg/m^3}$. The continuous distribution was also not provided, so again only the mean diameter was utilized.

Again, the cases used the same setup for particle-wall and particle-particle collision parameters as the first case of this section. In both studies the pipe is made of a smooth material, so that its roughness is simulated with a wall roughness parameter of 0.5°.

5.2.2.1 Simulations

The fluid phase velocity for the cases of Tsuji *et al.* (1984) are presented in Fig. 22, sorted column-wise by inlet velocity and particle diameter, and row-wise by particle mass loading. The one-way coupling provides good accuracy for the two first cases at the lower mass loading, but starts to fail from $\eta = 2.0\,\mathrm{kg_{part.}/kg_{air}}$ to the higher ones. This is in agreement with the horizontal flow findings. Regarding the two- and four-way coupling, one can note a good overall agreement in all cases. For the low mass loading cases there is a general small under-prediction of the center velocity, as the simulation profile is flatter than the experimental, but at medium loadings the agreement is very close. At higher loadings, the agreement is still good, but a slight difference is noted between two- and four-way coupling.

An interesting dynamics is seen at higher mass loadings where the point of maximum velocity may shift from the center towards a peripheral region, which is much more visible at the last plotted case (lower right). At this case it can be seen how the two-way coupling is able to predict the reduced center fluid velocity in comparison with its neighborhood in contrast to the four-way coupling that smoothed this effect showing a flat profile. This is exactly the same behavior shown in the horizontal flow, where the collision seem to excessively redistribute the concentrated particles. Although, here, this effect only appeared at a much higher particle mass loading.

The fluid phase velocity profiles for Mathisen *et al.* (2008) cases are depicted in Fig. 23. These authors do not provide data for comparison, however one can compare the simulations. Note that in all cases the one-way profile is more parabolic while the two- and four-way ones are more flat and very similar. As previously showed, for higher mass loadings the two-way coupling shows a shifting of the maximum velocity from the center, while the four-way coupling shows a flatter profile.

Note that for this case very high mass loadings are simulated, $\eta = 8\,\mathrm{kg_{part.}/kg_{air}}$ is roughly the loading of an industrial riser. However, in the present experiment as the particles enter all very well distributed and with a certain injection velocity, there is no great accumulation of solids as to form a cluster, and a dilute flow formulation is enough to provide good results since the volume fraction is kept small.

In Figure 24 the particle phase velocity profiles from Tsuji *et al.* (1984) are presented. Again the one-way coupling shows itself to be suitable only for low particle mass loadings, whereas the two- and four-way ones show an overall good agreement for all cases, only minor differences can be noted. Two-way coupling tends to show the same maximum velocity point shifting away form the center as it has shown in the fluid velocity profiles, while the four-way coupling showed the same flattening effect. These effects are much more light than for fluid velocity. One difference from the fluid velocity comparisons, is

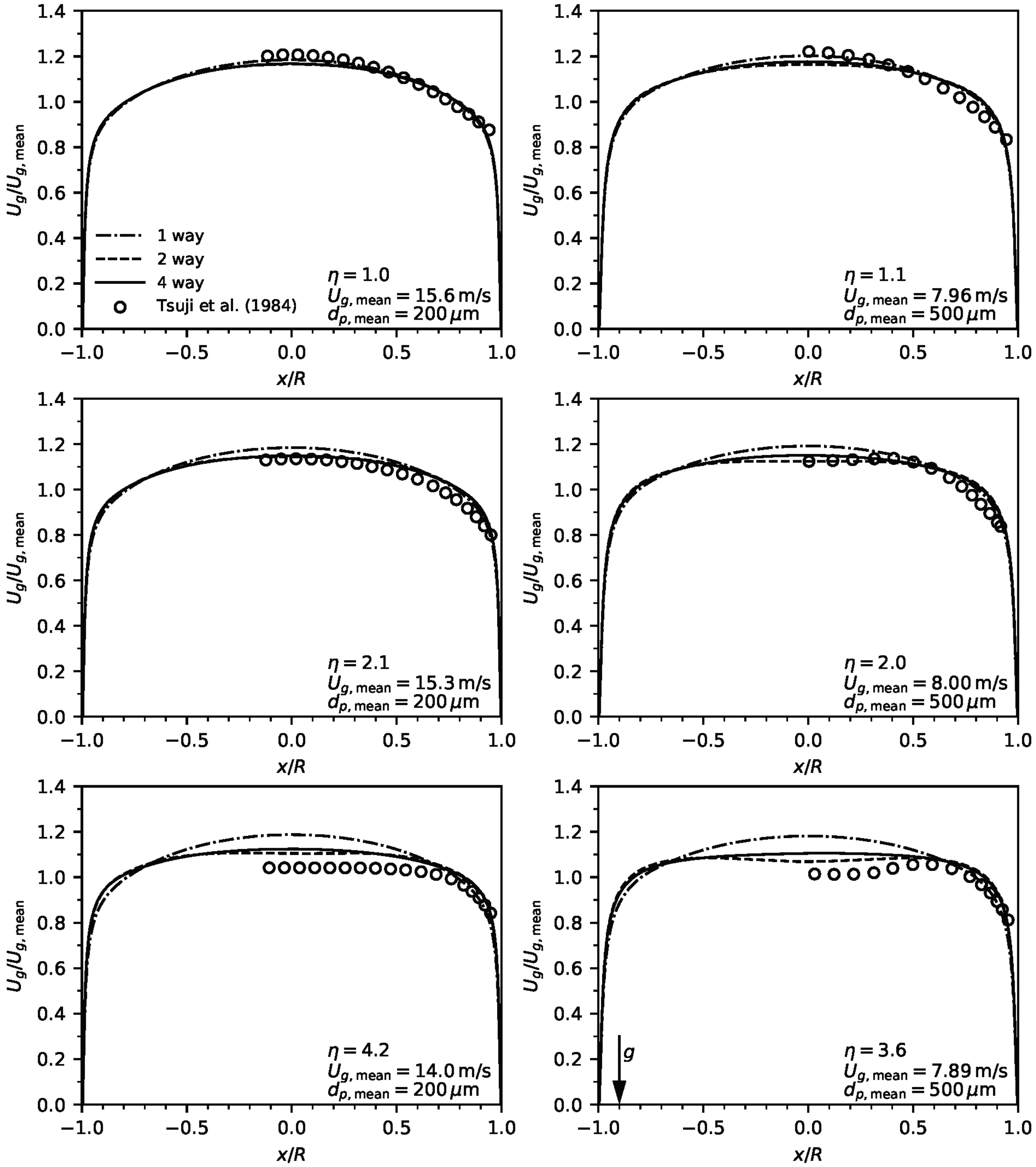

Figure 22 – Gas average velocity profiles using the k-ε model with one-, two- and four-way coupling, in comparison to experimental data from Tsuji *et al.* (1984).

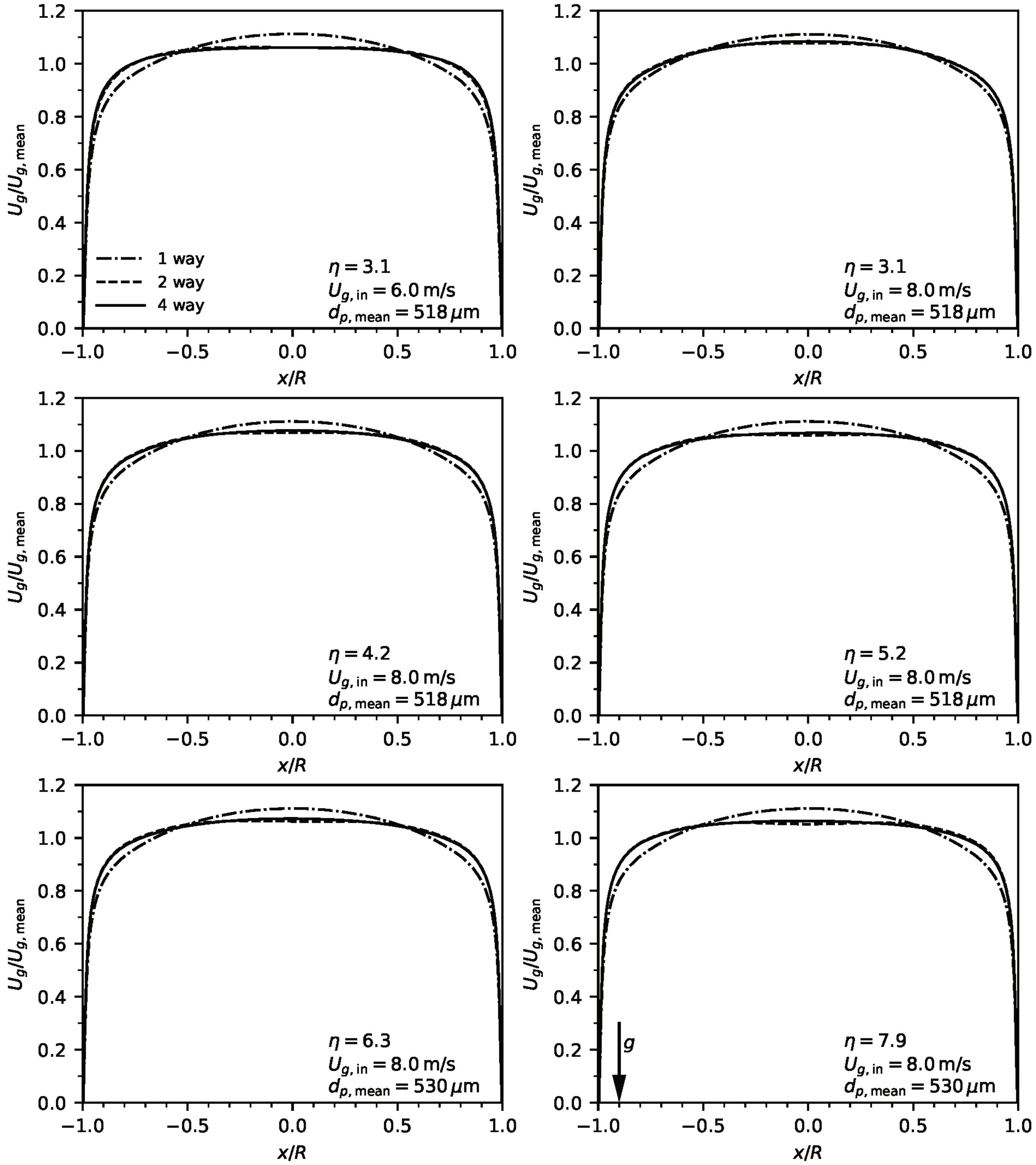

Figure 23 – Gas average velocity profiles using the k-ε model with one-, two- and four-way coupling, in comparison to experimental data from Mathisen *et al.* (2008).

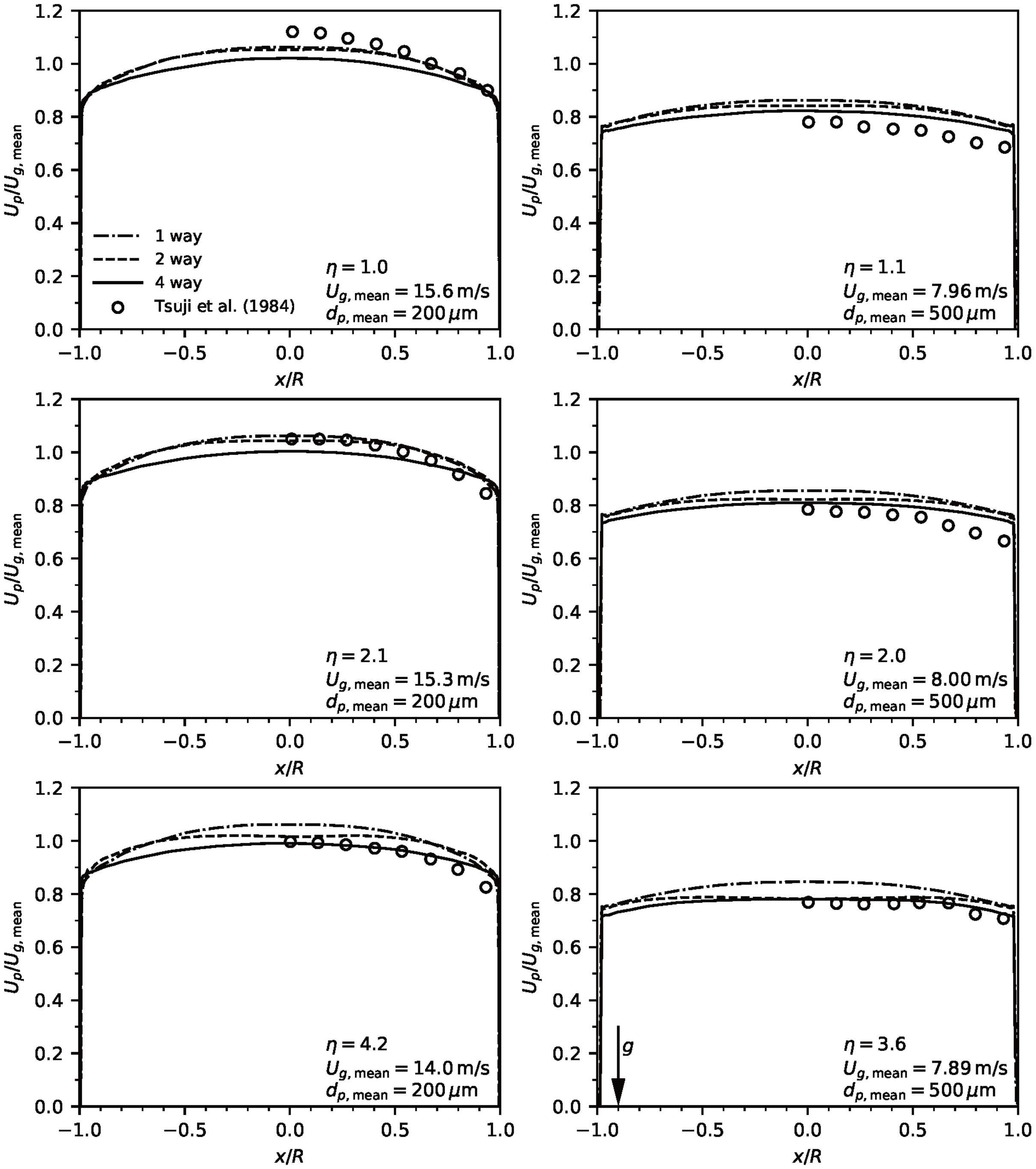

Figure 24 – Particle average velocity profiles using the k-ε model with one-, two- and four-way coupling, in comparison to experimental data from Tsuji *et al.* (1984).

that in this comparison the four-way coupling does show the decrease in velocity at the center point for the last case (lower right), and also it shows an overall better agreement than the two-way coupling.

Particle velocity profiles for the Mathisen *et al.* (2008) cases are presented in Figure 25. One can note that for this set of cases the particle velocities are much more flat than in the previous set. Also the numerical predictions are much alike to each other, and all also very flat, such that even a one-way coupling is able to reasonably predict

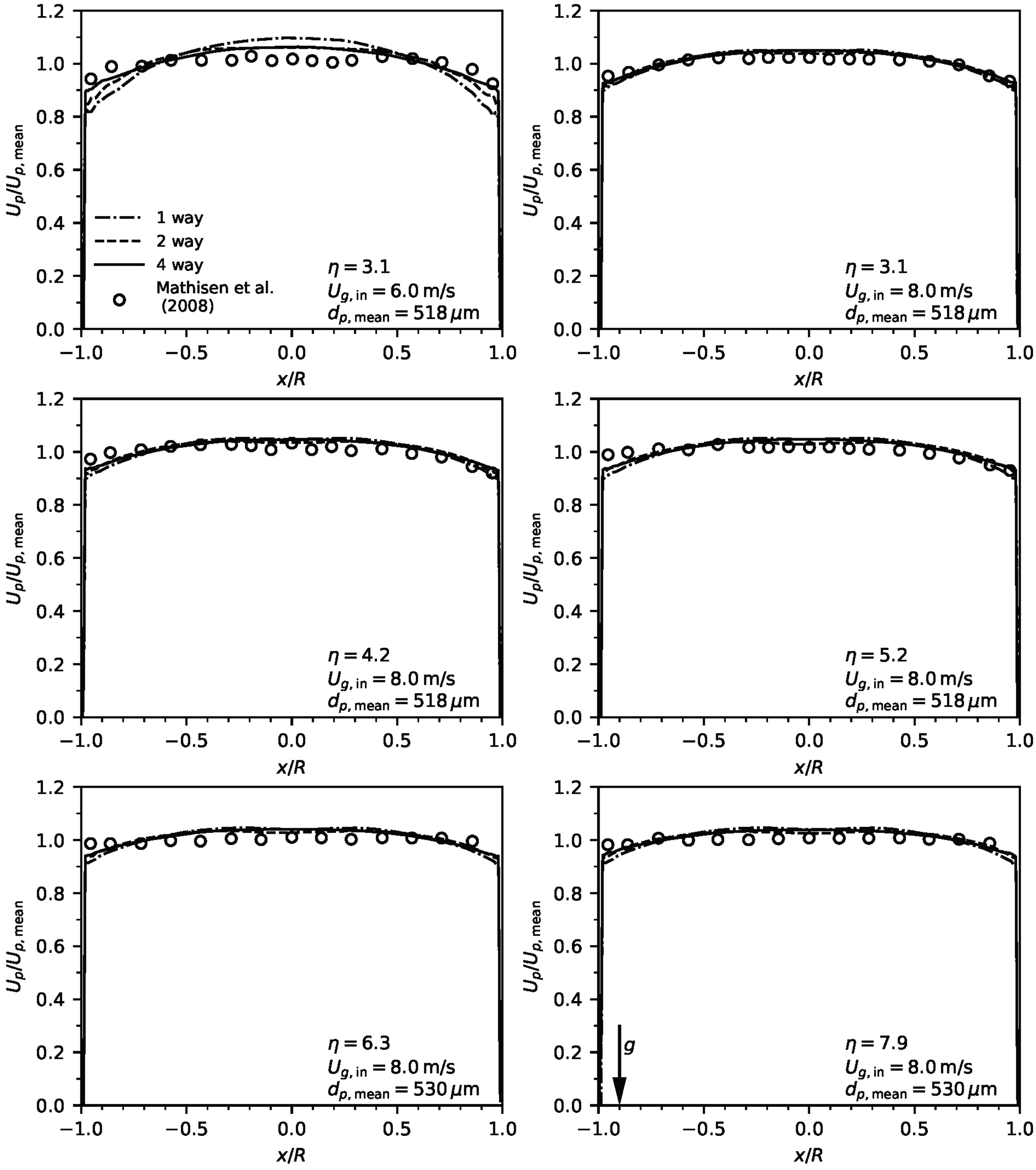

Figure 25 – Particle average velocity profiles using the k-ε model with one-, two- and four-way coupling, in comparison to experimental data from Mathisen *et al.* (2008).

the case at highest particle mass flow. This is attributed to the fact that in this vertical case the particles are very well distributed in the pipe section, creating no region of high concentration as is seen in the bottom region of the horizontal pipes or in the other vertical cases (shown next). Also, it is possible that the measurement of these experiments was carried out at a section where the flow was not yet fully developed, which would explain the profiles so flat and similar to each other.

The particle volume fraction profiles for the Tsuji *et al.* (1984) cases is presented in Figure 26. This figure supports the conclusions drawn before about the higher concentration of particles in the central region that draw momentum from the fluid and make the velocity to have a lower value at the center in some cases. Also, as already shown in the horizontal cases, one can note that the particle-particle collisions have the effect to redistribute the particles that are accumulated in the center to the peripheral regions. Another interesting fact is in the scale of the volume fraction. Although the lower left case has the highest particle mass loading, $\eta = 4.2\,\mathrm{kg_{part.}/kg_{air}}$, its volume fraction is still one order of magnitude lower that the second and third cases of the right column, at $\eta = 2.0\,\mathrm{kg_{part.}/kg_{air}}$ and $\eta = 3.6\,\mathrm{kg_{part.}/kg_{air}}$. This shows that the fluid velocity has a very important effect on the accumulation of particles inside the domain and the parameter η alone cannot be taken solely to define whether a flow will present features of a dilute or dense particle-laden flow.

On the other hand, in Figure 27 where the volume fraction profiles for the Mathisen *et al.* (2008) cases are shown, does not present any remarkable feature. Overall, one- and two-way coupling profiles show the expected increase in volume fraction at the center, but not nearly as pronounced as in the previous cases, and the four-way tend to flatten it a bit. Also, all cases fall into the order of 10^{-3}. These facts also point in the direction of a not yet fully developed flow.

5.3 Influence of forces and wall roughness

The roles of the fluid-particle forces and wall roughness are somewhat well-know in dilute particle-laden flows, but in order to gather some more insight about it and to check if the UNSCYFL3D code is able to provide such results, a simplified study is carried out herein. For this study, the first case from Mathisen *et al.* (2008), at $\eta = 3.1\,\mathrm{kg_{part.}/kg_{air}}$, $U_{g,\mathrm{in}} = 6.0\,\mathrm{m/s}$, $d_{p,\mathrm{mean}} = 518\,\mu\mathrm{m}$ and $\rho_p = 2500\,\mathrm{kg/m^3}$, is conducted using only one-way coupling. Although it has been shown that this coupling is not the ideal, it is enough to provide qualitative answers about the influences of each force.

Five cases are simulated for this case study: the first one is the standard case itself, that was already presented; the following one assess the effect of the shear lift force; the third one is removed from both shear and rotation lift; the fourth study assess the influence of the turbulent dispersion only, with all forces; and the last one evaluates the flow at a much higher wall roughness, $\Delta\gamma = 7.5°$, to clarify the difference in comparison to a smooth wall case.

Mando and Yin (2012) have also simulated this case from Mathisen *et al.* (2008), however did not present a very good agreement. In their simulation, the authors utilized an Euler-Lagrange approach with the standard k-ε model, one-way coupling, turbulent dispersion, and drag force, but neglected the lift forces (shear-induced and rotation-induced).

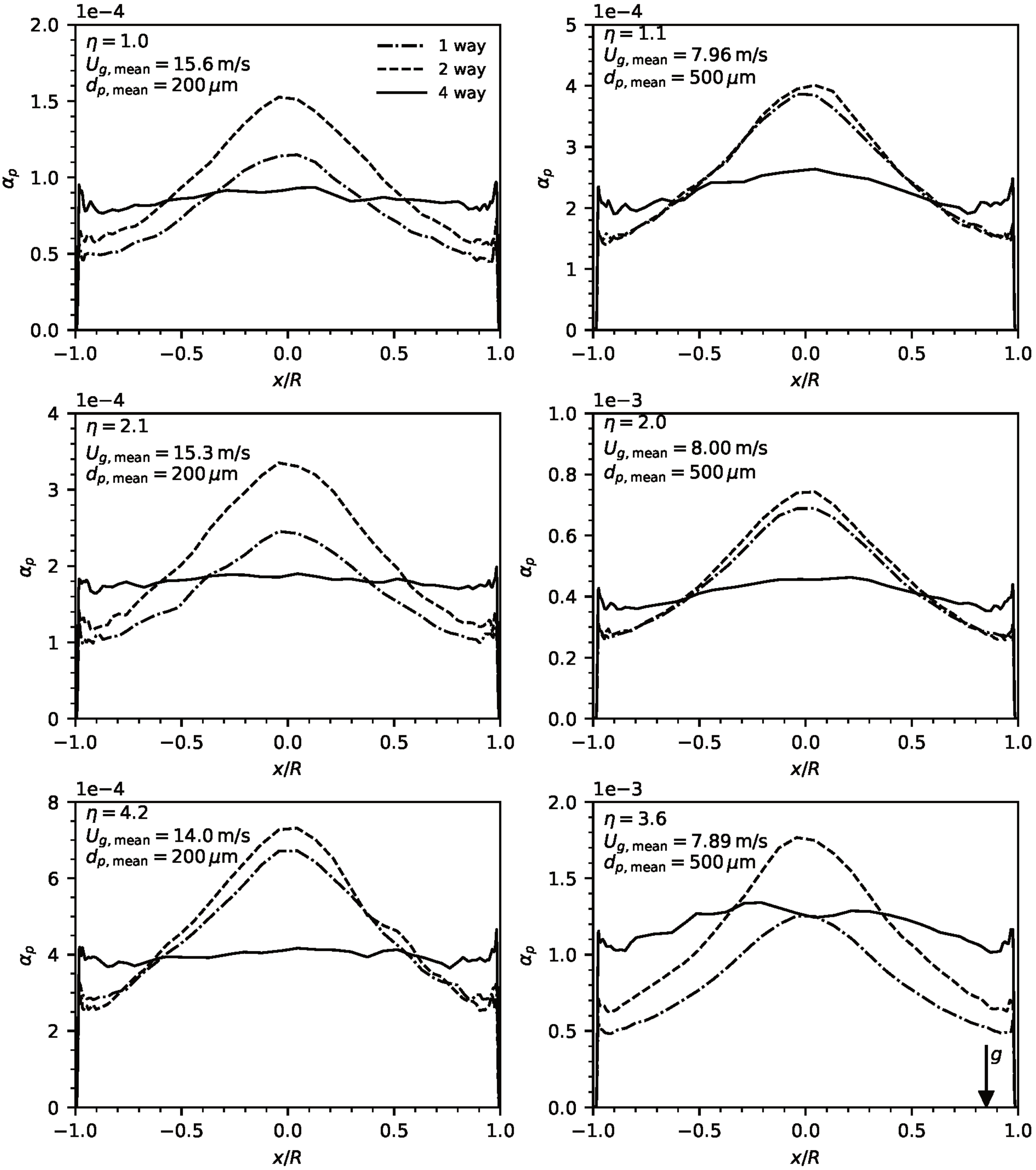

Figure 26 – Particle volume fraction profiles using the k-ε model with one-, two- and four-way coupling, for the simulations of Tsuji *et al.* (1984) cases.

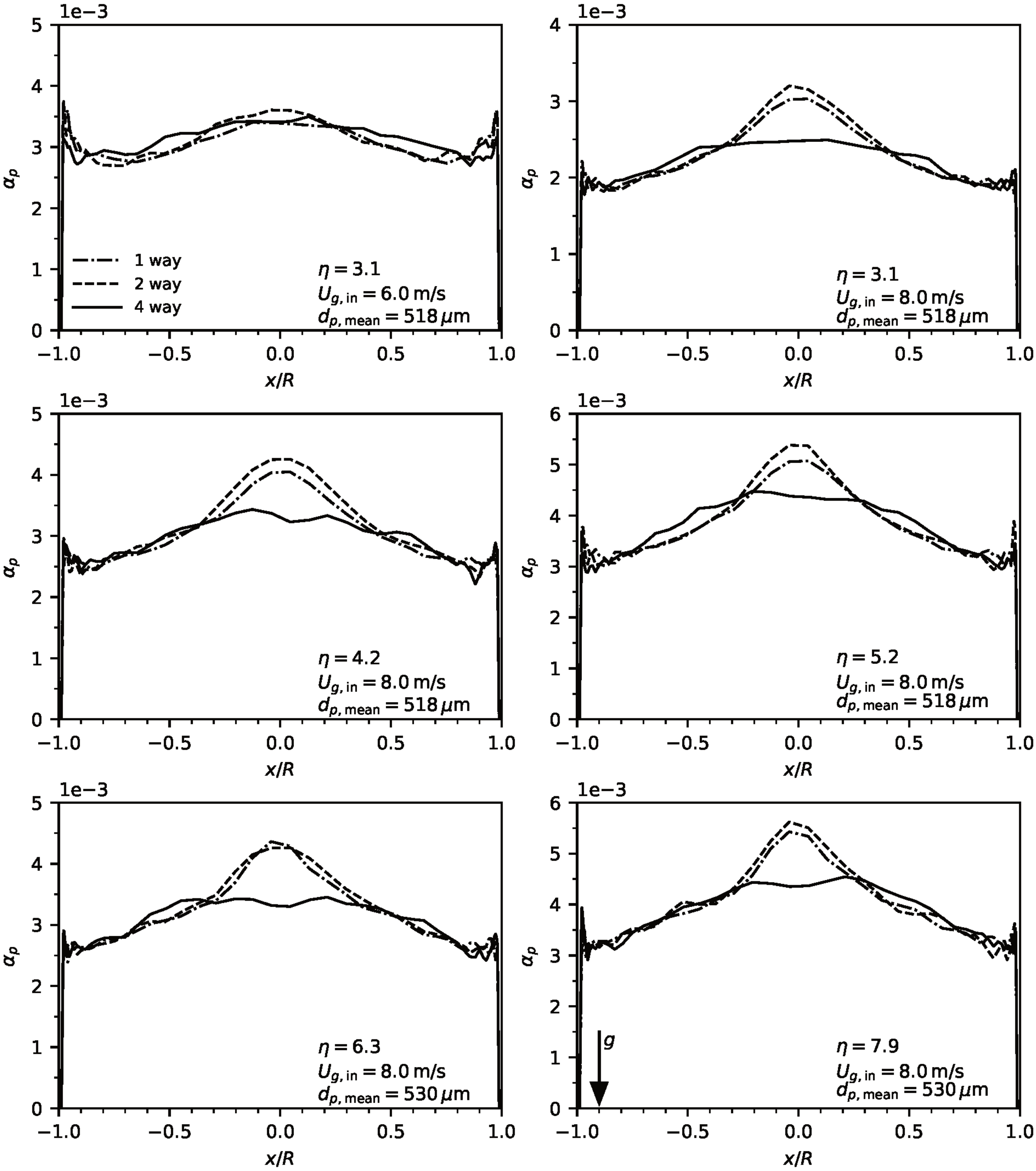

Figure 27 – Particle volume fraction profiles using the k-ε model with one-, two- and four-way coupling, for the simulations of Mathisen *et al.* (2008) cases.

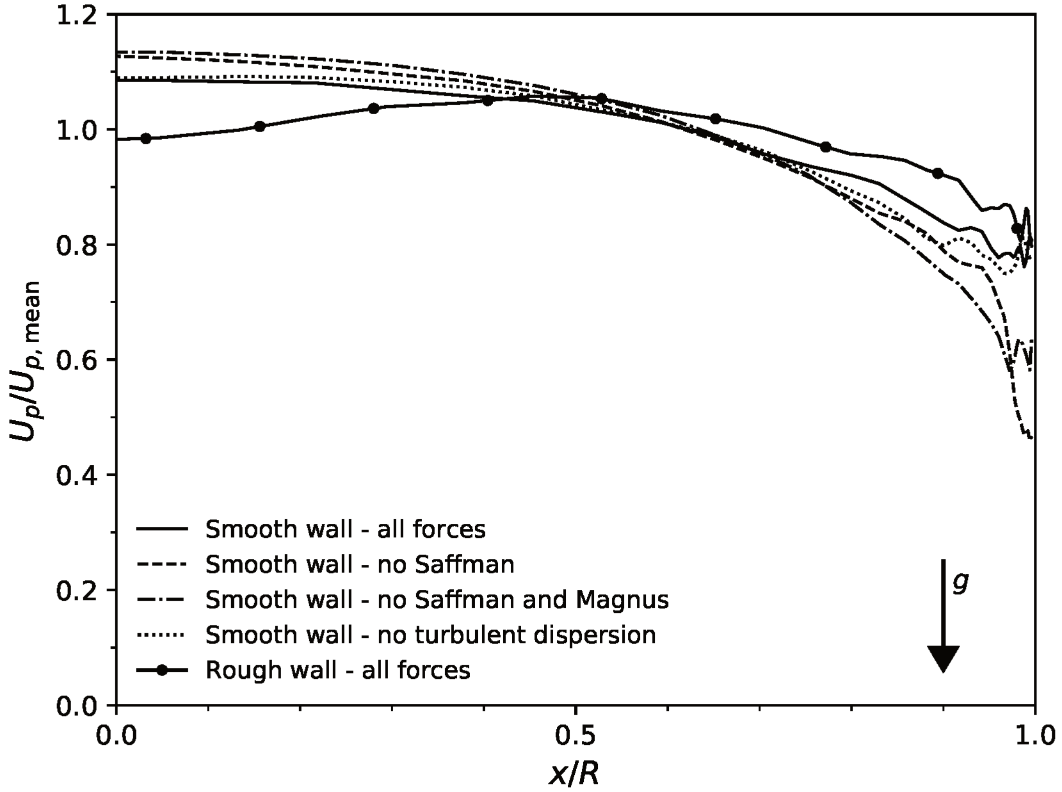

Figure 28 – Particle volume fraction profiles using the k-ε model with one-, two- and four-way coupling, for the simulations of Mathisen *et al.* (2008) cases.

They also evaluated the influence of the wall roughness.

5.3.1 Simulations

In Figure 28 the comparison of all particle velocity profiles is presented for one half of the pipe, as to provide a better comparative visualization. First of all, one notes that removing the shear lift force (Saffman) increases the center velocity a little while decreasing it largely at the wall. Further removing the second transversal force due to rotation (Magnus) just enhances the aforementioned effect, further increase in the center and decrease at the wall. On the other hand, it seems that the removal from turbulent dispersion has almost no effect in the profile. This finding was not expected and may be misleading because of the one-way coupling. It is necessary to investigate this effect under other couplings and mass loadings before drawing any conclusion, as the literature shows that the turbulent dispersion is indeed very important. At last, comparing a rough to a smooth wall shows that the roughness of the wall tend to decrease the center velocity while increasing it at the wall. The rough wall profile also reaches the previously discussed characteristic of higher velocity moved away from the center of the pipe. Note that this also shows that some minor tuning of the models in the previous simulations could have been done by changing the wall roughness parameter.

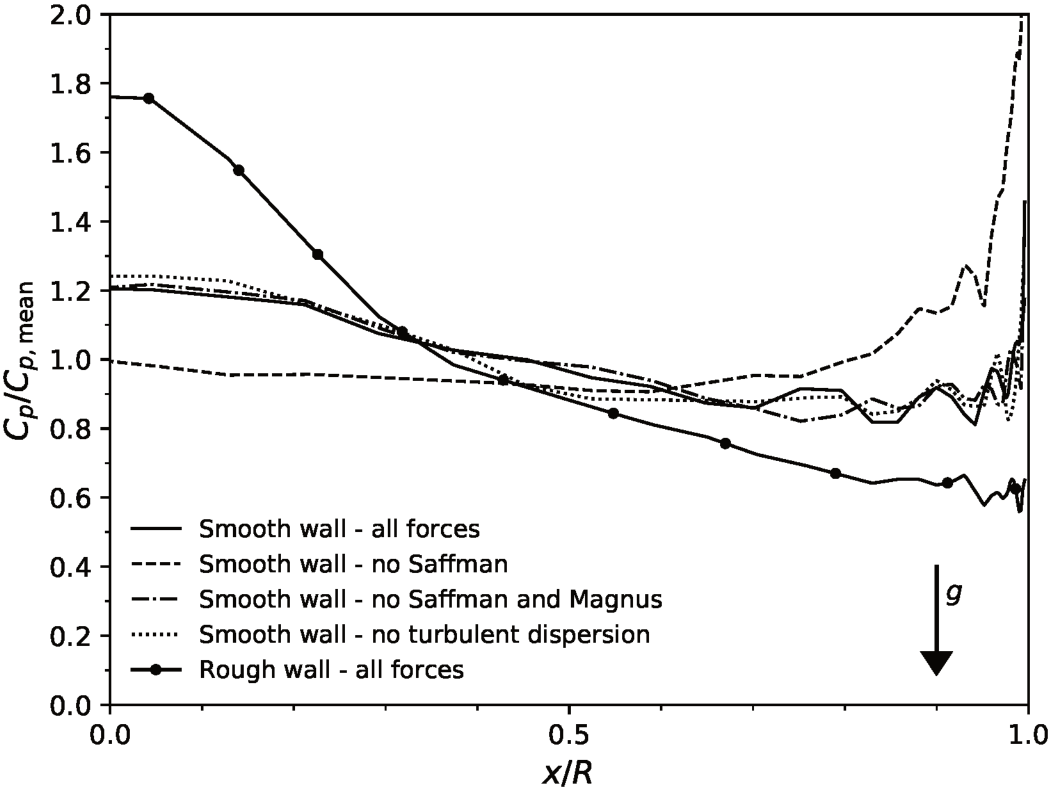

Figure 29 – Particle volume fraction profiles using the k-ε model with one-, two- and four-way coupling, for the simulations of Mathisen *et al.* (2008) cases.

It is important to note that the profiles neglecting the transversal lift forces presented in Figure 28, resemble Mando and Yin (2012) results that also neglected these forces. This result shows that even though the lift forces are small in magnitude, its transversal component is very important to a correct prediction of the flow characteristic in dilute particle-laden flows. The results from Mando and Yin (2012) for rough wall in comparison to a smooth one, also point in the same direction as concluded here, reduction of velocity at the center while increasing at the wall.

A great part of the modification seen in the previous profiles is due to a change in the particle volume fraction profiles, as presented in Figure 29. See for instance the effect of the removal of the Saffman force, the particles tend to move away from the center towards the wall, in comparison with the base case, which can directly explain the change in the particle velocity. However, further removing the Magnus force takes the particles back at the configuration of the base case. The mechanism here that causes this while changing the particle velocity is not clear. The turbulent dispersion has almost no effect, as in the particle velocity case. The wall roughness effect, is to rebound harder the particles away from the wall, causing the to accumulate in the central region and causing the effect seen in the particle velocity profile of velocity reduction.

5.4 Performance of the dense formulation in dilute flows

As a validation test for the dense formulation, but also as a test to compare the dense and dilute formulations, two cases from the present chapter were also simulated using the dense formulation. The first one the horizontal flow case from Tsuji and Morikawa (1982) at the higher mass loading, namely $\eta = 2.8\,\mathrm{kg_{part.}/kg_{air}}$, and the second one is the vertical case from Tsuji *et al.* (1984) that results in the highest volume fraction, namely $\eta = 3.6\,\mathrm{kg_{part.}/kg_{air}}$.

One could have noticed that, while the concentration profiles in the vertical cases were presented in terms of particle volume fraction, the horizontal cases were compared using a normalized particle concentration, even though the volume fraction is a better variable for comparison of concentration. This is because the horizontal simulations were carried out first, chronologically, and the calculation of the particle volume fraction was not available then. As this calculation was implemented during the course of the present thesis, now it is also a good time to provide at least an order of magnitude of the particle volume fraction for the horizontal cases. The resimulated case from Tsuji and Morikawa (1982) at $\eta = 2.8\,\mathrm{kg_{part.}/kg_{air}}$ presented the higher volume fraction value for two-way coupling at approximately $6{\times}10^{-3}$, which falls into the same order of magnitude as the volume fraction of the vertical cases.

Figures for the new particle phase velocities, particle volume fraction, and all other variables are not shown here because the results using the dense and dilute formulation were very similar, falling on top of each other when plotted together. It is reasonable that this would happen since both cases, horizontal and vertical, are at a very low value of particle volume fraction $\mathcal{O}(10^{-3})$. This shows that at least up to this order of magnitude of particle volume fraction, the dense formulation is not necessary, and also that the dense formulation is giving physical results at the limit of $\alpha_p \to 0$.

Chapter 6

Results and discussion: dense flows

In a similar fashion to the previous chapter, in this one simulations of dense flows in risers are carried out using the newly implemented dense formulation. As a means to show the importance of this formulation, comparisons are also made with the dilute formulation.

This chapter deals with simulations of particle-laden flows in risers at dense particle conditions. Firstly, in order to test the recent implementation of the mathematical formulation for dense flows in risers, a validation case is ran for comparison with both experiments and simulations utilizing other approaches. Following this validation, one case is isolated for a study of the influences from the mathematical model, adding and subtracting terms and forces. In the final part, the same riser, but at a lower particle mass loading is simulated with both dense and dilute formulation to point its differences. Also in this last cases the effect of the side inlet is evaluated.

Note that the comparison of formulations is carried out only at the end because of a numerical problem that will be detailed throughout this chapter, in which the convergence is impaired due to two factors: the first one is the transient term in the continuity equation (Equation 3.67); and the second one is the lack of a limiter for the gas-particle interaction force in very small cells. The side inlet was utilized only in these last simulations also because of this reason.

6.1 Validation for risers

As the dense flow formulation has just been implemented in the present thesis, in order to test it in risers a case study from Carlos Varas *et al.* (2017a), which carried out experiments and simulations in a pseudo-2D rectangular riser that mimics industrial ones, is simulated here. It mimics industrial risers in the sense that it is composed by a side inlet of particles that are carried upwards by the air flow and is separated at the top. More details are provided in the next subsection. This riser was also utilized in other studies of the group such as in Carlos Varas *et al.* (2016) and Carlos Varas *et al.* (2017b). This study was also chosen because it shows simulations using the LES+DEM approach, which is one of the most accurate models that one could utilize to simulate such cases, although it has a very high computational cost. It is interesting to evaluate the accuracy of the present thesis approach, which is very computationally cheap in comparison with the former.

In the present study, four simulations were carried out at four different gas inlet velocities that were also studied in Carlos Varas *et al.* (2017a) for comparison. The solids mass flux conditions are the same among the four cases. However, as in the present thesis we use the η to characterize the solids mass loading, which is a quantity that is calculated using the solids mass inlet over the gas mass inlet, the values will change.

6.1.1 Computational domain

The studied riser has a rectangular section of 70 × 6 mm and is 1.5 m height. At the top, a short radius curve leads to a cyclone separator that feed the solids back into a circular reservoir. The solids are fluidized at the reservoir to ease their injection back at the main riser, carried out by a small connecting rectangular channel. In this study, only the main riser is accounted for, and the separation and recirculation parts are not simulated. A simplified scheme of the riser showing its boundary conditions is presented in Figure 30.

Note, however, that in the present thesis the procedure utilized in the simulations of Carlos Varas *et al.* (2017a) is followed, where the solids are injected by the bottom of the riser together with the gas flow, using a small inlet velocity ($U_{p,\mathrm{in}} = 0.01$ m/s), instead of using the side inlet. It very important at this point to validate the model using the most precise information about the case, and the side inlet is not very well defined in the experiments, both in terms of geometry as in solids inlet velocity. Also, as their simulations utilize this very same approach, the comparisons should not be hindered.

The outlet curve in the cited study simulations is drawn very short, however in the present thesis it was decided to extend this exit geometry to avoid recirculation in this area. This recirculation can hinder the convergence of the fluid flow equations and also in extreme cases bring wrong results near this region.

Another important factor considered when chosen this case, is that the simulations from the mentioned authors are carried out using the LES approach for the gas phase, and a DEM approach to account for the particle collisions. The utilization of this combined approach leads to a very expensive computation, but also brings a good accuracy and

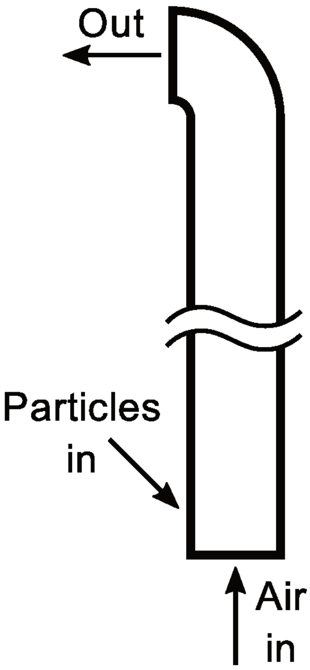

Figure 30 – Simplified scheme of the riser from Carlos Varas *et al.* (2017a) utilized in the simulations, and its boundary conditions.

physical representation. The comparison of this approach with the one followed in the present thesis, URANS for the gas and stochastic collision for the particles, which is very cheap in terms of computation, turns out to be a good test of its applicability.

The computational mesh was constructed using the same basis as stated in subsection 5.1.1, i.e. using a refinement in the near-wall regions to ensure $y^+ = 1$, with a growth ratio limited to 1.2. In the present case the construction of the mesh is very easy given that the geometry is rectangular and the hexahedral cells adapt perfectly to the geometry, with a perfect quality. With this, a total number of 312 thousand cells were needed to discretize the riser. In Figure 31, two details of the computational mesh are shown. The first is an overview of the main body and top curve mesh (left), and in the second one is a view of the cross-sectional area (right).

Note that the current mesh is much more refined that the much utilized in Carlos Varas *et al.* (2017a). In their study, the authors constructed a regular mesh with approximately 88 thousand cells, by discretizing the domain in a $28 \times 5 \times 628$ grid.

6.1.2 Simulation setup

Four conditions were studied in Carlos Varas *et al.* (2017a) and also in the present thesis, changing only the gas flow inlet velocity, namely: $U_{g,\mathrm{in}} = 6.74\,\mathrm{m/s}$; $U_{g,\mathrm{in}} = 6.35\,\mathrm{m/s}$; $U_{g,\mathrm{in}} = 5.95\,\mathrm{m/s}$; and $U_{g,\mathrm{in}} = 5.55\,\mathrm{m/s}$. The solids mass flux was defined as $32\,\mathrm{kg/(m^2\,s)}$ measured at the recirculation pipe. With and estimate of a 2 inches ID pipe, that would result in a total solid mass flow rate of $0.002\,\mathrm{kg/s}$. Given the particle density of $\rho_p =$

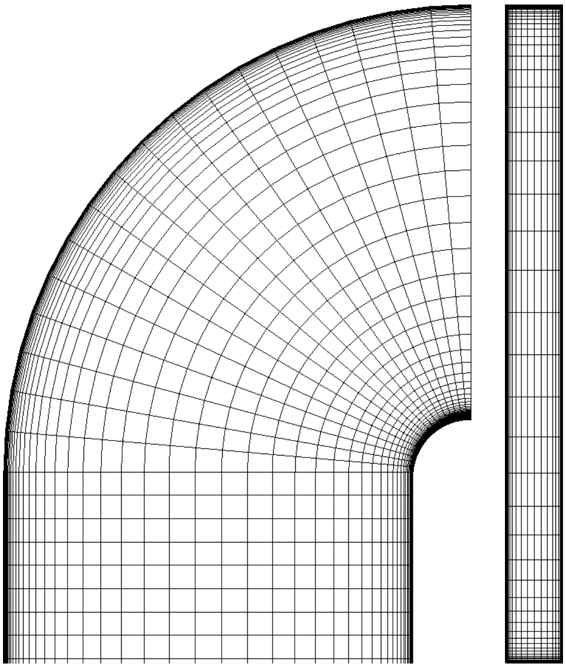

Figure 31 – Numerical grid for the riser: (left) lateral and (right) cross-sectional view.

$2500\,\mathrm{kg/m^3}$, the solids loading conditions are: $\eta = 19.1\,\mathrm{kg_{part.}/kg_{air}}$; $\eta = 20.3\,\mathrm{kg_{part.}/kg_{air}}$; $\eta = 21.6\,\mathrm{kg_{part.}/kg_{air}}$; and $\eta = 23.2\,\mathrm{kg_{part.}/kg_{air}}$.

The particles were characterized using only one diameter of 850 µm, and the number of real particles represented by each parcel is around 8. This represents a different view from the dilute cases were usually the number of real particles per parcel was smaller than one. The particle-wall collision parameters are defined in order to mimic the values utilized by the authors in their simulation, that means a wall roughness of $\Delta\gamma = 0.5°$, restitution coefficient of 0.86, and friction coefficient of 0.15. The particle-particle collision parameters were also defined in observation to Carlos Varas *et al.* (2017a), where the restitution coefficient is 0.96 and the friction coefficient is 0.33.

Regarding the time-steps utilized for both Eulerian and Lagrangian phase, the same approach as in the previous chapter simulations was followed. A larger time-step for the gas flow, $10^{-4}\,\mathrm{s}$, with ten sub-steps for the particles ($10^{-5}\,\mathrm{s}$).

6.1.3 Performance of the dilute formulation in dense flows

Let us start by assessing the performance of the dilute formulation on this chapter dense particle-laden cases before validating the dense formulation. Multiple attempts of simulation using the dilute formulation were tried at all four previously stated cases, but none of them succeeded. When trying it, at the very beginning the particles start to accumulate heavily at the bottom of the riser. The majority of the particles are never lifted by the gas flow. This continues to build up to a point where the solution diverges. Although the dilute approach have been previously utilized for the simulation of riser flows in Utzig (2016), it seems that at the present range of particle mass loading, which is much more dense than those in Utzig (2016), it is not suitable anymore and only the dense formulation is usable.

6.1.4 Validation

In Figures 32, 33, 34 and 35, plots of the local particle volume fraction for three different heights - 0.8, 1.1 and 1.4 m above the inlet of the riser - are shown comparing the present thesis simulations, and the simulations and experiments from Carlos Varas *et al.* (2017a). Each figure presents a different condition as stated in subsection 6.1.2.

Firstly, in Figure 32 the condition at $U_{g,\text{in}} = 6.74\,\text{m/s}$ and $\eta = 19.1\,\text{kg}_{\text{part.}}/\text{kg}_{\text{air}}$ is presented. In an overall overview of all heights, the presents work's simulation is able to yield a good representation of the volume fraction profiles. In all three heights the order of magnitude of the variable is captured, although some room for improvement can be seen especially in the lateral distribution of the particles. At 0.8 m, our simulation predicted a little bit more concentration on the center and failed to get the representation of some accumulation in the right wall. Note, however, that this underprediction in the right wall was also shown by the simulations of Carlos Varas *et al.* (2017a) and it is likely due to the bottom inlet of the particles, instead of the side inlet which would have sent the particles to the opposite wall. At the 1.1 m height, a good representation is achieved, in both central and wall regions. At the topmost location, the k-ε + stochastic collision simulation correctly predicts the lower accumulation at the left wall and the flat profile at the center region, but doesn't predicts the increase in the right wall, which Carlos Varas *et al.* (2017a) claims is due to the exit geometry.

In the second condition, at $U_{g,\text{in}} = 6.35\,\text{m/s}$ and $\eta = 20.3\,\text{kg}_{\text{part.}}/\text{kg}_{\text{air}}$ presented in Figure 33, an overall good agreement is also shown. At 0.8 m height, the wall region predictions is close to the reported values, although it shows a different dynamics from the center to the right wall. While in Carlos Varas *et al.* (2017a) experiment and simulation an accumulation only very near the right wall is noticed, in the present simulation the accumulation starts near the center and stands up to the the wall. At the center location measurement a reasonably good agreement is achieved for all regions, showing the increase in accumulation from the left to right wall. At the top, 1.4 m height, also a good agreement is shown, where the characteristic of the profile is very close to the other reported profiles, but with a minor overprediction.

Figure 34 shows the results for the third condition, at $U_{g,\text{in}} = 5.95\,\text{m/s}$ and $\eta = 21.6\,\text{kg}_{\text{part.}}/\text{kg}_{\text{air}}$. At this condition, the order of magnitude of the particle volume fraction is still correctly predicted at all heights, however, the present thesis simulations start to display some more difference in the predictions. In the 0.8 m height measurement, the reported profile from Carlos Varas *et al.* (2017a) shows two regions of accumulation at the two walls, and a lower concentration region in the center. On the other hand, in the

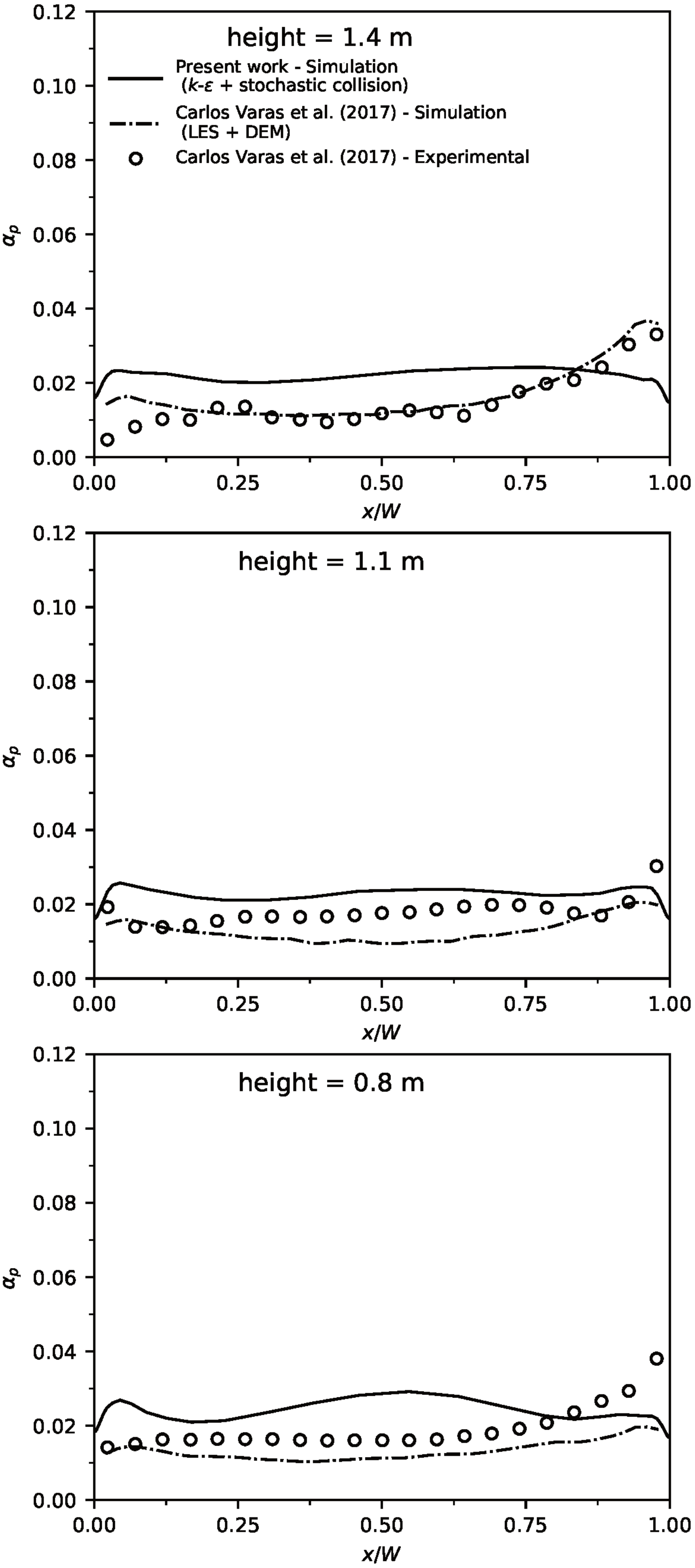

Figure 32 – Particle volume fraction profiles in comparison to the simulation and experiment of Carlos Varas *et al.* (2017a) at three heights: 0.8, 1.1 and 1.4 m above the inlet. Condition: $U_{g,\mathrm{in}} = 6.74\,\mathrm{m/s}$ and $\eta = 19.1\,\mathrm{kg_{part.}/kg_{air}}$.

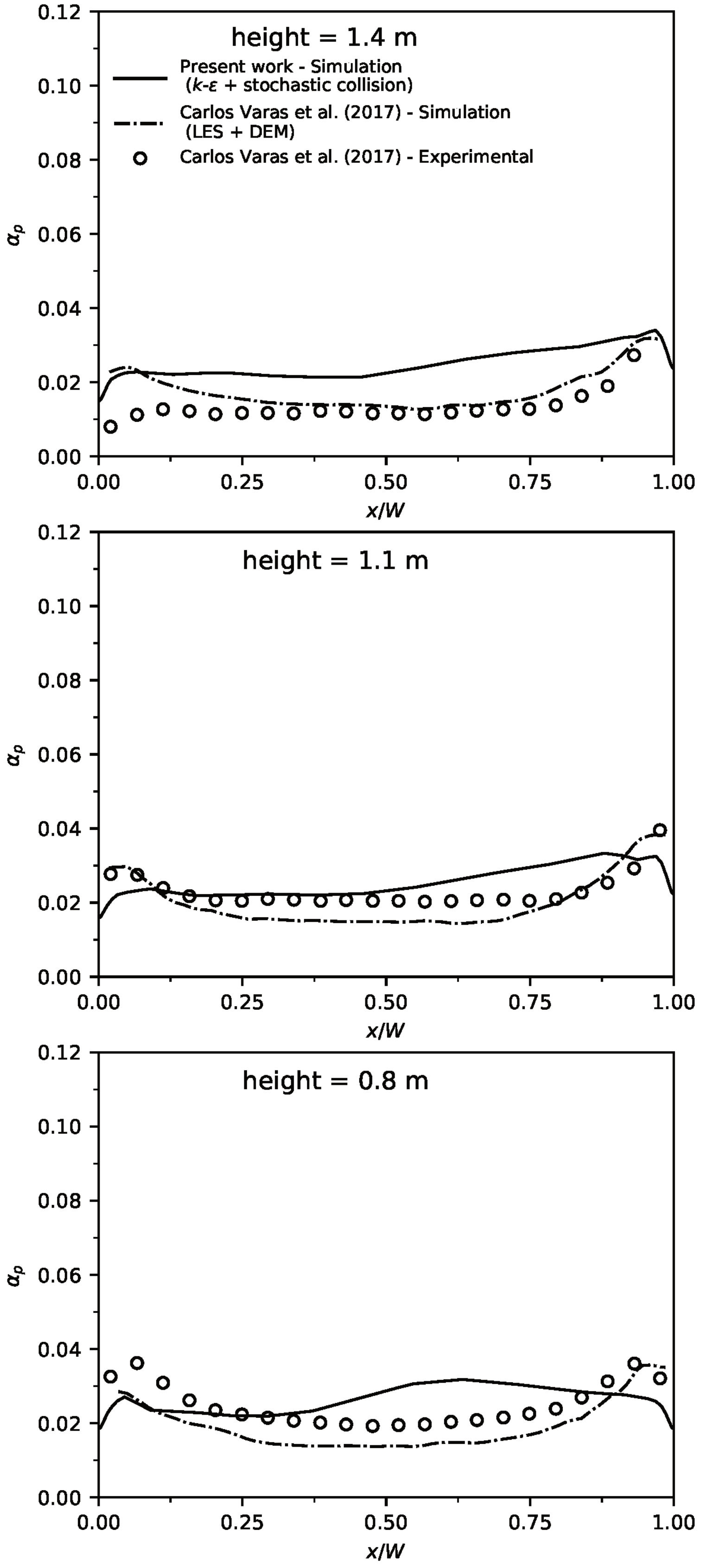

Figure 33 – Particle volume fraction profiles in comparison to the simulation and experiment of Carlos Varas *et al.* (2017a) at three heights: 0.8, 1.1 and 1.4 m above the inlet. Condition: $U_{g,\mathrm{in}} = 6.35\,\mathrm{m/s}$ and $\eta = 20.3\,\mathrm{kg}_{\mathrm{part.}}/\mathrm{kg}_{\mathrm{air}}$.

present thesis simulation this behavior is not correctly reproduced, as it shows a decrease of concentration on the walls and an increase near the center-right region. Now, at the middle and top measurements, the predictions are still good, correctly predicting the increased particle accumulation in the right wall and lower at the center. An underprediction is still present at the 1.1 m profile at the left wall.

In the last studied case, shown in Figure 35 at the condition $U_{g,\text{in}} = 5.55\,\text{m/s}$ and $\eta = 23.2\,\text{kg}_{\text{part.}}/\text{kg}_{\text{air}}$, the predictions from the present thesis simulations get worse. Note that the overall qualitative mean value of the particle volume fraction is still reasonable, but the profiles are off. All three profiles from Carlos Varas *et al.* (2017a) report an increased concentration of particles at the the walls while the center shows a lower accumulation, but none simulation of ours showed such characteristic.

In Figure 36 the axial profiles of particle volume fraction are presented, which were calculated by taking the average of the variable in planes at many heights. This figure also presents the present thesis simulations in comparison the ones from Carlos Varas *et al.* (2017a) and its experiments, for all four studied cases. One notes that the observations drawn from the previous figures are also valid and represented here. In the first (top left) and second (top right) cases, an overall good agreement is shown between the k-ε + stochastic collision simulations and the experiments for all the riser. It even shows a better prediction than the LES + DEM simulation, except at the top region. However, in the third case (bottom left) the prediction starts to show some discrepancies, but is still reasonable. The shape is similar but with a different slope, which causes a bit underprediction at the bottom to center regions, and a bit overprediction at the top. In the last condition (bottom right) the simulation shows no more agreement with the experiment.

Note that as the gas velocity decreases, the overall accumulation of particles inside the riser will increase due to the lower drag force. This higher accumulation will also increase the occurrence of particle clusters as shown in Carlos Varas *et al.* (2017a). It is reasonable to suppose that the present thesis approach fails more in these more dense conditions due to exactly this higher accumulation of solids. Although there may be factors to improve the predictions, such as the particles side inlet geometry, they were also not considered in Carlos Varas *et al.* (2017a) simulations, which have presented reasonably good accuracy for all cases. We understand that the model may have reached an upper limit of validity, given the great simplification in the treatment of the particle-particle collisions and also in the gas turbulence modeling.

Also in order to shed some light in the distribution of the particles in the riser, color maps in the center plane of the riser are presented for each case in Figure 37. At the bottom region, the only difference among the cases is that the lower the velocity, the higher is the buildup of volume fraction near the inlet. At the central region one also notes

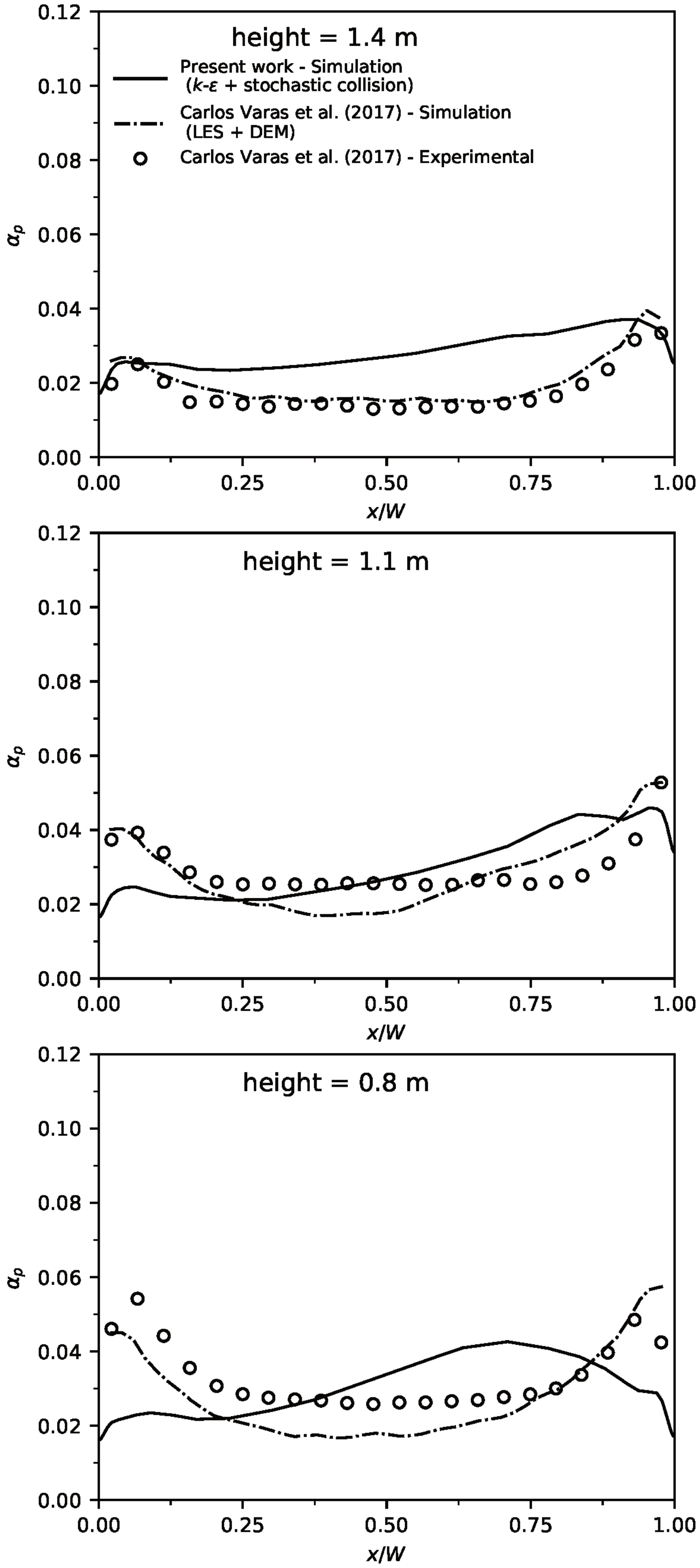

Figure 34 – Particle volume fraction profiles in comparison to the simulation and experiment of Carlos Varas *et al.* (2017a) at three heights: 0.8, 1.1 and 1.4 m above the inlet. Condition: $U_{g,\text{in}} = 5.95\,\text{m/s}$ and $\eta = 21.6\,\text{kg}_{\text{part.}}/\text{kg}_{\text{air}}$.

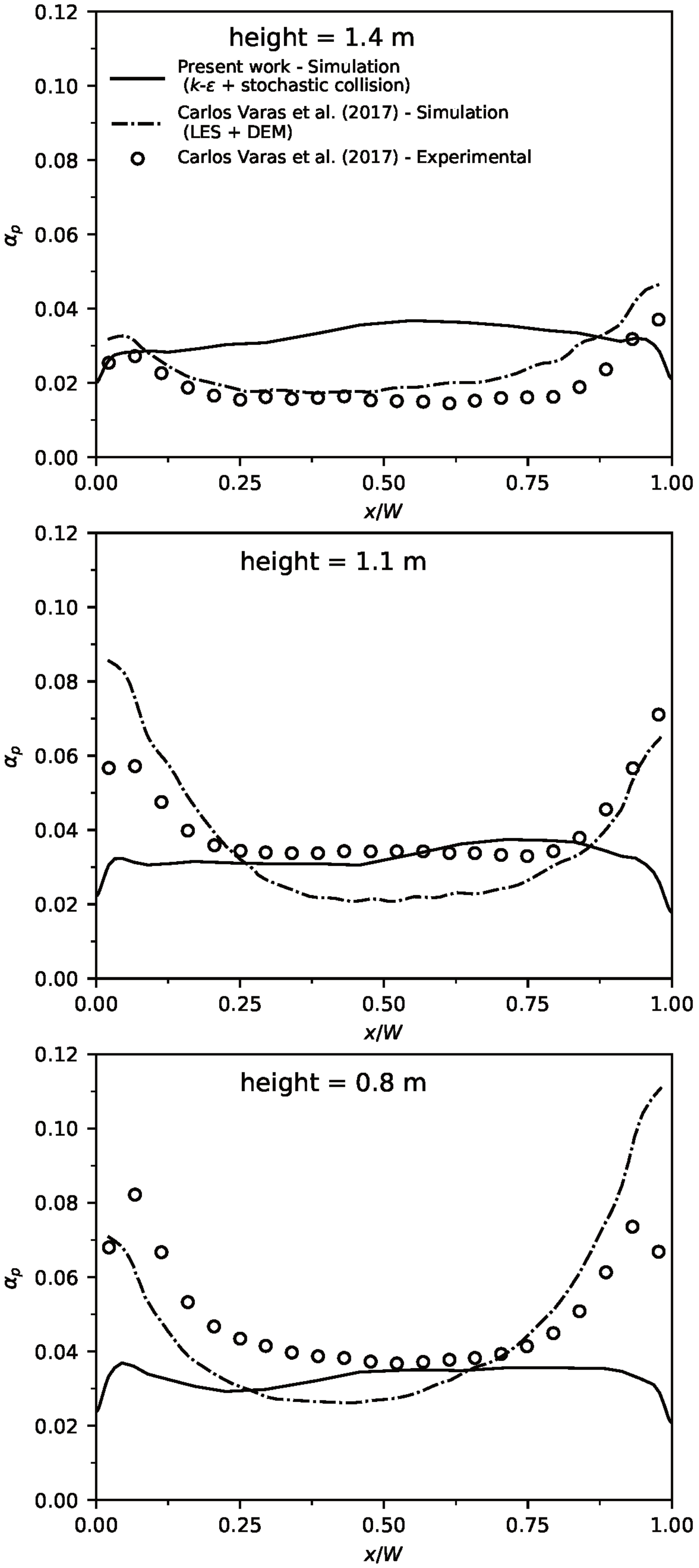

Figure 35 – Particle volume fraction profiles in comparison to the simulation and experiment of Carlos Varas *et al.* (2017a) at three heights: 0.8, 1.1 and 1.4 m above the inlet. Condition: $U_{g,\mathrm{in}} = 5.55\,\mathrm{m/s}$ and $\eta = 23.2\,\mathrm{kg_{part.}/kg_{air}}$.

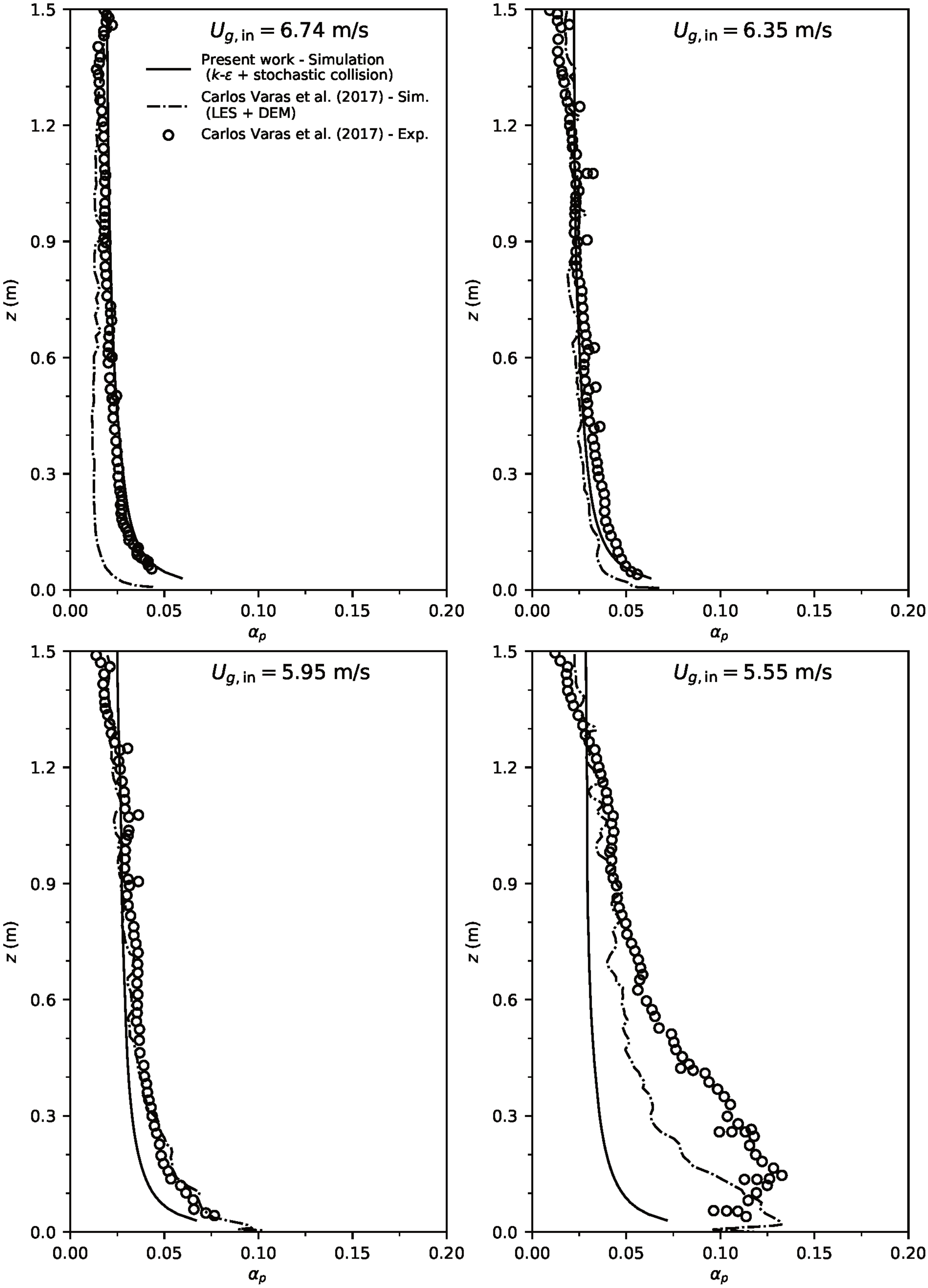

Figure 36 – Axial profile of particle volume fraction in comparison to the simulation and experiment of Carlos Varas *et al.* (2017a) at all 4 conditions.

that a slightly higher volume fraction is shown from left to right, but also there is a smoot change of the core of particles from the center to the right wall. At the exit region the behavior is very similar.

6.2 Modeling study

A few simplifications of the dense formulation that have been shown in literature works, have aroused some interest concerning their influence. The first one is from the neglect of the lift forces. Comparing the particle formulations from dilute and dense flows, one can notice that the lift forces were taken out of the model in the latter case. This was done in compliance to the majority of the other work in the literature. As the effect of the lift on multiple particles is not well known, it is a common simplification to not utilize the isolated sphere lift correlations.

The second one regards the term due to the resolved stresses acting as a force on the particle - recall the first term on the RHS of Equation 3.2.2. As discussed then, some authors neglect this term partially or entirely for particle-laden flows, given that the tangential stress term on the particle is usually small (due to the small velocity gradient over the diameter of the particle), and that the pressure related term could be reduced to the buoyancy if the pressure gradient force due to the flow is assumed small.

The last one comes form an observation made in the present thesis after trying other different riser simulations not shown here. It was noted a difficulty in convergence with the increase of the number of particles in a simulated domain, mainly when those particles had an accumulation near the walls. This was noted when trying to simulate other risers, but also in the geometry of Carlos Varas *et al.* (2017a) using lower inlet velocities for the particles. After many tests and evaluations, it was concluded that this convergence issue came from the transient term in the new continuity equation (Equation 3.67), mainly in the small cells of the wall. Although the issue was isolated, a way to correct it was not found out yet. Also, there is not much information about this issue in the literature. The only mention to this problem came from a reply to an user question on the official CFDEM project[1] forum, by a member of the development team (HAGER, 2018). In this reply, the development engineer writes that this term may be sometimes disregarded because it has "little impact on the result" (HAGER, 2018).

6.2.1 Simulation setup

In this section, three variants of the first case from Carlos Varas *et al.* (2017a), at $U_{g,\mathrm{in}} = 6.74\,\mathrm{m/s}$ and $\eta = 19.1\,\mathrm{kg_{part.}/kg_{air}}$, are simulated: one disregarding the transient

---

[1] The CFDEM project is a software integration for the OpenFOAM using a separate module to do the numerical operations of the DEM collision model. See more in https://www.cfdem.com/

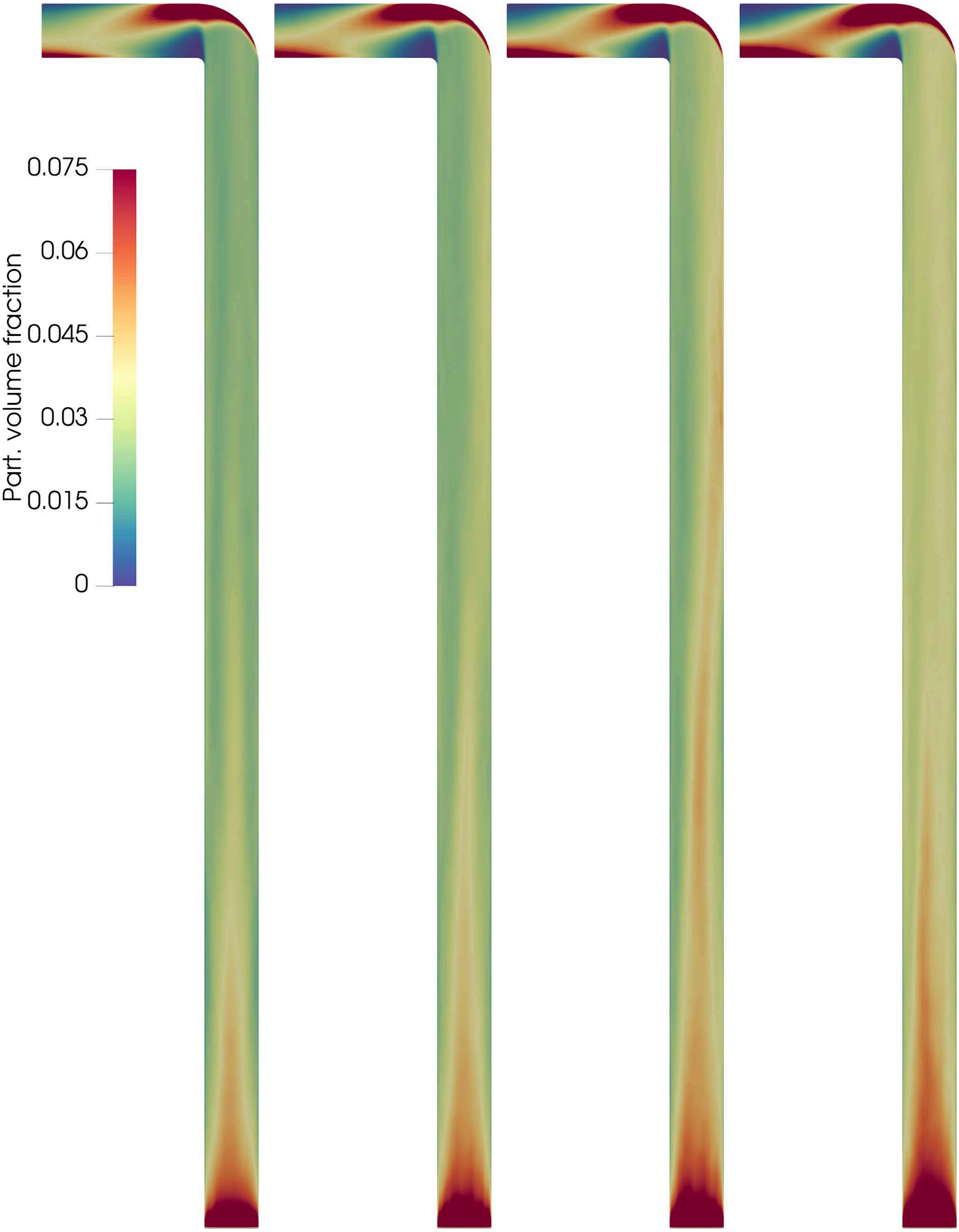

Figure 37 – Particle volume fraction color maps in the center plane of the riser, in decreasing order of velocity from left to right.

term in Equation 3.67; one taking into account the lift forces for isolated sphere, including the particle angular velocity; and the last one neglecting entirely the term from the resolved stresses in Equation 3.2.2. All simulations are carried out in the same computational mesh and other parameters as stated in subsection 6.1.2.

6.2.2 Simulations

In Figure 38 the local particle volume fractions plots are presented in comparison to the experimental data from Carlos Varas *et al.* (2017a) in the three measured heights. The base case refers to the previously shown simulation. One can note that although the removal of the transient term from Equation 3.67 was suggested by Hager (2018), in the present case it shows a great difference from the base case. It overall lowered the volume fraction and also changed the wall with higher accumulation from the right to the left one. The inclusion of the lift forces can have arguably improved the agreement. At 0.8 m it lowered the value at the left wall and enhanced at the right one. This change was also reproduced in 1.1 and 1.4 m. However, this requires more investigation before being able to state that the isolated spheres for lift forces are actually suitable for risers. At last, the removal of the resolved stresses term showed almost no difference from the base case.

The same analysis is carried out in the axial volume fraction profile, in Figure 39, where also the conclusions can be drawn. (1) The removal of the transient term in the new continuity equation changes the prediction and make it worse than the base one. (2) Inclusion of lift forces can improve the agreement (requires more investigation). (3) And the last analysis shows almost no difference in the predictions.

6.3 Formulation influence and side inlet

A last analysis was chosen to be performed at a lower particle mass loading of $\eta = 4.0\,\mathrm{kg_{part.}}/\mathrm{kg_{air}}$. This was made in order to be able to effectively compare the difference from the dilute to the dense formulation, as in the previous cases the dilute formulation was not even able to achieve convergence.

Another test that can be made at this lower η, is injecting the particles by a side inlet. In higher η conditions this was not possible because of a numerical issue. As the side inlet is adjacent to a wall, the cells there are very refined and the particles become larger than the cell. Due to a high accumulation of particle near the inlet, the gas-particle interaction term becomes very large, and without a limiter it makes the solution diverge.

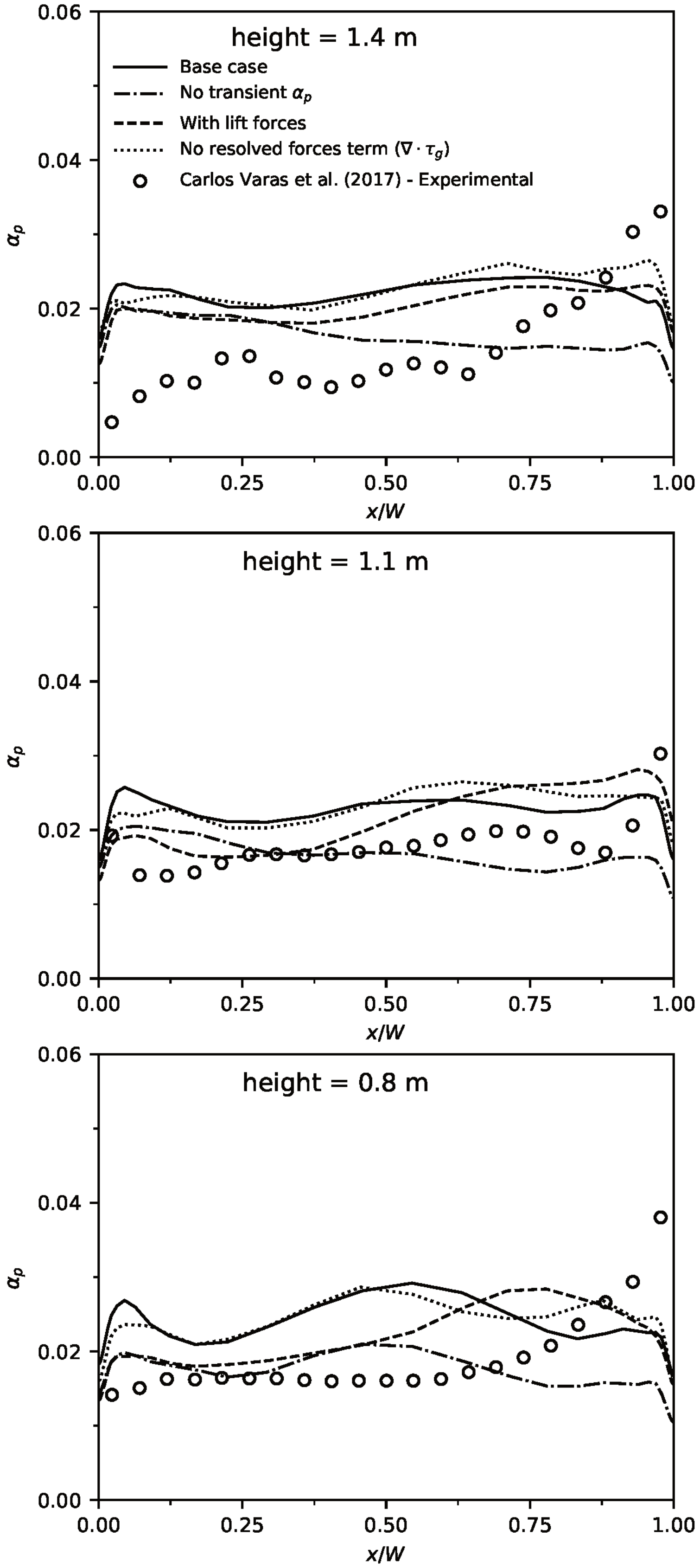

Figure 38 – Particle volume fraction profiles using different simplifications in comparison to the experiment of Carlos Varas *et al.* (2017a). Condition: $U_{g,\mathrm{in}} = 6.74\,\mathrm{m/s}$ and $\eta = 19.1\,\mathrm{kg_{part.}/kg_{air}}$.

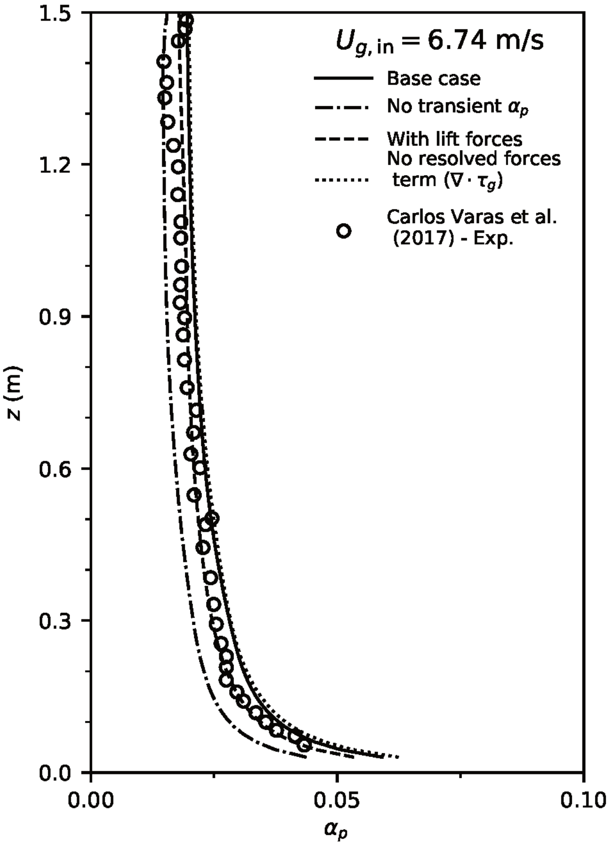

Figure 39 – Axial profile of particle volume fraction using different simplifications in comparison to the experiment of Carlos Varas *et al.* (2017a). Condition: $U_{g,\mathrm{in}} = 6.74\,\mathrm{m/s}$ and $\eta = 19.1\,\mathrm{kg_{part.}/kg_{air}}$.

6.3.1 Simulation setup

In this section's tests, the bottom inlet of the particles was substituted to a side inlet. This side inlet was made by defining some wall boundary cells as injection faces. At these faces, the boundary for the gas remained the same, but the particles were injected there with a velocity of 0.5 m/s in a direction of 45° pointing downwards, trying to mimic the experiments inlet.

Also, the dense and dilute formulations are compared directly. A third formulation is utilized. This one uses the basis of the dilute formulation, but the regular Schiller and Naumann (1935) drag for isolated spheres was replaced by the Tenneti *et al.* (2011) one, in order to evaluate if the differences seen from the dilute to the dense formulation were due to the transport equations, or due to the drag model for population of particles.

6.3.2 Simulations

In the first comparison showing the local profiles of particle volume fraction at the three usual locations, presented in Figure 40, it is clear that while the dense and dilute formulation with the Tenneti *et al.* (2011) drag model are close to each other, the dilute

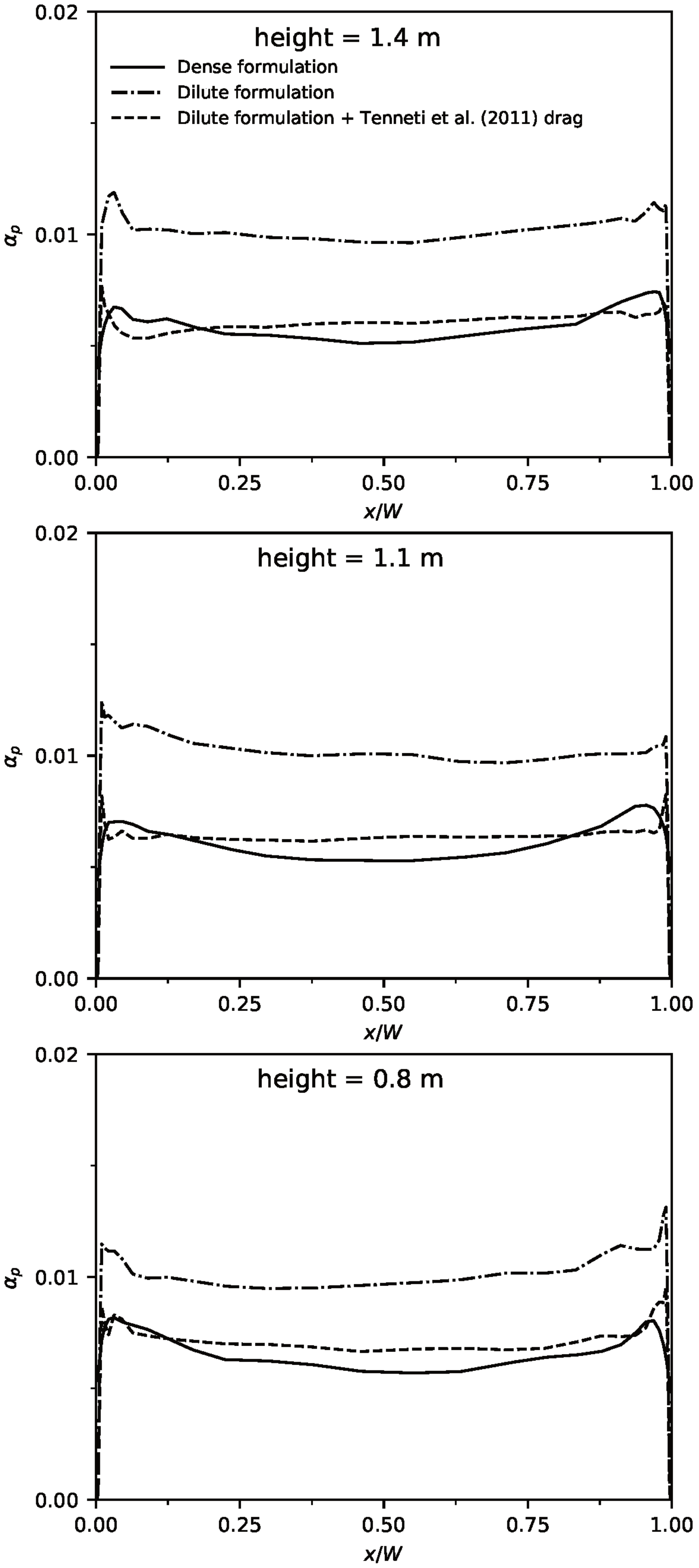

Figure 40 – Particle volume fraction profiles using different formulations. Condition: $U_{g,\mathrm{in}} = 6.74\,\mathrm{m/s}$ and $\eta = 4.0\,\mathrm{kg_{part.}/kg_{air}}$.

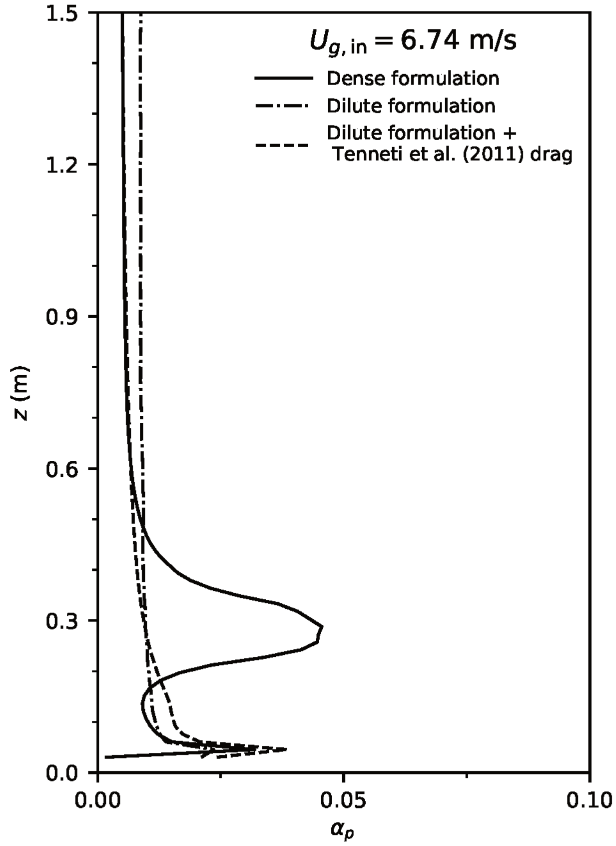

Figure 41 – Axial profile of particle volume fraction using different formulations. Condition: $U_{g,\mathrm{in}} = 6.74\,\mathrm{m/s}$ and $\eta = 4.0\,\mathrm{kg_{part.}/kg_{air}}$.

formulation predicts a much higher concentration of particles in all locations.

Although the dense formulation and the modified dilute one were similar in the last analysis, when looking at the axial volume fraction profiles in Figure 41, one notes a big difference. The dense formulation predicts a region of high accumulation near the inlet, while the other two are very smooth.

It is easier to clarify the differences among these three cases by looking at color maps at the central plane of the riser. In the first one in Figure 42, the particle volume fraction is shown. The first plot shows that the high concentration shown in the previous figure is due to a large cluster formed soon after the inlet. Also, it is clear that the particles are lifted by the gas flow as soon as they are injected into the riser, in a way that is expected from a riser under these circumstances. On the other hand, when utilizing the dilute formulation (middle plot) the particles are not carried straight up. In fact, the majority of the particles fall down and are lifted up after colliding with the gas inlet, in a dynamics that is unphysical to such case, as the drag was not high enough to maintain them in the air. In a test to understand if this only due to the lower drag an isolated sphere experiences in comparison to a population of particles, or due to all the modifications in the alternative formulation, in the third case the dilute formulation is used in combination with the Tenneti *et al.* (2011) drag. It is shown that this third case in fact improves the region near the inlet of the particles, but it is not enough to show as similar dynamics as in the first case.

To complete the above analysis, the color maps of the gas velocity are shown in combination with a representation of each individual particle in Figure 43. It becomes clear that the dense formulation is capable of lifting all the particles. Also as they accumulate in the right wall, the flow in this region is slower, and speeds up in the clear area. The dilute formulation represented in the middle shows almost no difference in the gas velocity in the whole domain, while the particles are all scattered. In the last case is also represented that some particles still fall after the inlet.

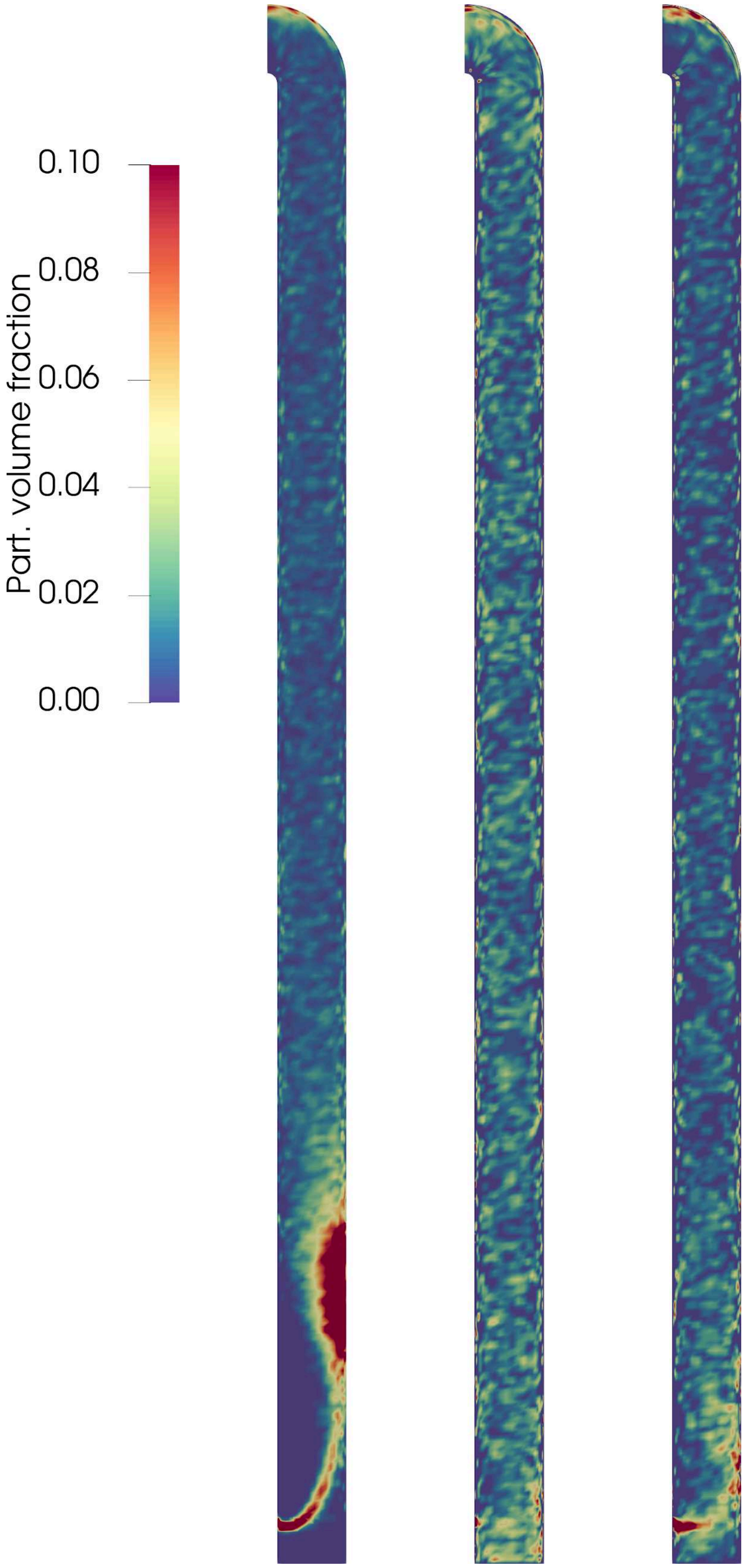

Figure 42 – Particle volume fraction color maps in the center plane of the riser, from left to right: dense formulation; dilute formulation; dilute formulation using the Tenneti *et al.* (2011) drag law.

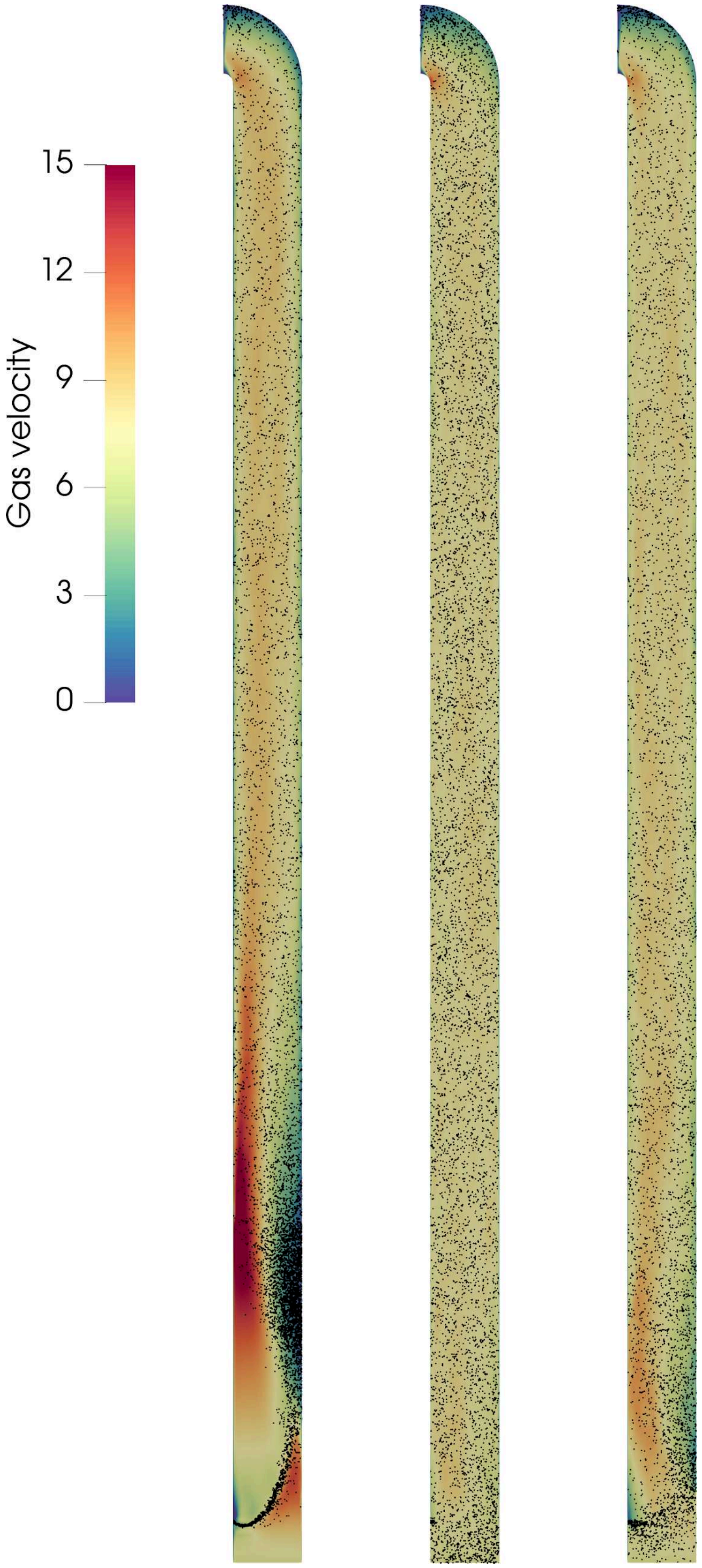

Figure 43 – Gas velocity color maps in the center plane of the riser, from left to right: dense formulation; dilute formulation; dilute formulation using the Tenneti *et al.* (2011) drag law. Black dots are representations of the particles.

Chapter 7

Conclusion

In the last chapter of this thesis, some final considerations about the work carried out are presented. Firstly, the main conclusions and contributions from the simulations using the dilute and dense formulations in many different gas-solid flows are discussed. Also, to finalize the document, suggestions for future work are give. Such suggestions com from the analysis of the points of the present work that need more investigation and also form ideas for studies that can be carried out from here.

7.1 Present contribution

7.1.1 Dilute flows on pipes

In the first part of the thesis, a study on dilute flows was carried out. Although the UNSCYFL3D code was already well-established and validate for such configuration, there were still evaluations to be made. The first one had to do with recent implementations made just before the present thesis for the utilization of polydisperse particles. For this, a case from Huber and Sommerfeld (1998) for horizontal particle-laden pipe flow was simulated, where good agreements were found for the particle velocity and particle diameter distribution profiles. In this same case, we continued to show that the four-way coupling was important even though the flow was dilute, and that the already good accuracy of the two-layer k-ε could be improved by utilizing the RSM model for the turbulence closure modeling.

Another topic of interest when simulating cases with the dilute formulation, was to try to assess the limits of such formulation. So far, the UNSCYFL3D code had only been used for very low solid mass loadings, and its usability at higher ones was not clear. In section 5.2 a study with specifically this objective was carried out. For horizontal pipe flows, comparisons with experiments from Tsuji and Morikawa (1982) showed that the use of such approach is suitable only up to $\eta = 0.9\,\mathrm{kg_{part.}/kg_{air}}$. At higher η, the agreement starts to deviate in such a way that lead us to believe that the the particle-particle collision is responsible, for not being able to account for collisions of particles with such a wide spectrum of diameters. Also, later simulations of this same case with the dense formulation, resulted in very similar profiles.

On the other hand, regarding particle-laden flows in vertical ascending pipes, simulations in comparison to experiments from Tsuji *et al.* (1984) and Mathisen *et al.* (2008) have shown that the dilute formulation considering the stochastic particle-particle collisions could give reasonably good results up to $\eta = 7.9\,\mathrm{kg_{part.}/kg_{air}}$. This increase in the limits of the applicability of the model have to do with the fact that in this configuration the particles are much more well-distributed in the pipe section, which results in still low volume fractions $\mathcal{O}(10^{-3})$ and fewer collisions. Again, posterior simulations of one of this cases with the dense formulation has shown no further improvement.

In a further simplified study, simulations on one case of vertical flow were utilized to evaluate the sensibility of the velocity and concentration profiles with the fluid-exerted forces and with the wall roughness. The conclusions from the mentioned study were not new in the literature, but served to help to validate the code. It has been shown that the transversal lift forces are very important in the particles radial concentration profiles, which can lead to a change in the velocity. Also, the wall roughness has the same influence, and two very different flows can be achieved in only a different wall material pipe configuration.

7.1.2 Dense flow in a CFB riser

In this second part of the thesis, simulations of a CFB riser from Carlos Varas *et al.* (2017a) were carried out in order to verify and validate the new mathematical formulation of the dense gas-solid flows, and to evaluate the performance of the stochastic particle-particle collision model from Sommerfeld (2001) in such scenario. Right at the start, it was possible to see that the previous formulation, for dilute flows, was not suitable for such dense flows in the CFB riser. There was a big accumulation of particles and the simulations diverged.

Following that by utilizing the dense formulation, it was shown that a good agreement was achieved for the first two cases, at $\eta = 19.1\,\mathrm{kg_{part.}/kg_{air}}$ and $\eta = 20.3\,\mathrm{kg_{part.}/kg_{air}}$, with similar accuracy to Carlos Varas *et al.* (2017a) simulations utilizing a the fully deterministic collision model DEM with the LES approach for turbulence closure modeling. At the third condition, $\eta = 21.6\,\mathrm{kg_{part.}/kg_{air}}$, reasonable accuracy was still maintained. However, in the last case at $\eta = 23.2\,\mathrm{kg_{part.}/kg_{air}}$ it was possible to see that the results were not in agreement with either the experiments or simulations from Carlos Varas *et al.*

(2017a). It is not totally clear, but the explanation is possibly the same from the horizontal cases in the dilute flows, that the collision model could not handle the increase in collisions.

We then proceeded with a modeling study to assess if some change in the model or in the forces could have a great effect on the results. The simulations have shown that the inclusion of lift forces can have a positive influence on the concentration profiles, although it is hard to state this with only a few tests. Lift forces are generally excluded of the modeling of CFB risers because its relation form isolated conditions to the presence of multiple particles is not known as is the drag. On the other hand, some works and softwares remove the transient α_g term from the continuity equation because of numerical issues claiming that this term leads to almost no difference in the predictions. The test in this CFB riser has shown that removing this term change the results for worse.

In the last study, the same riser was simulated in a much lower solids mass loading condition, $\eta = 4\,\mathrm{kg}_{\mathrm{part.}}/\mathrm{kg}_{\mathrm{air}}$, so that the dilute formulation could provide results and its differences with the dense one could be clarified. Moreover, this last assessment is carried out utilizing a side inlet for the particles, trying to mimic the experiments. Firstly, it was shown that the side inlet can change the concentration profiles and that the current formulation can predict clusters. Regarding the formulations, the dilute one could not provide a stable inlet of particles, and the majority of them fell to the gas inlet instead of going upwards, as one would expect. Only the dense formulation could provide a prediction where the particles would go straight upwards from the inlet. Out of scientific curiosity, a third case using the dilute formulation, but with the drag force modeling of the dense one, was carried out and showed that this was not only an effect of the forces involved, but the greatest influence comes from the volume fraction in the fluid equations.

7.2 Future and suggested works

Throughout the development of the present thesis, many challenges had to be overcome in order to reach these final simulations of dense flows in a CFB riser. Since the implementation of a new formulation, which had many sub-steps involved, to testing a collision model that had not been tested before for such conditions. During this run, and from the conclusions drawn from the results, it was possible to identify many points in which further developments are due. It is our duty as researchers to also points out such questions, so others can move from there, and science and engineering evolves:

a) try the collision efficiency model from Blei *et al.* (2002), to assess its influence in polydisperse particle-laden flows cases;

b) further investigate the convergence problem related to the new transient term in the continuity equation, which we have shown to be important in the present thesis cases;

c) implement a limiter to the gas-particle interaction term, such as is utilized for α_g, so that simulations with side inlets where the particles cross thin cells can converge easier;

d) now that the one important aspect for dense flows was implementation, the use of α_g in the fluid flow equations, test other non-deterministic collision models (even using other software or cases) to evaluate the relative accuracy to the Sommerfeld (2001) model;

e) simulate Utzig (2016) CFB riser experimental case.

Bibliography

ABBASI, A.; EGE, P. E.; LASA, H. I. de. CPFD simulation of a fast fluidized bed steam coal gasifier feeding section. *Chemical Engineering Journal*, v. 174, n. 1, p. 341–350, 2011. doi:10.1016/j.cej.2011.07.085. Cited on page 46.

ADAMCZYK, W. P.; KLIMANEK, A.; BIAŁECKI, R. A.; WECEL, G.; KOZOŁUB, P.; CZAKIERT, T. Comparison of the standard Euler-Euler and hybrid Euler-Lagrange approaches for modeling particle transport in a pilot-scale circulating fluidized bed. *Particuology*, v. 15, p. 129–137, 2014. doi:10.1016/j.partic.2013.06.008. Cited on page 44.

ADNAN, M.; ZHANG, N.; SUN, F.; WANG, W. Numerical simulation of a semi-industrial scale CFB riser using coarse-grained DDPM-EMMS modelling. *The Canadian Journal of Chemical Engineering*, v. 96, n. 6, p. 1403–1416, 2018. doi:10.1002/cjce.23071. Cited on page 44.

ALLETTO, M. *Numerical investigation of the influence of particle-particle and particle-wall collisions in turbulent wall-bounded flows at high mass loadings*. Thesis (PhD) — Helmut Schmidt Universität, Hamburg, 2014. Available from INIS: <http://inis.iaea.org/search/search.aspx?orig_q=RN:47028461>. Cited on page 56.

ALLETTO, M.; BREUER, M. Prediction of turbulent particle-laden flow in horizontal smooth and rough pipes inducing secondary flow. *International Journal of Multiphase Flow*, v. 55, p. 80–98, 2013. doi:10.1016/j.ijmultiphaseflow.2013.04.009. Cited 2 times on pages 43 and 77.

ALOBAID, F.; EPPLE, B. Improvement, validation and application of CFD/DEM model to dense gas-solid flow in a fluidized bed. *Particuology*, v. 11, n. 5, p. 514–526, 2013. doi:10.1016/j.partic.2012.05.008. Cited on page 44.

ANDERSON, T. B.; JACKSON, R. Fluid mechanical description of fluidized beds: equations of motion. *Industrial & Engineering Chemistry Fundamentals*, v. 6, n. 4, p. 527–539, 1967. doi:10.1021/i160024a007. Cited 5 times on pages 41, 62, 63, 66, and 67.

ANDREWS, M. J.; O'ROURKE, P. J. The multiphase particle-in-cell (MP-PIC) method for dense particulate flows. *International Journal of Multiphase Flow*, v. 22, n. 2, p. 379–402, 1996. doi:10.1016/0301-9322(95)00072-0. Cited on page 45.

BARTHOLOMEW, P.; DENNER, F.; ABDOL-AZIS, M. H.; MARQUIS, A.; WACHEM, B. G. M. van. Unified formulation of the momentum-weighted interpolation for collocated variable arrangements. *Journal of Computational Physics*, v. 375, p. 177–208, 2018. doi:10.1016/j.jcp.2018.08.030. Cited 2 times on pages 82 and 83.

BENSON, M.; TANAKA, T.; EATON, J. K. Effects of wall roughness on particle velocities in a turbulent channel flow. *Journal of Fluids Engineering*, v. 127, n. 2, p. 250–256, 2005. doi:10.1115/1.1891149. Cited on page 77.

BERROUK, A. S.; PORNSILPH, C.; BALE, S. S.; DU, Y.; NANDAKUMAR, K. Simulation of a large-scale fcc riser using a combination of MP-PIC and four-lump oil-cracking kinetic models. *Energy & Fuels*, v. 31, n. 5, p. 4758–4770, 2017. doi:10.1021/acs.energyfuels.6b03380. Cited on page 46.

BIRD, R. B.; STEWART, W. E.; LIGHTFOOT, E. N. *Transport Phenomena*. 2. ed. New York: John Wiley & Sons, 2002. Cited on page 50.

BLEI, S.; HO, C. A.; SOMMERFELD, M. A stochastic droplet collision model with consideration of impact efficiency. In: *ILASS-Europe*. Zaragoza: [s.n.], 2002. Cited 2 times on pages 101 and 141.

BREUER, M.; ALLETTO, M. Efficient simulation of particle-laden turbulent flows with high mass loadings using LES. *International Journal of Heat and Fluid Flow*, v. 35, p. 2–12, 2012. doi:10.1016/j.ijheatfluidflow.2012.01.001. Cited on page 73.

CAPECELATRO, J.; DESJARDINS, O. An Euler-Lagrange strategy for simulating particle-laden flows. *Journal of Computational Physics*, v. 238, p. 1–31, 2013. doi:10.1016/j.jcp.2012.12.015. Cited 10 times on pages 41, 43, 48, 62, 63, 66, 67, 68, 86, and 87.

CAPECELATRO, J.; PEPIOT, P.; DESJARDINS, O. Numerical characterization and modeling of particle clustering in wall-bounded vertical risers. *Chemical Engineering Journal*, v. 245, p. 295–310, 2014. doi:10.1016/j.cej.2014.02.040. Cited on page 44.

CARLOS VARAS, A. E.; PETERS, E. A. J. F.; DEEN, N. G.; KUIPERS, J. A. M. Solids volume fraction measurements on riser flow using a temporal-histogram based DIA method. *AIChE Journal*, v. 62, n. 8, p. 2681–2698, 2016. doi:10.1002/AIC.15243. Cited on page 118.

CARLOS VARAS, A. E.; PETERS, E. A. J. F.; KUIPERS, J. A. M. CFD-DEM simulations and experimental validation of clustering phenomena and riser hydrodynamics. *Chemical Engineering Science*, v. 169, p. 246–258, 2017. doi:10.1016/j.ces.2016.08.030. Cited 19 times on pages 16, 17, 44, 117, 118, 119, 120, 121, 122, 123, 124, 125, 126, 127, 129, 130, 131, 132, and 140.

CARLOS VARAS, A. E.; PETERS, E. A. J. F.; KUIPERS, J. A. M. Experimental study of full field riser hydrodynamics by PIV/DIA coupling. *Powder Technology*, v. 313, p. 402–416, 2017. doi:10.1016/j.powtec.2017.01.055. Cited on page 118.

CHEN, C.; WERTHER, J.; HEINRICH, S.; QI, H.-Y.; HARTGE, E.-U. CPFD simulation of circulating fluidized bed risers. *Powder Technology*, v. 235, p. 238–247, 2013. doi:10.1016/j.powtec.2012.10.014. Cited on page 46.

CHEN, H. C.; PATEL, V. C. Near-wall turbulence models fo complex flows including separation. *AIAA Journal*, v. 26, n. 6, p. 641–648, 1988. doi:10.2514/3.9948. Cited on page 54.

CHEN, X.; WANG, J. A comparison of two-fluid model, dense discrete particle model and CFD-DEM method for modeling impinging gas-solid flows. *Powder Technology*, v. 254, p. 94–102, 2014. doi:10.1016/j.powtec.2013.12.056. Cited on page 44.

CHIESA, M.; MATHIESEN, V.; MELHEIM, J. A.; HALVORSEN, B. Numerical simulation of particulate flow by the Eulerian-Lagrangian and the Eulerian-Eulerian approach with application to a fluidized bed. *Computers & Chemical Engineering*, v. 29, n. 2, p. 291–304, 2005. doi:10.1016/j.compchemeng.2004.09.002. Cited on page 44.

CHU, K. W.; WANG, B.; YU, A. B.; VINCE, A.; BARNETT, G. D.; BARNETT, P. J. CFD-DEM study of the effect of particle density distribution on the multiphase flow and performance of dense medium cyclone. *Minerals Engineering*, v. 22, n. 11, p. 893–909, 2009. doi:10.1016/j.mineng.2009.04.008. Cited on page 42.

CHU, S.; PROSPERETTI, A. On flux terms in volume averaging. *International Journal of Multiphase Flow*, v. 80, p. 176–180, 2016. doi:10.1016/j.ijmultiphaseflow.2015.12.009. Cited on page 41.

CLOETE, S.; JOHANSEN, S. T.; AMINI, S. Performance evaluation of a complete Lagrangian KTGF approach for dilute granular flow modelling. *Powder Technology*, v. 226, p. 43–52, 2012. doi:10.1016/j.powtec.2012.04.010. Cited on page 44.

COELHO, R. M. L.; MASSARANI, G. Fluidodinâmica da partícula sólida isolada. In: *Anais Do XXIV Congresso Brasileiro de Sistemas Particulados*. Uberlândia: [s.n.], 1996. v. 1, p. 19. Cited on page 57.

CROWE, C. T.; SCHWARZKOPF, J. D.; SOMMERFELD, M.; TSUJI, Y. *Multiphase Flows with Droplets and Particles*. 2. ed. ed. Boca Raton: CRC Press, 2011. Cited 6 times on pages 41, 49, 56, 62, 67, and 72.

CSANADY, G. T. Turbulent diffusion of heavy particles in the atmosphere. *Journal of the Atmospheric Sciences*, v. 20, n. 3, p. 201–208, 1963. doi:10.1175/1520-0469(1963)020<0201:TDOHPI>2.0.CO;2. Cited on page 71.

CUBERO, A.; SÁNCHEZ-INSA, A.; FUEYO, N. A consistent momentum interpolation method for steady and unsteady multiphase flows. *Computers & Chemical Engineering*, v. 62, p. 96–107, 2014. doi:10.1016/j.compchemeng.2013.12.002. Cited 2 times on pages 82 and 83.

CUNDALL, P. A.; STRACK, O. D. L. A discrete numerical model for granular assemblies. *Géotechnique*, v. 29, n. 1, p. 47–65, 1979. doi:10.1680/geot.1979.29.1.47. Cited on page 43.

DANDY, D. S.; DWYER, H. A. A sphere in shear flow at finite Reynolds number: effect of shear on particle lift, drag, and heat transfer. *Journal of Fluid Mechanics*, v. 216, p. 381–410, 1990. doi:10.1017/S0022112090000477. Cited on page 58.

DAVIDSON, L. *Fluid Mechanics, Turbulent Flow and Turbulence Modeling*. Götemburg: [s.n.], 2019. Available from Chalmers University: <http://www.tfd.chalmers.se/~lada/postscript_files/solids-and-fluids_turbulent-flow_turbulence-modelling.pdf>. Cited on page 51.

DENNIS, S. C. R.; SINGH, S. N.; INGHAM, D. B. The steady flow due to a rotating sphere at low and moderate Reynolds number. *Journal of Fluid Mechanics*, v. 101, n. 2, p. 257–279, 1980. doi:10.1017/S0022112080001656. Cited on page 61.

DUARTE, C. A. R.; SOUZA, F. J. de. Innovative pipe wall design to mitigate elbow erosion: a CFD analysis. *Wear*, v. 380-381, p. 176–190, 2017. doi:10.1016/j.wear.2017.03.015. Cited on page 35.

DUARTE, C. A. R.; SOUZA, F. J. de; SALVO, R. de V.; SANTOS, V. F. dos. The role of inter-particle collisions on elbow erosion. *International Journal of Multiphase Flow*, v. 89, p. 1–22, 2017. doi:10.1016/j.ijmultiphaseflow.2016.10.001. Cited 2 times on pages 35 and 77.

DUARTE, C. A. R.; SOUZA, F. J. de; SANTOS, V. F. dos. Numerical investigation of mass loading effects on elbow erosion. *Powder Technology*, v. 283, p. 593–606, 2015. doi:10.1016/j.powtec.2015.06.021. Cited on page 35.

DUARTE, C. A. R.; SOUZA, F. J. de; SANTOS, V. F. dos. Mitigating elbow erosion with a vortex chamber. *Powder Technology*, v. 288, p. 6–25, 2016. doi:10.1016/j.powtec.2015.10.032. Cited on page 35.

DUARTE, C. A. R.; SOUZA, F. J. de; VENTURI, D. N.; SOMMERFELD, M. A numerical assessment of two geometries for reducing elbow erosion. *Particuology*, 2019. doi:10.1016/j.partic.2019.01.004. Cited on page 35.

ENWALD, H.; PEIRANO, E.; ALMSTEDT, A. E. Eulerian two-phase flow theory applied to fluidization. *International Journal of Multiphase Flow*, v. 22, p. 21–66, 1996. doi:10.1016/S0301-9322(96)90004-X. Cited on page 41.

EVRARD, F.; DENNER, F.; van Wachem, B. A multi-scale approach to simulate atomisation processes. *International Journal of Multiphase Flow*, v. 119, p. 194–216, 2019. doi:10.1016/j.ijmultiphaseflow.2019.07.005. Cited on page 48.

FENG, Y. Q.; YU, A. B. Assessment of model formulations in the discrete particle simulation of gas-solid flow. *Industrial & Engineering Chemistry Research*, v. 43, n. 26, p. 8378–8390, 2004. doi:10.1021/ie049387v. Cited on page 41.

FENG, Y. Q.; YU, A. B. Comments on "Discrete particle-continuum fluid modelling of gas-solid fluidised beds" by Kafui et al. [Chemical Engineering Scinece 57 (2002) 2395-2410]. *Chemical Engineering Science*, v. 59, n. 3, p. 719–722, 2004. doi:10.1016/j.ces.2003.11.003. Cited on page 41.

FERZIGER, J. H.; PERIC, M.; STREET, R. L. *Computational Methods for Fluid Dynamics*. 4. ed. [S.l.]: Springer International Publishing, 2020. doi:10.1007/978-3-319-99693-6. Cited on page 80.

GARG, R.; DIETIKER, J. F. *Documentation of open-source MFIX-PIC software for gas-solids flows*. 2013. <https://mfix.netl.doe.gov/>. Cited on page 46.

GIBILARO, L. G.; GALLUCCI, K.; FELICE, R. D.; PAGLIAI, P. On the apparent viscosity of a fluidized bed. *Chemical Engineering Science*, v. 62, n. 1, p. 294–300, 2007. doi:10.1016/j.ces.2006.08.030. Cited on page 66.

GIDASPOW, D. *Multiphase Flow and Fluidization Continuum and Kinetic Theory Description*. Boston: Academic Press, 1994. Cited on page 41.

HAGER, A. Development Team, CFDEM Project Official Forum, Online Reply at <https://www.cfdem.com/forums/can-someone-brief-what-useddtvoidfraction-does?destination=node/14499>, *Can Someone Brief What useDDTvoidfraction Does?* 2018. Cited 2 times on pages 129 and 130.

HAIDER, A.; LEVENSPIEL, O. Drag coefficient and terminal velocity of spherical and nonspherical particles. *Powder Technology*, v. 58, n. 1, p. 63–70, 1989. doi:10.1016/0032-5910(89)80008-7. Cited on page 57.

HASELBACHER, A.; NAJJAR, F. M.; FERRY, J. P. An efficient and robust particle-localization algorithm for unstructured grids. *Journal of Computational Physics*, v. 225, n. 2, p. 2198–2213, 2007. doi:10.1016/j.jcp.2007.03.018. Cited on page 86.

HE, Y.; DEEN, N. G.; ANNALAND, M. van S.; KUIPERS, J. A. M. Gas-solid turbulent flow in a circulating fluidized bed riser: numerical study of binary particle systems. *Industrial & Engineering Chemistry Research*, v. 48, n. 17, p. 8098–8108, 2009. doi:10.1021/ie8015297. Cited on page 43.

HEINTZENBERG, J. Properties of the log-normal particle size distribution. *Aerosol Science and Technology*, v. 21, n. 1, p. 46–48, 1994. doi:10.1080/02786829408959695. Cited on page 74.

HOEF, M. A. van der; YE, M.; ANNALAND, M. van S.; ANDREWS, A. T.; SUNDARESAN, S.; KUIPERS, J. A. M. Multiscale modeling of gas-fluidized beds. In: MARIN, G. B. (Ed.). *Computational Fluid Dynamics*. [S.l.]: Academic Press, 2006, (Advances in Chemical Engineering, v. 31). p. 65–149. doi:10.1016/S0065-2377(06)31002-2. Cited on page 44.

HUBER, N.; SOMMERFELD, M. Modelling and numerical calculation of dilute-phase pneumatic conveying in pipe systems. *Powder Technology*, v. 99, n. 1, p. 90–101, 1998. doi:10.1016/S0032-5910(98)00065-5. Cited 10 times on pages 15, 90, 91, 92, 93, 95, 96, 97, 98, and 139.

JIANG, Y.; QIU, G.; WANG, H. Modelling and experimental investigation of the full-loop gas-solid flow in a circulating fluidized bed with six cyclone separators. *Chemical Engineering Science*, v. 109, p. 85–97, 2014. doi:10.1016/j.ces.2014.01.029. Cited on page 46.

JONES, W. P.; LAUNDER, B. E. The prediction of laminarization with a two-equation model of turbulence. *International Journal of Heat and Mass Transfer*, v. 15, n. 2, p. 301–314, 1972. doi:10.1016/0017-9310(72)90076-2. Cited on page 53.

KAFUI, K. D.; THORNTON, C.; ADAMS, M. J. Discrete particle-continuum fluid modelling of gas-solid fluidised beds. *Chemical Engineering Science*, v. 57, n. 13, p. 2395–2410, 2002. doi:10.1016/S0009-2509(02)00140-9. Cited on page 41.

KAFUI, K. D.; THORNTON, C.; ADAMS, M. J. Reply to Comments by Feng and Yu on “Discrete particle-continuum fluid modelling of gas-solid fluidised beds” by Kafui et al. *Chemical Engineering Science*, v. 59, n. 3, p. 723–725, 2004. doi:10.1016/j.ces.2003.11.004. Cited on page 41.

KHOSLA, P. K.; RUBIN, S. G. A diagonally dominant second-order accurate implicit scheme. *Computers & Fluids*, v. 2, p. 207–209, 1974. doi:10.1016/0045-7930(74)90014-0. Cited on page 81.

KLIMANEK, A.; ADAMCZYK, W.; KATELBACH-WOŹNIAK, A.; WĘCEL, G.; SZLĘK, A. Towards a hybrid Eulerian-Lagrangian CFD modeling of coal gasification in a circulating fluidized bed reactor. *Fuel*, v. 152, p. 131–137, 2015. doi:10.1016/j.fuel.2014.10.058. Cited on page 44.

KUSSIN, J.; SOMMERFELD, M. Experimental studies on particle behaviour and turbulence modification in horizontal channel flow with different wall roughness. *Experiments in Fluids*, v. 33, n. 1, p. 143–159, 2002. doi:10.1007/s00348-002-0485-9. Cited on page 77.

LAÍN, S.; GRILLO, C. A. Comparison of turbulent particle dispersion models in turbulent shear flows. *Brazilian Journal of Chemical Engineering*, v. 24, n. 3, p. 351–363, 2007. doi:10.1590/S0104-66322007000300005. Cited on page 71.

LAÍN, S.; SOMMERFELD, M. Euler/Lagrange computations of pneumatic conveying in a horizontal channel with different wall roughness. *Powder Technology*, v. 184, n. 1, p. 76–88, 2008. doi:10.1016/j.powtec.2007.08.013. Cited 2 times on pages 46 and 71.

LAÍN, S.; SOMMERFELD, M. Numerical calculation of pneumatic conveying in horizontal channels and pipes: Detailed analysis of conveying behaviour. *International Journal of Multiphase Flow*, v. 39, p. 105–120, 2012. doi:10.1016/j.ijmultiphaseflow.2011.09.006. Cited 2 times on pages 46 and 77.

LAÍN, S.; SOMMERFELD, M. Characterisation of pneumatic conveying systems using the Euler/Lagrange approach. *Powder Technology*, v. 235, p. 764–782, 2013. doi:10.1016/j.powtec.2012.11.029. Cited 5 times on pages 15, 46, 90, 91, and 95.

LAUNDER, B. E.; REECE, G. J.; RODI, W. Progress in the development of a Reynolds-stress turbulence closure. *Journal of Fluid Mechanics*, v. 68, n. 3, p. 537–566, 1975. doi:10.1017/S0022112075001814. Cited on page 54.

LAUNDER, B. E.; SHARMA, B. I. Application of the energy-dissipation model of turbulence to the calculation of flow near a spinning disc. *Letters in Heat and Mass Transfer*, v. 1, n. 2, p. 131–137, 1974. doi:10.1016/0094-4548(74)90150-7. Cited on page 53.

LESIEUR, M. *Turbulence in Fluids*. Dordrecht: Springer Netherlands, 2008. v. 84. (Fluid Mechanics and Its Applications, v. 84). doi:10.1007/978-1-4020-6435-7. Cited on page 51.

LI, F.; SONG, F.; BENYAHIA, S.; WANG, W.; LI, J. MP-PIC simulation of CFB riser with EMMS-based drag model. *Chemical Engineering Science*, v. 82, p. 104–113, 2012. doi:10.1016/j.ces.2012.07.020. Cited on page 46.

LIANG, Y.; ZHANG, Y.; LI, T.; LU, C. A critical validation study on CPFD model in simulating gas-solid bubbling fluidized beds. *Powder Technology*, v. 263, p. 121–134, 2014. doi:10.1016/j.powtec.2014.05.003. Cited on page 46.

LIM, K. S.; ZHU, J. X.; GRACE, J. R. Hydrodynamics of gas-solid fluidization. *International Journal of Multiphase Flow*, v. 21, p. 141–193, 1995. doi:10.1016/0301-9322(95)00038-Y. Cited 2 times on pages 15 and 33.

LOPES, D. S.; SILVA, M. T.; AMBRÓSIO, J. A. Tangent vectors to a 3-D surface normal: a geometric tool to find orthogonal vectors based on the Householder transformation. *Computer-Aided Design*, v. 45, n. 3, p. 683–694, 2013. doi:10.1016/j.cad.2012.11.003. Cited on page 75.

LOTH, E. Lift of a spherical particle subject to vorticity and/or spin. *AIAA Journal*, v. 46, n. 4, p. 801–809, 2008. doi:10.2514/1.29159. Cited on page 60.

LOTH, E. *Particles, Drops and Bubbles: Fluid Dynamics and Numerical Methods*. London: Cambridge University Press, 2010. Cited on page 56.

LOTH, E. Overview of numerical approaches. In: MICHAELIDES, E. E.; CROWE, C. T.; SCHWARZKOPF, J. D. (Ed.). *Multiphase Flow Handbook*. 2. ed. Boca Raton: CRC Press, 2016. Cited on page 56.

LU, L.; KONAN, A.; BENYAHIA, S. Influence of grid resolution, parcel size and drag models on bubbling fluidized bed simulation. *Chemical Engineering Journal*, v. 326, p. 627–639, 2017. doi:10.1016/j.cej.2017.06.002. Cited on page 44.

LU, L.; XU, J.; GE, W.; YUE, Y.; LIU, X.; LI, J. EMMS-based discrete particle method (EMMS-DPM) for simulation of gas-solid flows. *Chemical Engineering Science*, v. 120, p. 67–87, 2014. doi:10.1016/j.ces.2014.08.004. Cited 2 times on pages 42 and 44.

LU, L.; XU, Y.; LI, T.; BENYAHIA, S. Assessment of different coarse graining strategies to simulate polydisperse gas-solids flow. *Chemical Engineering Science*, v. 179, p. 53–63, 2018. doi:10.1016/j.ces.2018.01.003. Cited 2 times on pages 42 and 44.

LUN, C. K. K.; LIU, H. S. Numerical simulation of dilute turbulent gas-solid flows in horizontal channels. *International Journal of Multiphase Flow*, v. 23, n. 3, p. 575–605, 1997. doi:10.1016/S0301-9322(96)00087-0. Cited 2 times on pages 59 and 60.

MALISKA. *Transferência de Calor e Mecânica dos Fluídos Computacional*. Edição: 2. Rio de Janeiro: LTC, 2004. Cited on page 80.

MALLOUPPAS, G.; WACHEM, B. van. Large Eddy Simulations of turbulent particle-laden channel flow. *International Journal of Multiphase Flow*, v. 54, p. 65–75, 2013. doi:10.1016/j.ijmultiphaseflow.2013.02.007. Cited on page 43.

MANDO, M.; YIN, C. Euler-Lagrange simulation of gas-solid pipe flow with smooth and rough wall boundary conditions. *Powder Technology*, v. 225, p. 32–42, 2012. doi:10.1016/j.powtec.2012.03.029. Cited 3 times on pages 110, 113, and 114.

MARTINS, D. A. de M. *Implementação e avaliação de modelos computacionais para a previsão da erosão em ciclones*. Thesis (PhD) — Federal University of Uberlândia, Uberlândia, 2016. Available at: <https://repositorio.ufu.br/handle/123456789/14775>. Cited on page 80.

MARTINS, D. A. de M.; SOUZA, F. J. de; SALVO, R. de V. Formation of vortex breakdown in conical-cylindrical cavities. *International Journal of Heat and Fluid Flow*, v. 48, p. 52–68, 2014. doi:10.1016/j.ijheatfluidflow.2014.05.001. Cited on page 35.

MATHISEN, A.; HALVORSEN, B.; MELAAEN, M. C. Experimental Studies of Dilute Vertical Pneumatic Transport. *Particulate Science and Technology*, v. 26, n. 3, p. 235–246, 2008. doi:10.1080/02726350802028900. Cited 11 times on pages 16, 102, 103, 106, 107, 109, 110, 112, 113, 114, and 140.

MATHUR, S.; MURTHY, J. A pressure-based method for unstructured meshes. *Numerical Heat Transfer*, v. 31, p. 195–215, 1997. doi:10.1080/10407799708915105. Cited on page 82.

MCLAUGHLIN, J. B. Inertial migration of a small sphere in linear shear flows. *Journal of Fluid Mechanics*, v. 224, p. 261–274, 1991. doi:10.1017/S0022112091001751. Cited 2 times on pages 57 and 58.

MEI, R. An approximate expression for the shear lift force on a spherical particle at finite reynolds number. *International Journal of Multiphase Flow*, v. 18, n. 1, p. 145–147, 1992. doi:10.1016/0301-9322(92)90012-6. Cited on page 58.

MORSI, S. A.; ALEXANDER, A. J. An investigation of particle trajectories in two-phase flow systems. *Journal of Fluid Mechanics*, v. 55, n. 02, p. 193, 1972. doi:10.1017/S0022112072001806. Cited on page 57.

MOUKALLED, F.; MANGANI, L.; DARWISH, M. *The Finite Volume Method in Computational Fluid Dynamics: An Advanced Introduction with OpenFOAM® and Matlab.* [S.l.]: Springer International Publishing, 2016. (Fluid Mechanics and Its Applications). doi:10.1007/978-3-319-16874-6. Cited 2 times on pages 80 and 82.

MÜLLER, C. R.; SCOTT, S. A.; HOLLAND, D. J.; CLARKE, B. C.; SEDERMAN, A. J.; DENNIS, J. S.; GLADDEN, L. F. Validation of a discrete element model using magnetic resonance measurements. *Particuology*, v. 7, n. 4, p. 297–306, 2009. doi:10.1016/j.partic.2009.04.002. Cited on page 44.

NAPOV, A.; NOTAY, Y. An algebraic multigrid method with guaranteed convergence rate. *SIAM Journal of Scientific Computing*, v. 34, p. A1079–A1109, 2012. doi:10.1137/100818509. Cited on page 84.

NOTAY, Y. An aggregation-based albegraic multigrid method. *Eletronic Transactions on Numerical Analysis*, v. 37, p. 123–146, 2010. Cited on page 84.

NOTAY, Y. Aggregation-based algebraic multigrid for convection-diffusion equations. *SIAM Journal of Scientific Computing*, v. 34, p. A2288–A2316, 2012. doi:10.1137/110835347. Cited on page 84.

OESTERLÉ, B.; DINH, T. B. Experiments on the lift of a spinning sphere in a range of intermediate Reynolds numbers. *Experiments in Fluids*, v. 25, n. 1, p. 16–22, 1998. doi:10.1007/s003480050203. Cited on page 59.

OESTERLÉ, B.; PETITJEAN, A. Simulation of particle-to-particle interactions in gas solid flows. *International Journal of Multiphase Flow*, v. 19, n. 1, p. 199–211, 1993. doi:10.1016/0301-9322(93)90033-Q. Cited 2 times on pages 32 and 74.

OESTERLÉ, B.; TRI, B. D.; VIAL, J. L. Measurements of lift and torque on a rotating sphere at intermediate Reynolds number. *Mechanics Research Communications*, v. 18, n. 2, p. 145–150, 1991. doi:10.1016/0093-6413(91)90043-V. Cited on page 59.

O'ROURKE, P. J.; SNIDER, D. M. Inclusion of collisional return-to-isotropy in the MP-PIC method. *Chemical Engineering Science*, v. 80, p. 39–54, 2012. doi:10.1016/j.ces.2012.05.047. Cited on page 46.

PATANKAR, N. A.; JOSEPH, D. D. Modeling and numerical simulation of particulate flows by the Eulerian-Lagrangian approach. *International Journal of Multiphase Flow*, v. 27, n. 10, p. 1659–1684, 2001. doi:10.1016/S0301-9322(01)00021-0. Cited on page 42.

PATANKAR, S. *Numerical Heat Transfer and Fluid Flow.* Boca Raton: CRC Press, 1980. doi:10.1201/9781482234213. Cited 2 times on pages 80 and 83.

PENG, Z.; DOROODCHI, E.; ALGHAMDI, Y. A.; SHAH, K.; LUO, C.; MOGHTADERI, B. CFD-DEM simulation of solid circulation rate in the cold flow model of chemical looping systems. *Chemical Engineering Research and Design*, v. 95, p. 262–280, 2015. doi:10.1016/j.cherd.2014.11.005. Cited on page 42.

PENG, Z.; DOROODCHI, E.; LUO, C.; MOGHTADERI, B. Influence of void fraction calculation on fidelity of CFD-DEM simulation of gas-solid bubbling fluidized beds. *AIChE Journal*, v. 60, n. 6, p. 2000–2018, 2014. doi:10.1002/aic.14421. Cited 2 times on pages 47 and 86.

PEPIOT, P.; DESJARDINS, O. Numerical analysis of the dynamics of two- and three-dimensional fluidized bed reactors using an Euler-Lagrange approach. *Powder Technology*, v. 220, p. 104–121, 2012. doi:10.1016/j.powtec.2011.09.021. Cited on page 44.

PEREIRA, G. C.; SOUZA, F. J. de; MARTINS, D. A. de M. Numerical prediction of the erosion due to particles in elbows. *Powder Technology*, v. 261, p. 105–117, 2014. doi:10.1016/j.powtec.2014.04.033. Cited on page 35.

POPE, S. B. *Turbulent Flows*. Cambridge: Cambridge University Press, 2000. Cited on page 51.

POPOFF, B.; BRAUN, M. A Lagrangian approach to dense particulate flows. In: *International Conference on Multiphase Flow*. Leipzig: [s.n.], 2007. Cited on page 44.

RENZO, A. di; MAIO, F. P. di. Homogeneous and bubbling fluidization regimes in DEM-CFD simulations: hydrodynamic stability of gas and liquid fluidized beds. *Chemical Engineering Science*, v. 62, n. 1, p. 116–130, 2007. doi:10.1016/j.ces.2006.08.009. Cited on page 44.

RHIE, C. M.; CHOW, W. L. Numerical study of the turbulent flow past an airfoil with trailing edge separation. *AIAA Journal*, v. 21, n. 11, p. 1525–1532, 1983. doi:10.2514/3.8284. Cited on page 82.

ROSSBACH, V.; UTZIG, J.; DECKER, R. K.; NORILER, D.; SOARES, C.; MARTIGNONI, W. P.; MEIER, H. F. Gas-solid flow in a ring-baffled CFB riser: numerical and experimental analysis. *Powder Technology*, v. 345, p. 521–531, 2019. doi:10.1016/j.powtec.2018.12.096. Cited on page 37.

RUBINOW, S. I.; KELLER, J. B. The transverse force on a spinning sphere moving in a viscous fluid. *Journal of Fluid Mechanics*, v. 11, n. 03, p. 447, 1961. doi:10.1017/S0022112061000640. Cited 2 times on pages 59 and 60.

SAFFMAN, P. G. The lift on a small sphere in a slow shear flow. *Journal of Fluid Mechanics*, v. 22, n. 2, p. 385–400, 1965. doi:10.1017/S0022112065000824. Cited 2 times on pages 57 and 58.

SAFFMAN, P. G. The lift on a small sphere in a slow shear flow - Corrigendum. *Journal of Fluid Mechanics*, v. 31, n. 3, p. 624–624, 1968. doi:10.1017/S0022112068999990. Cited on page 57.

SAKAI, M.; YAMADA, Y.; SHIGETO, Y.; SHIBATA, K.; KAWASAKI, V. M.; KOSHIZUKA, S. Large-scale discrete element modeling in a fluidized bed. *International Journal for Numerical Methods in Fluids*, v. 64, n. 10-12, p. 1319–1335, 2010. doi:10.1002/fld.2364. Cited on page 42.

SALVO, R. de V. *Aplicação da metodologia euleriana-lagrangiana à análise do processo de separação em ciclones*. Thesis (PhD) — Federal University of Uberlândia, Uberlândia, 2013. Available at: <https://repositorio.ufu.br/handle/123456789/14717>. Cited on page 80.

SANTOS, V. F. dos; SOUZA, F. J. de; DUARTE, C. A. R. Reducing bend erosion with a twisted tape insert. *Powder Technology*, v. 301, p. 889–910, 2016. doi:10.1016/j.powtec.2016.07.020. Cited on page 35.

SCHILLER, L.; NAUMANN, A. A drag coefficient correlation. *Zeitschrift des Vereins Deutscher Ingenieure*, v. 77, p. 318–320, 1935. Cited 3 times on pages 57, 69, and 132.

SHEPARD, D. A two-dimensional interpolation function for irregularly-spaced data. In: *Proceedings of the 1968 23rd ACM National Conference*. New York, NY, USA: Association for Computing Machinery, 1968. (ACM '68), p. 517–524. doi:10.1145/800186.810616. Cited on page 86.

SHI, X.; SUN, R.; LAN, X.; LIU, F.; ZHANG, Y.; GAO, J. CPFD simulation of solids residence time and back-mixing in CFB risers. *Powder Technology*, v. 271, p. 16–25, 2015. doi:10.1016/j.powtec.2014.11.011. Cited on page 46.

SHI, X.; WU, Y.; LAN, X.; LIU, F.; GAO, J. Effects of the riser exit geometries on the hydrodynamics and solids back-mixing in CFB risers: 3D simulation using CPFD approach. *Powder Technology*, v. 284, p. 130–142, 2015. doi:10.1016/j.powtec.2015.06.049. Cited on page 46.

SLATTERY, C. *Momentum, Energy, and Mass Transfer in Continua*. New York: McGraw-Hill, 1972. Cited on page 62.

SNIDER, D. M. An incompressible three-dimensional multiphase particle-in-cell model for dense particle flows. *Journal of Computational Physics*, v. 170, n. 2, p. 523–549, 2001. doi:10.1006/jcph.2001.6747. Cited 2 times on pages 45 and 46.

SOLNORDAL, C. B.; KENCHE, V.; HADLEY, T. D.; FENG, Y.; WITT, P. J.; LIM, K.-S. Simulation of an internally circulating fluidized bed using a multiphase particle-in-cell method. *Powder Technology*, v. 274, p. 123–134, 2015. doi:10.1016/j.powtec.2014.12.045. Cited on page 46.

SOLNORDAL, C. B.; WONG, C. Y.; BOULANGER, J. An experimental and numerical analysis of erosion caused by sand pneumatically conveyed through a standard pipe elbow. *Wear*, v. 336-337, p. 43–57, 2015. doi:10.1016/j.wear.2015.04.017. Cited on page 77.

SOMMERFELD, M. Overview and fundamentals. In: BUCHLIN, J.-M. (Ed.). *Theoretical and Experimental Modelling of Particulate Flows*. Rhode Saint Genèse, Belgium: von Karman Institute for Fluid Dynamics, 2000, (Lecture Series 2000-06, 35). Cited on page 56.

SOMMERFELD, M. Validation of a stochastic Lagrangian modelling approach for inter-particle collisions in homogeneous isotropic turbulence. *International Journal of Multiphase Flow*, v. 27, n. 10, p. 1829–1858, 2001. doi:10.1016/S0301-9322(01)00035-0. Cited 10 times on pages 15, 32, 40, 42, 46, 71, 74, 76, 140, and 142.

SOMMERFELD, M.; HUBER, N. Experimental analysis and modelling of particle-wall collisions. *International Journal of Multiphase Flow*, v. 25, n. 6-7, p. 1457–1489, 1999. doi:10.1016/S0301-9322(99)00047-6. Cited on page 77.

SOMMERFELD, M.; KOHNEN, G.; RÜGER, M. Some open questions and inconsistencies of Lagrangian particle dispersion models. In: *Proceedings of the Ninth Symposium on Turbulent Shear Flows*. Kyoto: [s.n.], 1993. Cited on page 71.

SOMMERFELD, M.; KUSSIN, J. Wall roughness effects on pneumatic conveying of spherical particles in a narrow horizontal channel. *Powder Technology*, v. 142, n. 2, p. 180–192, 2004. doi:10.1016/j.powtec.2004.05.002. Cited on page 77.

SOMMERFELD, M.; LAÍN, S. Euler-Lagrange methods. In: MICHAELIDES, E. E.; CROWE, C. T.; SCHWARZKOPF, J. D. (Ed.). *Multiphase Flow Handbook*. 2. ed. Boca Raton: CRC Press, 2016. Cited on page 56.

SONG, F.; LI, F.; WANG, W.; LI, J. A sub-grid EMMS drag for multiphase particle-in-cell simulation of fluidization. *Powder Technology*, v. 327, p. 420–429, 2018. doi:10.1016/j.powtec.2017.12.079. Cited on page 46.

SOUZA, F. J. de; SALVO, R. de V.; MARTINS, D. A. de M. Large Eddy Simulation of the gas-particle flow in cyclone separators. *Separation and Purification Technology*, v. 94, p. 61–70, 2012. doi:10.1016/j.seppur.2012.04.006. Cited on page 35.

SOUZA, F. J. de; SALVO, R. de V.; MARTINS, D. A. de M. Simulation of the performance of small cyclone separators through the use of Post Cyclones (PoC) and annular overflow ducts. *Separation and Purification Technology*, v. 142, p. 71–82, 2015. doi:10.1016/j.seppur.2014.12.032. Cited on page 35.

SOUZA, F. J. de; SILVA, A. L.; UTZIG, J. Four-way coupled simulations of the gas-particle flow in a diffuser. *Powder Technology*, v. 253, p. 496–508, 2014. doi:10.1016/j.powtec.2013.12.021. Cited 3 times on pages 35, 77, and 80.

SPEIGHT, J. G. *The Chemistry and Technology of Petroleum*. 4. ed. [S.l.]: CRC Press, 2006. Cited on page 36.

SUN, R.; XIAO, H. Diffusion-based coarse graining in hybrid continuum-discrete solvers: applications in CFD-DEM. *International Journal of Multiphase Flow*, v. 72, p. 233–247, 2015. doi:10.1016/j.ijmultiphaseflow.2015.02.014. Cited on page 47.

SUN, R.; XIAO, H. Diffusion-based coarse graining in hybrid continuum-discrete solvers: theoretical formulation and a priori tests. *International Journal of Multiphase Flow*, v. 77, p. 142–157, 2015. doi:10.1016/j.ijmultiphaseflow.2015.08.014. Cited 3 times on pages 48, 86, and 87.

TENNETI, S.; GARG, R.; SUBRAMANIAM, S. Drag law for monodisperse gas-solid systems using particle-resolved direct numerical simulation of flow past fixed assemblies of spheres. *International Journal of Multiphase Flow*, v. 37, n. 9, p. 1072–1092, 2011. doi:10.1016/j.ijmultiphaseflow.2011.05.010. Cited 7 times on pages 17, 68, 69, 132, 134, 135, and 137.

TIAN, L.; AHMADI, G. Particle deposition in turbulent duct flows-comparisons of different model predictions. *Journal of Aerosol Science*, v. 38, n. 4, p. 377–397, 2007. doi:10.1016/j.jaerosci.2006.12.003. Cited on page 54.

TSUJI, Y.; KAWAGUCHI, T.; TANAKA, T. Discrete particle simulation of two-dimensional fluidized bed. *Powder Technology*, v. 77, n. 1, p. 79–87, 1993. doi:10.1016/0032-5910(93)85010-7. Cited on page 43.

TSUJI, Y.; MORIKAWA, Y. LDV measurements of an air-solid two-phase flow in a horizontal pipe. *Journal of Fluid Mechanics*, v. 120, p. 385–409, 1982. doi:10.1017/S002211208200281X. Cited 10 times on pages 15, 16, 99, 100, 101, 102, 103, 104, 115, and 140.

TSUJI, Y.; MORIKAWA, Y.; MIZUNO, O. Experimental measurement of the Magnus force on a rotating sphere at low Reynolds numbers. *Journal of Fluids Engineering*, v. 107, n. 4, p. 484–488, 1985. doi:10.1115/1.3242517. Cited on page 59.

TSUJI, Y.; MORIKAWA, Y.; SHIOMI, H. LDV measurements of an air-solid two-phase flow in a vertical pipe. *Journal of Fluid Mechanics*, v. 139, p. 417–434, 1984. doi:10.1017/S0022112084000422. Cited 10 times on pages 16, 102, 103, 104, 105, 106, 108, 111, 115, and 140.

TUKOVIĆ, Ž.; PERIĆ, M.; JASAK, H. Consistent second-order time-accurate non-iterative PISO-algorithm. *Computers & Fluids*, v. 166, p. 78–85, 2018. doi:10.1016/j.compfluid.2018.01.041. Cited on page 82.

U.S. Department of Energy. Energy Information Administration. Independent Statistics & Analysis. *U.S. Monthly Crude Oil Production Exceeds 10 Million Barrels per Day, Highest since 1970.* 2018. <https://www.eia.gov/todayinenergy/detail.php?id=34772>. Cited on page 36.

U.S. Department of Energy. Energy Information Administration. Independent Statistics & Analysis. *EIA Increases U.S. Crude Oil Production Forecast for 2019 and 2020.* 2019. <https://www.eia.gov/todayinenergy/detail.php?id=42055>. Cited on page 36.

U.S. Department of Energy. Energy Information Administration. Independent Statistics & Analysis. *Price Summary (Historical and Forecast).* 2019. <https://www.eia.gov/analysis/>. Cited on page 37.

UTZIG, J. *Dinâmica das partículas em leito fluidizado circulante.* Thesis (PhD) — Federal University of Uberlândia, Uberlândia, 2016. Available at: <https://repositorio.ufu.br/handle/123456789/18235>. Cited 7 times on pages 15, 35, 37, 98, 120, 121, and 142.

VREMAN, A. W. Turbulence attenuation in particle-laden flow in smooth and rough channels. *Journal of Fluid Mechanics*, v. 773, p. 103–136, 2015. doi:10.1017/jfm.2015.208. Cited on page 77.

VREMAN, A. W. Particle-resolved direct numerical simulation of homogeneous isotropic turbulence modified by small fixed spheres. *Journal of Fluid Mechanics*, v. 796, p. 40–85, 2016. doi:10.1017/jfm.2016.228. Cited on page 49.

VREMAN, A. W.; GEURTS, B. J.; DEEN, N. G.; KUIPERS, J. A. M. Large-Eddy Simulation of a particle-laden turbulent channel flow. In: FRIEDRICH, R.; GEURTS, B. J.; MÉTAIS, O. (Ed.). *Direct and Large-Eddy Simulation V.* Dordrecht: Springer, 2004, (ERCOFTAC Series, v. 9). p. 271–278. Cited on page 49.

WANG, Q.; NIEMI, T.; PELTOLA, J.; KALLIO, S.; YANG, H.; LU, J.; WEI, L. Particle size distribution in CPFD modeling of gas-solid flows in a CFB riser. *Particuology*, v. 21, p. 107–117, 2015. doi:10.1016/j.partic.2014.06.009. Cited on page 46.

WANG, Q.; YANG, H.; WANG, P.; LU, J.; LIU, Q.; ZHANG, H.; WEI, L.; ZHANG, M. Application of CPFD method in the simulation of a circulating fluidized bed with a loop seal Part II—Investigation of solids circulation. *Powder Technology*, v. 253, p. 822–828, 2014. doi:10.1016/j.powtec.2013.11.040. Cited on page 46.

WANG, Q.; YANG, H.; WANG, P.; LU, J.; LIU, Q.; ZHANG, H.; WEI, L.; ZHANG, M. Application of CPFD method in the simulation of a circulating fluidized bed with a loop seal, Part I—Determination of modeling parameters. *Powder Technology*, v. 253, p. 814–821, 2014. doi:10.1016/j.powtec.2013.11.041. Cited on page 46.

WEBER, J. M.; LAYFIELD, K. J.; ESSENDELFT, D. T. V.; MEI, J. S. Fluid bed characterization using Electrical Capacitance Volume Tomography (ECVT), compared to CPFD software's Barracuda. *Powder Technology*, v. 250, p. 138–146, 2013. doi:10.1016/j.powtec.2013.10.005. Cited on page 46.

WHITE, F. M. *Viscous Fluid Flow*. 3. ed. Boston: McGraw-Hill, 2006. Cited on page 50.

WIKIPEDIA. *Fluid Catalytic Cracking – Wikipedia, the Free Encyclopedia*. 2019. <https://en.wikipedia.org/wiki/Fluid_catalytic_cracking>. Cited on page 36.

WILCOX, D. C. *Turbulence Modeling for CFD*. La Cañada: DCW Industries, 1993. Cited 2 times on pages 51 and 96.

WU, C. L.; ZHAN, J. M.; LI, Y. S.; LAM, K. S.; BERROUK, A. S. Accurate void fraction calculation for three-dimensional discrete particle model on unstructured mesh. *Chemical Engineering Science*, v. 64, n. 6, p. 1260–1266, 2009. doi:10.1016/j.ces.2008.11.014. Cited on page 48.

XIAO, H.; SUN, J. Algorithms in a robust hybrid CFD-DEM solver for particle-laden flows. *Communications in Computational Physics*, v. 9, n. 02, p. 297–323, 2011. doi:10.4208/cicp.260509.230210a. Cited on page 48.

XIE, J.; ZHONG, W.; YU, A. MP-PIC modeling of CFB risers with homogeneous and heterogeneous drag models. *Advanced Powder Technology*, v. 29, n. 11, p. 2859–2871, 2018. doi:10.1016/j.apt.2018.08.007. Cited on page 46.

YEO, K.; MAXEY, M. R. Simulation of concentrated suspensions using the force-coupling method. *Journal of Computational Physics*, v. 229, n. 6, p. 2401–2421, 2010. doi:10.1016/j.jcp.2009.11.041. Cited on page 49.

ZHANG, S.; ZHAO, X.; BAYYUK, S. Generalized formulations for the Rhie-Chow interpolation. *Journal of Computational Physics*, v. 258, p. 880–914, 2014. doi:10.1016/j.jcp.2013.11.006. Cited on page 82.

ZHANG, W.; YOU, C. Numerical simulation of particulate flows in CFB riser with drag corrections based on particle distribution characterization. *Chemical Engineering Journal*, v. 303, p. 145–155, 2016. doi:10.1016/j.cej.2016.05.139. Cited on page 46.

ZHAO, Y.; CHENG, Y.; WU, C.; DING, Y.; JIN, Y. Eulerian-Lagrangian simulation of distinct clustering phenomena and RTDs in riser and downer. *Particuology*, v. 8, n. 1, p. 44–50, 2010. doi:10.1016/j.partic.2009.11.002. Cited on page 44.

ZHOU, Z. Y.; KUANG, S. B.; CHU, K. W.; YU, A. B. Discrete particle simulation of particle-fluid flow: Model formulations and their applicability. *Journal of Fluid Mechanics*, v. 661, p. 482–510, 2010. doi:10.1017/S002211201000306X. Cited on page 41.